

AD-A194 677

AN INVESTIGATION INTO THE METALLURGICAL ASPECTS OF
JOINING RAPIDLY-SOLIDIFIED (U) OHIO STATE UNIV RESEARCH
FOUNDATION COLUMBUS W A BAESLACK 01 APR 88

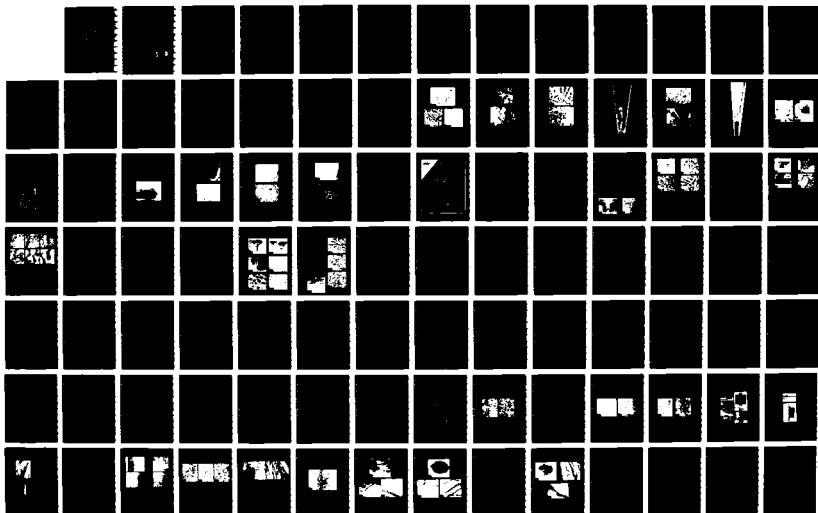
1/2

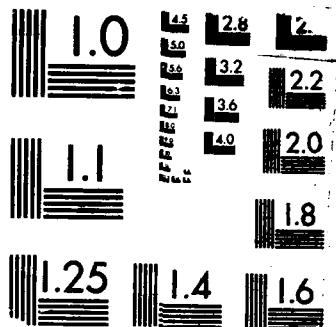
UNCLASSIFIED

ARO-20987. 4-MS DARG29-04-K-0176

F/O 11/6.2

NL





DTIC FILE COPY

ARO 20987.4-MS

(2)

AD-A194 677

RF Project 764348/716625
Final Report

AN INVESTIGATION INTO THE METALLURGICAL ASPECTS
OF JOINING RAPIDLY-SOLIDIFIED ALUMINUM ALLOYS

William A. Baeslack III
Department of Metallurgical Engineering

For the Period
September 1, 1984 - December 31, 1987

DEPARTMENT OF THE ARMY
U.S. Army Research Office
Research Triangle Park, North Carolina 27709

Contract No. DAAG29-84-K-0176

April 1988

DTIC
ELECTE
MAY 11 1988
S D
CAH

OSU

The Ohio State University
Research Foundation

1314 Kinnear Road
Columbus, Ohio 43212

DISTRIBUTION STATEMENT A

Approved for public release;
Distribution Unlimited

88 5 10 047

ADA194677

UNCLASSIFIED
SECURITY CLASSIFICATION OF THIS PAGE

MASTER COPY

FOR REPRODUCTION PURPOSES

REPORT DOCUMENTATION PAGE

1a. REPORT SECURITY CLASSIFICATION Unclassified		1b. RESTRICTIVE MARKINGS	
2a. SECURITY CLASSIFICATION AUTHORITY		3. DISTRIBUTION/AVAILABILITY OF REPORT Approved for public release; distribution unlimited.	
2b. DECLASSIFICATION/DOWNGRADING SCHEDULE		4. PERFORMING ORGANIZATION REPORT NUMBER(S) RF Project 764348/716625	
5. MONITORING ORGANIZATION REPORT NUMBER(S) ARO 20987.4-M5		6a. NAME OF PERFORMING ORGANIZATION The Ohio State University Research Foundation	
6b. OFFICE SYMBOL (If applicable) OSURF		7a. NAME OF MONITORING ORGANIZATION U. S. Army Research Office	
6c. ADDRESS (City, State, and ZIP Code) 1314 Kinnear Road Columbus, Ohio 43212		7b. ADDRESS (City, State, and ZIP Code) P. O. Box 12211 Research Triangle Park, NC 27709-2211	
8a. NAME OF FUNDING/SPONSORING ORGANIZATION U. S. Army Research Office		8b. OFFICE SYMBOL (If applicable)	
8c. ADDRESS (City, State, and ZIP Code) P. O. Box 12211 Research Triangle Park, NC 27709-2211		9. PROCUREMENT INSTRUMENT IDENTIFICATION NUMBER DAA629-84-K-0176	
10. SOURCE OF FUNDING NUMBERS		11. TITLE (Include Security Classification)	
PROGRAM ELEMENT NO.	PROJECT NO.	TASK NO.	WORK UNIT ACCESSION NO.
12. PERSONAL AUTHOR(S) William A. Baeslack III		13a. TYPE OF REPORT FINAL	
13b. TIME COVERED FROM 9/84 TO 12/87		14. DATE OF REPORT (Year, Month, Day) 1988 April 1	
15. PAGE COUNT 109		16. SUPPLEMENTARY NOTATION The view, opinions and/or findings contained in this report are those of the author(s) and should not be construed as an official Department of the Army position, policy, or decision, unless so designated by other documentation.	
17. COSATI CODES		18. SUBJECT TERMS (Continue on reverse if necessary and identify by block number)	
FIELD	GROUP	SUB-GROUP	
		aluminum, welding, rapid-solidification, powder metallurgy, joining, weldability, electron beam welding, inertia-friction welding, diffusion welding, capacitor-discharge welding	
19. ABSTRACT (Continue on reverse if necessary and identify by block number) Research performed during this program demonstrated that the metastable microstructures upon which rapidly-solidified, powder metallurgy (RS/PM) aluminum alloys depend for their unique mechanical properties can be both recreated using rapid solidification fusion welding processes and/or retained using solid-state welding processes. Alloys investigated included Al-Fe-X dispersoid-type compositions developed for superior elevated-temperature properties and Al-Li-X alloys developed for high strength and modulus and low density. Processes found to be most effective for the joining of these alloys included rapid-solidification electron beam and capacitor-discharge welding and solid-state inertia-friction and diffusion welding. Metallurgical phenomena investigated included solidification, solid-state phase transformations, defect formation and structure-property-fracture relationships. RS/PM aluminum alloys which contain low hydrogen levels, such as the inertly produced Al-8Fe-2Mo alloy, were effectively joined using the high-energy density electron-beam welding. Keywords: Iron, Lithium, Molybdenum, Cerium			
20. DISTRIBUTION/AVAILABILITY OF ABSTRACT <input type="checkbox"/> UNCLASSIFIED/UNLIMITED <input checked="" type="checkbox"/> SAME AS RPT. <input type="checkbox"/> OTIC USERS		21. ABSTRACT SECURITY CLASSIFICATION Unclassified	
22a. NAME OF RESPONSIBLE INDIVIDUAL Dr. Andrew Crowson - Materials Science Div.		22b. TELEPHONE (Include Area Code) (919) 549-0641	
		22c. OFFICE SYMBOL ARO	

DD FORM 1473, 84 MAR

83 APR edition may be used until exhausted.
All other editions are obsolete.SECURITY CLASSIFICATION OF THIS PAGE
UNCLASSIFIED

FINAL REPORT

on

AN INVESTIGATION INTO THE METALLURGICAL ASPECTS OF JOINING
RAPIDLY-SOLIDIFIED ALUMINUM ALLOYS

Contract Number: DAAG29-84-K-0176

Contract Period: 1 September 1986 to 30 December 1987


Submitted to:

Army Research Office
Research Triangle Park, North Carolina 27709

Submitted by:

The Department of Welding Engineering
The Ohio State University
Columbus, OH 43210

1 April 1988


W. A. Baeslack III, Associate Professor
Principal Investigator

APPROVED FOR PUBLIC DISTRIBUTION
DISTRIBUTION UNLIMITED

TABLE OF CONTENTS

SUMMARY	ii
INTRODUCTION.	1
Electron Beam Weldability of Al-8Fe-2Mo.	2
Capacitor-Discharge Welding of Al-Fe-Ce.	4
Inertia-Friction Welding of Al-Fe-X Alloys	5
Diffusion Welding of Al-Fe-Ce.	6
Weldability of RS/PM Al-Li-X Alloys.	7
PROJECT PERSONNEL AND DEGREES GRANTED	9
TECHNICAL REPORTS AND PUBLICATIONS.	9
APPENDIX I.	24



Accession For	
NTIS GRA&I	<input checked="" type="checkbox"/>
DTIC TAB	<input type="checkbox"/>
Unannounced	<input type="checkbox"/>
Justification	
By _____	
Distribution/	
Availability Codes	
Dist	Avail and/or Special
A-1	

SUMMARY

Rapidly-solidified, powder metallurgy (RS/PM) aluminum alloys are experiencing continued development and increased utilization in DoD applications due to their superior room and elevated-temperature properties versus conventional ingot metallurgy (IM) aluminum alloys. The effective integration of these new materials in structural applications will require the use of efficient and economical joining methods. Unfortunately, the unique metallurgical characteristics exhibited by these RS/PM alloy systems generally preclude their joining using conventional techniques, and therefore require the development and application of advanced joining methodologies. In addition, the optimization of joint microstructures and mechanical properties requires an understanding of the welding or joining metallurgy of these alloys. The principal objective of this study was to address these important requirements by investigating the fundamental metallurgical aspects of joining advanced, rapidly-solidified, powder metallurgy aluminum alloys.

Research performed during this program demonstrated that the metastable RS/PM microstructures upon which these alloys depend for their unique mechanical properties can be both "recreated" using rapid-solidification fusion welding processes and/or "retained" using solid-state welding processes. Alloys investigated included both Al-Fe-X dispersoid-type alloys developed for high strength and superior elevated-temperature

properties and, to a lesser extent, highly-alloyed Al-Li-X alloys developed for low density, high modulus and high strength. Processes found most effective for the joining of these alloys included rapid-solidification electron-beam and capacitor-discharge welding and solid-state inertia-friction and diffusion welding. Metallurgical phenomena investigated included solidification phenomena, solid-state phase transformations, defect formation and structure-property-fracture relationships.

RS/PM aluminum alloys which contain low hydrogen levels, such as the inertly-produced Al-8Fe-2Mo alloy, were effectively joined using the high-energy density electron beam welding process. By minimizing the weld energy input and thereby maximizing weld fusion zone solidification and cooling rates, a microstructure comprised of extremely fine intermetallics in a matrix of alpha aluminum was generated which promoted high joint efficiencies (exceeding 75-80%). Relationships between weld fusion zone nucleation and growth phenomena, heat-affected zone coarsening, mechanical properties and weld fracture behavior were developed for a wide range of electron beam energy inputs.

Capacitor-discharge welding was alternatively demonstrated to be a rapid-solidification, fusion welding process capable of effectively joining Al-Fe-Ce alloys which exhibit high hydrogen levels. The extremely rapid-solidification provided by this process (comparable to splat cooling) and high pressures experienced during weld solidification produced high integrity weld structures and joint efficiencies of 100%. The effect of

process parameters on weld cooling rate and solidification phenomena (ie., the formation of a Zone A versus Zone B fusion zone microstructure), joint properties and fracture behavior were determined. The generation of high-strength, defect-free joints in Al-Fe-X RS/PM alloys which contained high hydrogen contents (thereby precluding the application of electron beam welding due to porosity formation) was also achieved using the solid-state inertia-friction welding process. The in-depth metallurgical evaluation of inertia-friction welds produced in Al-Fe-Ce and Al-Fe-Mo-V alloys showed that through the optimization of weld axial force, the fine, metastable base metal microstructure could be retained across the weld interface and that outer-periphery defects could be eliminated. Solid-state phase coarsening in the inertia-friction weld heat-and deformation zone and the effects of this phenomenon on weld strength and fractographic characteristics were determined.

The diffusion welding of high hydrogen level Al-Fe-Ce alloys was investigated using a silver interlayer. Using the Gleeble 1500 System, bonding temperature/pressure/time parameter combinations were developed to produce diffusion welds without excessive microstructural coarsening and associated property degradation in the base metal. Metallurgical analysis of bonds produced over this range of bonding parameters determined that the welds produced at low pressure (ie., negligible macroscopic deformation) exhibited low strength due to the formation of Kirkendall porosity at the interface between the original silver

interlayer and the Al-Fe-Ce base alloy. The application of higher pressures promoted macroscopic deformation which resulted in higher weld integrity and increased weld strengths.

The effective fusion welding of highly-alloyed RS/PM Al-Li-X alloys was prevented due to excessive porosity formation. High-temperature degassing studies on the consolidated product were ineffective in reducing hydrogen levels to levels required to completely eliminate porosity without the excessive coarsening of intermetallics in the base material.

INTRODUCTION

In recent years, the development of RS/PM aluminum alloys has continued at a significant pace, with a wide variety of alloy compositions currently available which offer property combinations superior to those of conventional aluminum alloys. Alloy chemistries range from those of near-conventional IM alloys, which utilize RS/PM primarily for purposes of improved compositional homogeneity and grain and dispersoid refinement, to highly unconventional chemistries which take full advantage of the rapid solidification process to develop unique microstructures and properties not obtainable via conventional ingot metallurgy. The Al-Fe-X dispersoid-type alloys represent perhaps the most significant example of this latter RS/PM aluminum alloy category.

Commensurate with the increased development and application of these advanced materials has been the increased consideration of their joinability. Research on the joining of RS/PM aluminum alloys at OSU under ARO support has been fundamental in nature, directed primarily at developing an improved understanding of the basic metallurgical phenomena associated with the joining of RS/PM alloys whose chemistries are highly unconventional and which differ appreciably from IM alloy compositions. In addition to metallurgical aspects, an important consideration of this work was the iterative process of identifying and evaluating joining processes which were most amenable to producing high quality

joints. Based on preliminary work, both fusion and solid-state welding processes were investigated.

The following sections provide a summary of important results determined in this three-year investigation. During the past two years, much of this research has been presented at national and international forums and published in the open literature. (Selected publications are provided in Appendix I.) Consequently, the following sections will concentrate on the most recent experimental results which are currently under preparation for presentation and publication.

Electron Beam Weldability of Al-8Fe-2Mo

Al-8Fe-2Mo is a semi-commercial dispersoid-type RS/PM alloy produced using completely inert atomization and consolidation. The correspondingly low hydrogen level exhibited by this alloy (typically below 0.5 ml/100 gm) allows fusion welding without the formation of hydrogen-induced porosity. Through variations in sheet thickness and electron beam welding parameters, full-penetration, autogenous welds were produced which exhibited a range of cooling rates between about 10^3 and 10^4 C/s through the solidification range (Appendix IA). Subsequent to weld generation, the weld macro and microstructures, room-temperature mechanical properties and fracture behavior were characterized. Light and scanning-electron and transmission-electron microscopy analysis showed a significant influence of cooling rate in promoting the formation of an increasingly finer Zone B fusion zone microstructure comprised of extremely fine intermetallics in

a matrix of dendritic alpha aluminum (Figures 1 and 2). At the highest cooling rates, Zone A microeutectic regions were observed.

An important aspect of fusion zone microstructure evolution involved the effects of incomplete base metal dispersoid dissolution during welding in providing heterogeneous nucleation sites during solidification. Extensive experimental and analytical analysis using appropriate kinetic equations for particle dissolution suggested that this effect is significant primarily in the vicinity of the weld fusion boundary, where temperatures are relatively low and fluid flow sluggish. This nucleation phenomenon may partially account for a coarsened intermetallic structure exhibited by the partially-melted and/or partially mixed zone adjacent to the fusion line (Figures 1 and 3). Achieving increased depth/width ratios and the associated higher fusion boundary temperature gradients were successful in minimizing and eliminating these regions (Appendix IB).

Microhardness traverses across the EB weld zones showed fusion zone hardnesses of the most rapidly-solidified weld zones to equal or exceed that of the base metal. As shown in Appendix IA/Figure 3 and Appendix IB/Figure 4, however, hardness decreases in the dispersoid-coarsened partially-melted region of the higher energy input welds, or in the HAZ of the low-energy input welds, limited overall weld efficiencies as determined by hardness and transverse tensile testing to 75 to 80%.

Fractographic analysis more clearly demonstrated the degrading influence of the coarsened partially-melted region

dispersoid structure in promoting localized failure. As shown in Appendix IA/Figure 6 for a weld produced at a high energy input, transverse-weld oriented tensile fracture in this region at low strength and low ductility resulted from delamination of the intermetallics and the alpha aluminum matrix.

Extensive work was completed on evaluating new dispersoid-type Al-Fe-X type alloys for potential weldability using RS fusion welding processes. Chill castings which provided cooling rates ranging from 10 to 10^4 C/s were produced for Al-Fe, Al-Fe-Mo, Al-Fe-Ce, Al-Fe-Ni and Al-Fe-Co alloys of varying composition in order to examine compositional and cooling rate effects on the proportions of Zone A and Zone B in the microstructures. Results indicated that Al-3-6 wt%Fe-1-4wt%Ni alloys offer a strong potential for providing the desirable high proportion of Zone A microeutectic (Figures 4 and 5) at cooling rates associated with electron beam and laser welding, thereby promoting high weld strengths. As shown in Figure 6 and 7, Al-Fe-Ce and Al-Fe-Mo alloys were observed to exhibit greater proportions of the softer and lower strength Zone B microstructures at comparable alloying levels versus the Al-Fe-Ni alloys. A correlation of these microstructural results with actual welded structures was shown via the generation of laser welds on each of these chill castings vertically across the range of casting solidification structures. Detailed structure and property analysis of these laser welds will be continued in the follow-on program.

Capacitor-Discharge Welding of Al-Fe-Ce

In this study, the capacitor-discharge welding process was shown to be extremely successful in producing high-quality, rapidly-solidified welds in an Al-8Fe-4Ce alloy which exhibited a high hydrogen content. Structural analysis showed the weld solidification and cooling rate to be dependent on the welding process parameters. Welds produced at the maximum cooling rate exhibited a Zone A fusion zone microstructure appreciably harder and stronger than that of the unaffected base metal and negligible evidence of a heat-affected zone (Appendix IC/Figure 3). Fracture of these most rapidly solidified weldments occurred across the unaffected base metal. Slower cooling rates promoted a Zone B microstructure and the occasional presence of spherical defects at the weld centerline. These solidification defects were observed to serve as preferential fracture initiation sites during mechanical testing (Appendix IC/Figure 6). Minimal evidence of porosity in these weldments, despite the high base metal hydrogen content, was attributed to the high pressure during and immediately subsequent to weld solidification minimizing the growth of pores and possibly promoting pore closure via mechanical deformation.

Inertia-Friction Welding of Al-Fe-X Alloys

Many Al-Fe-X alloys, including Al-Fe-Ce and certain Al-Fe-Mo alloy compositions exhibit inherently high hydrogen contents (typically 1-10 ml/100gm) due to atomization in flue-gas and/or non-inert consolidation and processing. For such alloys, solid-

state welding provides an important alternative to fusion welding since melting and solidification are avoided. Inertia-friction welding is a solid-state process which combines frictional heating at faying surfaces with a high axial force to produce a metallurgical bond. The absence of melting at the interface during welding minimizes or eliminates the formation of hydrogen-induced porosity. In addition, the expulsion of surface contaminants (oxides) and severely heat-and-deformation affected metal at the faying interfaces promotes final bonding between fresh subsurface materials. These process advantages were demonstrated through the generation and metallurgical evaluation of inertia-friction welds between Al-9Fe-4Ce, Al-9Fe-4Ce and Al-8.7Fe-2.8Mo-1V dispersoid type alloys. In this work, the influence of axial force was found to be significant in controlling the weld macro and microstructures, the formation of weld defects and ultimately weld mechanical properties and fracture behavior. Appendix ID/Figure 10 illustrates the microstructure and hardness traverses across the weld interface for inertia-friction welds in Al-9Fe-4Ce produced at (A) low and (B) high axial force. At low axial force, SEM analysis revealed appreciable coarsening and softening of the metastable dispersoid and alpha grain structures at the weld interface, and to a lesser extent in the adjacent heat-and-deformation zone, resulting in preferential interface fracture at reduced strength. Increased axial force promoted shorter weld thermal cycles and the increased expulsion of the dispersoid-coarsened microstructure

out of the bond region as flash, thereby resulting in welds between nearly unaffected microstructures and higher strengths approaching that of the base metal. Increased axial force was also found to eliminate outer periphery defects which form at the interface due to plastic instabilities during interface deformation. Figure 8 illustrates an inertia-friction weld between 25 mm diameter Al-8.7Fe-2.8Mo-1V alloy produced using inert atomization. Despite significant local deformation at the weld interface, hardnesses across the bond line of a weld produced at high pressure were equivalent or greater than that of the base metal, and mechanical fracture of this weld occurred in the unaffected base metal. As in the Al-Fe-Ce alloys, the use of a low welding pressure, however, promoted appreciable microstructural coarsening and a softening at the weld interface.

Diffusion Welding of Al-Fe-Ce Alloys

Diffusion welding offers an alternative solid-state joining process which ideally involves little or no macroscopic deformation. This work initially determined welding temperature/time/pressure combinations which were suitable for diffusion welding of the Al-Fe-Ce alloy without promoting appreciable microstructural coarsening and corresponding softening. The result of a typical plot of welding temperature versus time for a 10 VPN maximum drop in hardness is shown in Figure 9. Subsequent to the identification of acceptable welding parameter ranges, silver interlayers were deposited electrolytically or by sputtering on the Al-Fe-Ce alloy specimen

surfaces and the specimens were welded in vacuum using a Gleeble 1500 system.

A systematic evaluation of bonding parameters on the weld structure, mechanical properties and fracture behavior showed the formation of Kirkendall porosity at the interface between the silver interlayer (which ultimately transformed to a complex Al and Ag-rich intermetallic) to reduce weld strength and ductility (Figures 10 and 11). Through the use of increased temperatures and pressures, which promoted macroscopic deformation at the weld interface, higher quality welds were produced exhibiting near base metal strength. These improved weld properties were attributed to the dissolution and dispersion of continuous intermetallics along the weld interface and effect of higher pressures on pore closure during the later stages of the welding process.

Weldability of RS/PM Al-Li-X Alloys

The addition of lithium to aluminum alloys offers significant property improvements, including reduced density, higher modulus and increased strength. Although conventional Al-Li alloys produced by ingot metallurgy are experiencing increased evaluation and utilization by industry (eg., 2090, 2091, 8090), rapid-solidification offers the possibility to produce more highly alloyed Al-Li alloys. In the present work, the weldability of selected highly-alloyed Al-Li-X alloys produced by Pratt and Whitney was evaluated. Alloy compositions included: Al-4.0Li-3.0Cu-1.5Mg-0.18Cr-0.2Zr and Al-3.0Li-5.5Mg-0.2Zr alloys. These

alloys were observed to contain appreciable second phases in the as-received base metal, as shown in Figure 12 for the Al-4.0Li-3.0Cu-1.5Mg-0.18Cr-0.2Zr alloy. In addition, initial gas tungsten-arc and electron beam fusion welding studies on these alloys showed appreciable porosity, despite their apparent inert processing. Since these alloys require solution heat treatment and aging to maximize strengthening (in contrast to the dispersoid-strengthened Al-Fe-X alloys), degassing trials were performed on the consolidated product over a range of temperatures up to approximately 550 C/48 hours. Results indicated that vacuum degassing even at these high temperatures was inadequate in reducing hydrogen to levels required to eliminate porosity. In addition, such degassing promoted appreciable surface depletion of alloying elements and the coarsening of second phase particles which degraded mechanical properties (Figure 12).

As shown in Figure 13, fusion weldments in these alloys exhibited dendritic alpha aluminum structures with appreciable eutectic constituent at interdendritic regions. Unfortunately, excessive porosity precluded effective mechanical property evaluation. The future study of such alloys will be restricted to solid-state joining techniques.

PROJECT PERSONNEL AND DEGREES GRANTED

- A. R. Gentry, MS in Welding Engineering, 1985
- B. K. Hagey, MS in Welding Engineering, 1986
- C. V. Ananthanarayanan, Ph.D. in Welding Engineering, (to be granted in June, 1988)
- D. S. Krishnaswamy, Ph.D. in Welding Engineering (to be granted in August, 1988)

TECHNICAL REPORTS AND PUBLICATIONS

Technical Reports

- a. R. Gentry, "A Study of the Effect of Vacuum Degassing and Fusion Welding on Experimental IM and PM Al-Li Alloys," MS Thesis, Department of Welding Engineering, The Ohio State University (1985).
- b. K. Hagey, "Inertia-Friction Welding of Rapidly-Solidified Aluminum Alloys," MS Thesis, Department of Welding Engineering, The Ohio State University (1986).
- c. V. Ananthanarayanan, "Diffusion Welding of a Rapidly-Solidified Al-Fe-Ce Alloy," Ph.D. Thesis (Pending Final Approval), Department of Welding Engineering, The Ohio State University (1988).

Publications (See Appendix I)

- a. W. A. Baeslack III and S. Krishnaswamy, "Electron Beam Weldability of a Rapidly-Solidified, Powder Metallurgy Aluminum Alloy," Trends in Welding Research, S. A. David, ed., ASM International (1986) 357-363.
- b. S. Krishnaswamy and W. A. Baeslack III, "Structure and Properties of Rapidly-Solidified Weldments in Al-8Fe-2Mo," Materials Science and Engineering, (in press).
- c. W. A. Baeslack III and K. Hagey, "Inertia Friction Welding of a Rapidly-Solidified Aluminum Alloy," Welding Journal/Research Supplement, (in press).
- d. W. A. Baeslack III, K. H. Hou and J. H. Devletian, "Rapid Solidification Joining of a Powder Metallurgy Al-Fe-Ce Alloy," Journal of Materials Science Letters, (in press).
- e. W. A. Baeslack III, "Metallurgy of Joining Rapidly-Solidified Aluminum Alloys," Proceedings of Second International SAMPE Metals and Metals Processing Conference, Dayton, OH, 1988 (in preparation).
- f. W. A. Baeslack III and K. H. Hou, "Electron Microscopy Study of Inertia-Friction Welded Al-8.7Fe-2.8Mo-1V," Journal of Materials Science Letters (in preparation).
- g. S. Krishnaswamy and W. A. Baeslack III, "A Study of Chill-Cast Microstructures in Al-Fe-X Alloys," Metallography (in press).

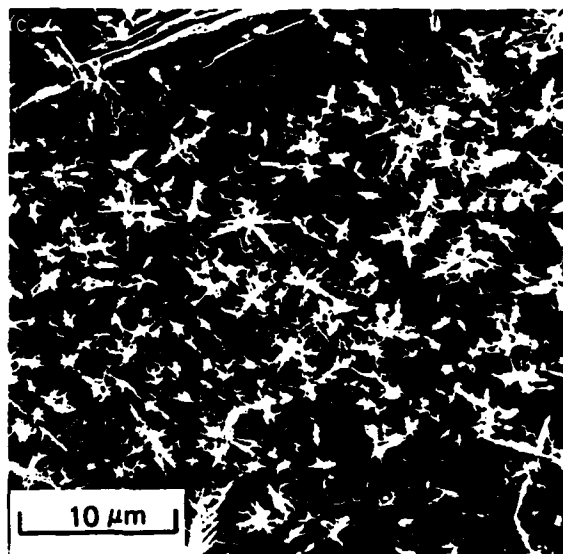
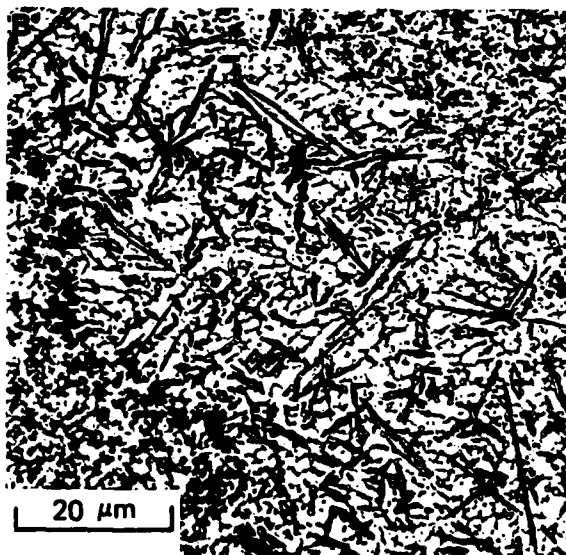
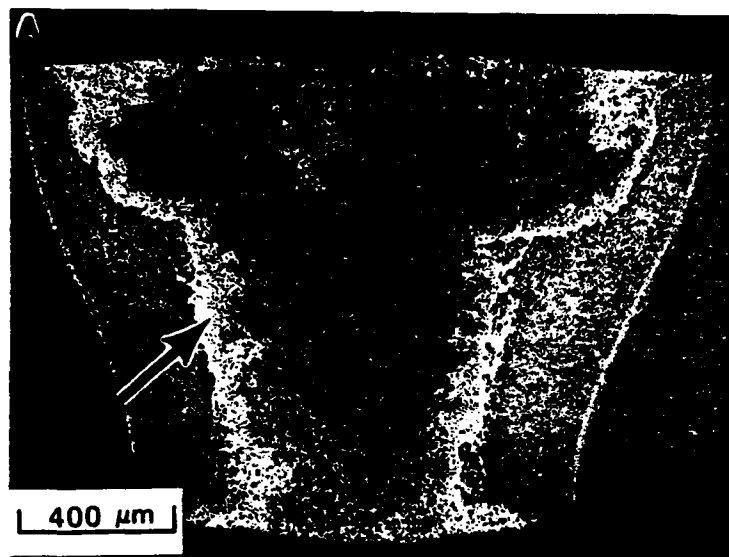


Figure 1. Electron beam weld in Al-8Fe-2Mo produced at medium energy input: A: light micrograph, arrow indicates light-appearing, dispersoid-coarsened partially-melted or partially-mixed region, (B) light and (C) SEM micrographs of dispersoid-coarsened region.

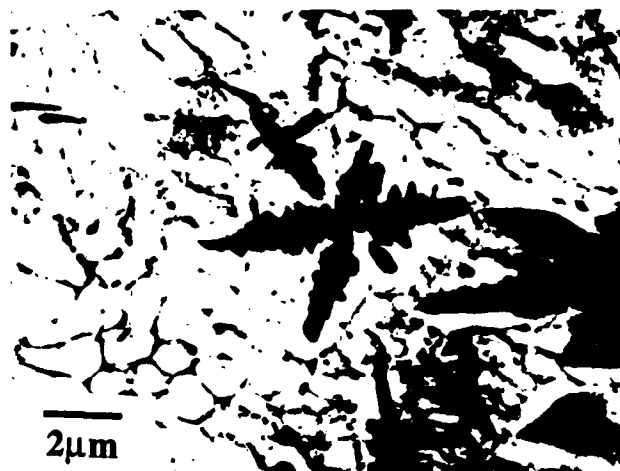


Figure 2. Transmission-electron micrographs showing Zone B microstructure at center of electron beam weld in Al-8Fe-2Mo produced at low energy input.

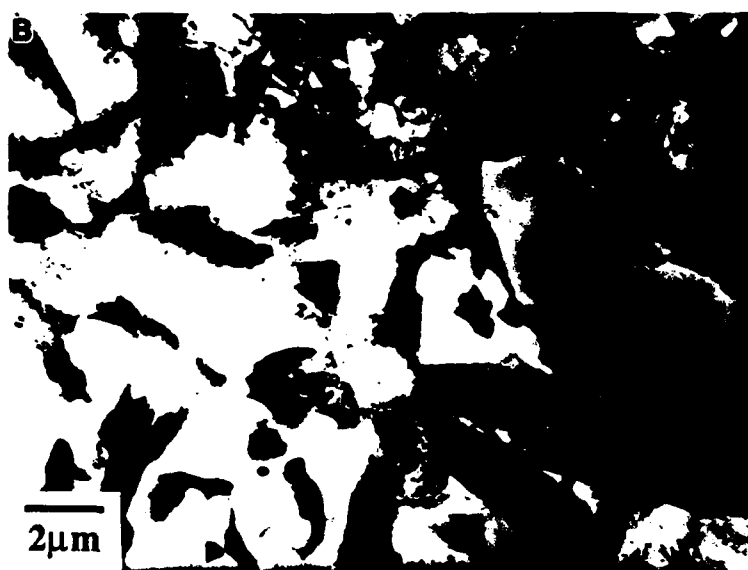
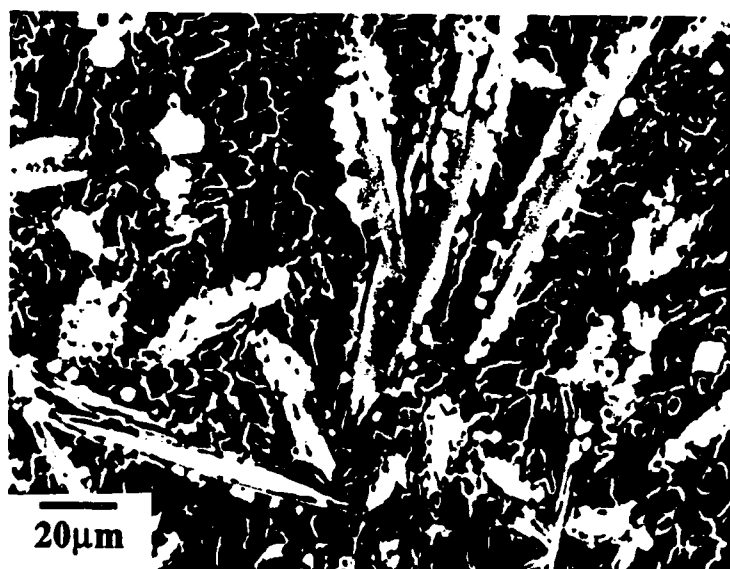


Figure 3. Scanning-electron (A) and transmission-electron (B) micrographs of partially-melted or partially-mixed region of electron beam weld in Al-8Fe-2Mo shown in Figure 1.



Figure 4. Light macrograph of Al-6Fe-4Ni chill casting cross section. Arrow indicates boundary between predominantly coupled-eutectic growth and Zone B solidification.



Figure 5. Light (A) and SEM (B) micrographs of coupled eutectic growth in Al-6Fe-4Ni chill casting.

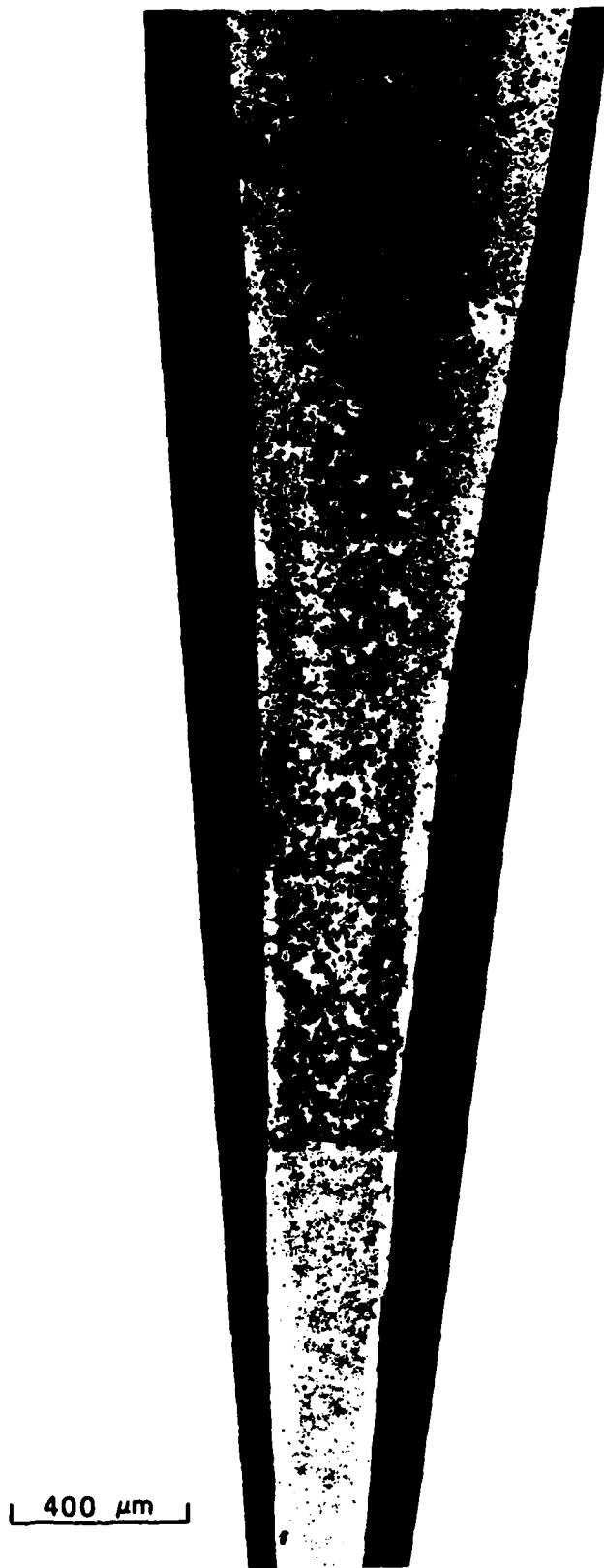


Figure 6. Light macrograph of Al-8Fe-2Mo chill casting cross section.



Figure 7. SEM micrographs of Al-8Fe-2Mo chill casting showing primary nucleation of alpha aluminum on intermetallic growth centers.

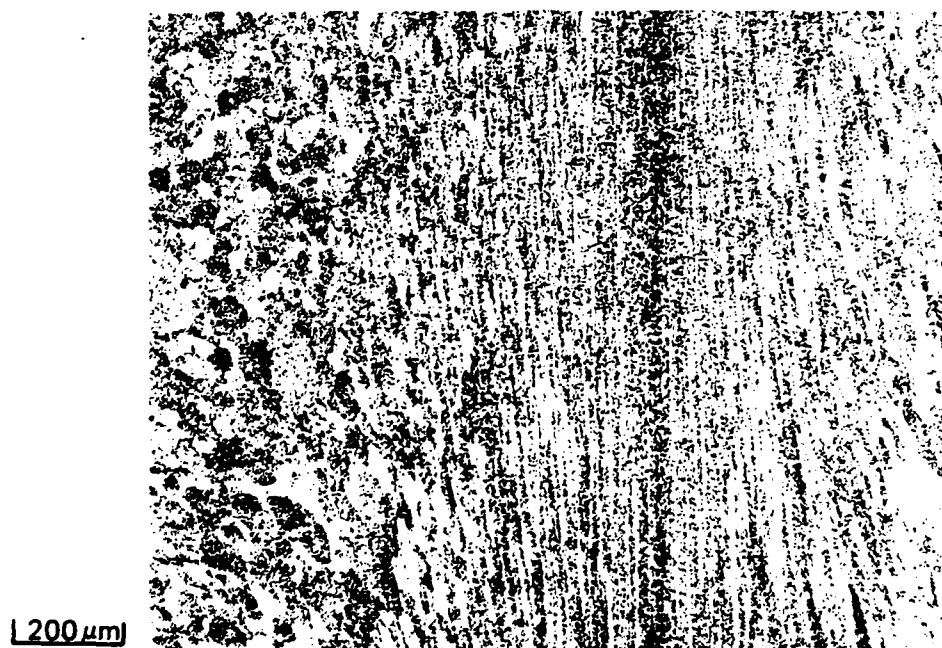
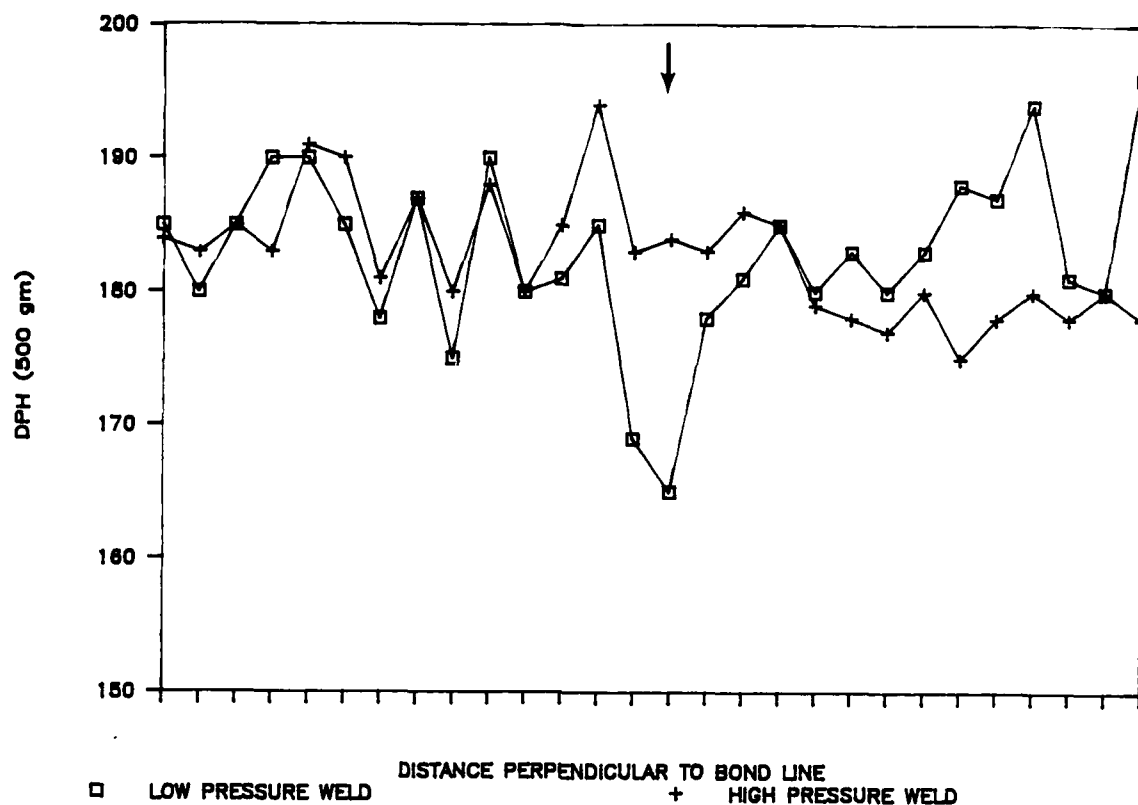


Figure 8. Weld interface microstructure (high axial force) and hardness traverses for inertia-friction welds produced in RS/PM Al-8.7Fe-2.8Mo-1V.

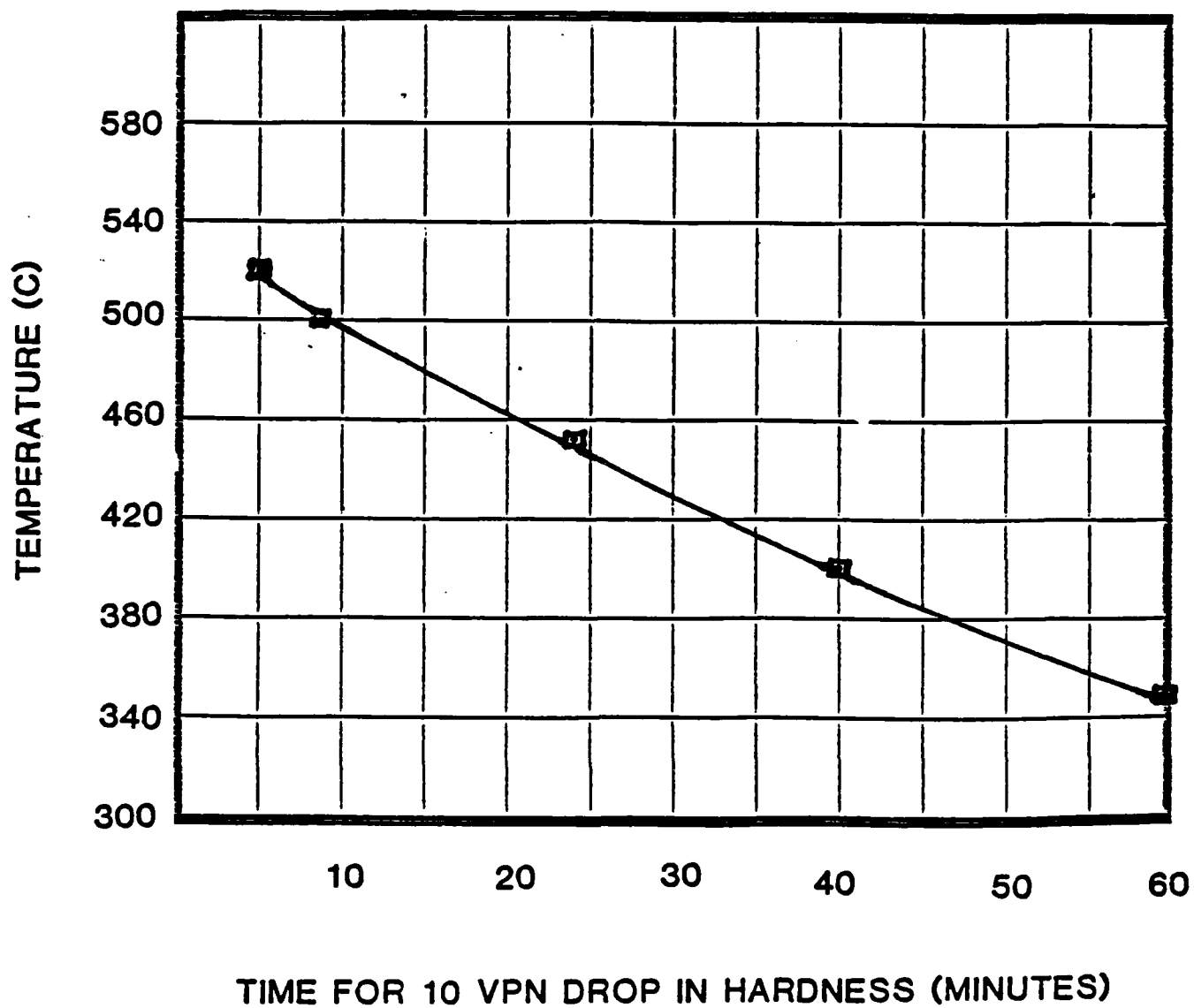


Figure 9. Time for 10 VPN drop in hardness versus temperature for Al-8Fe-4Ce alloy.

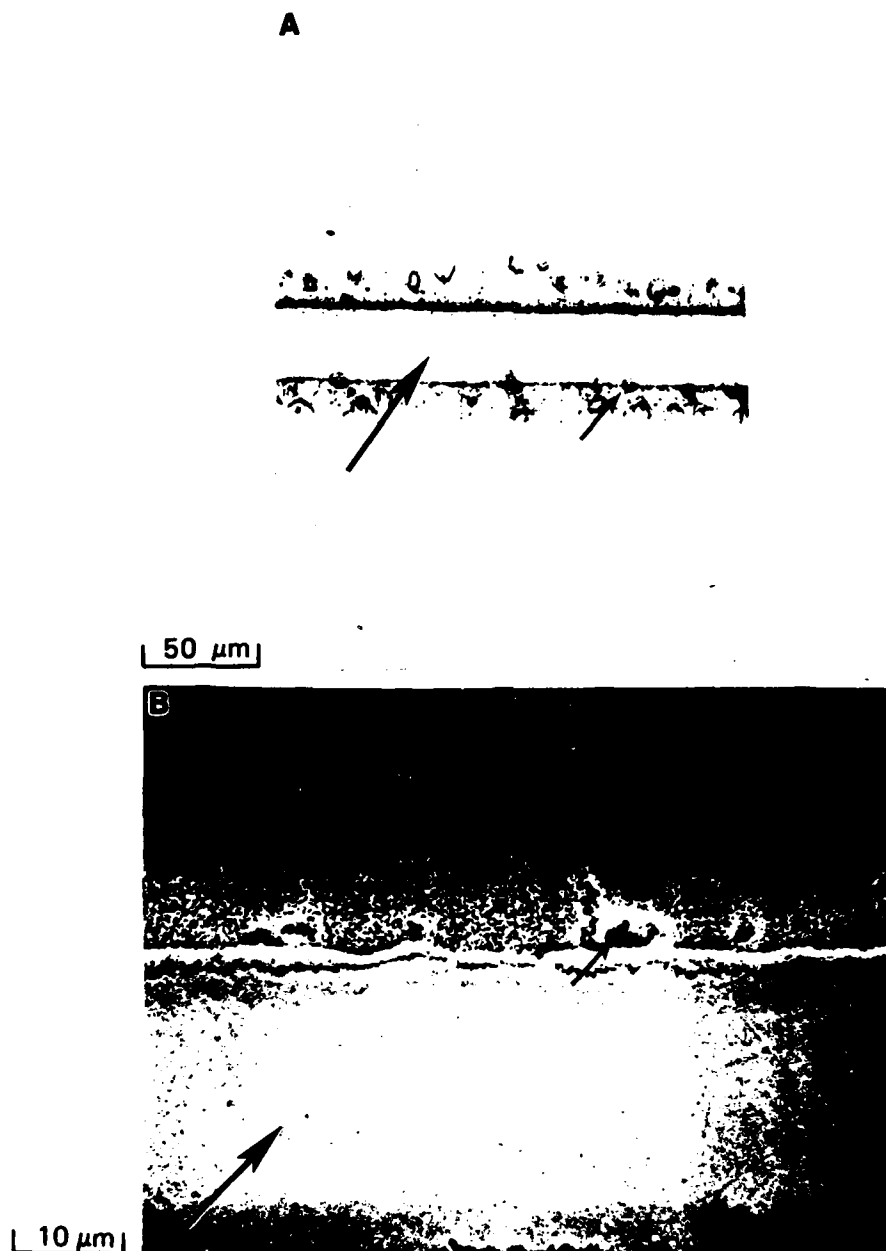


Figure 10. Light (A) and SEM (B) micrographs of diffusion weld in Al-8Fe-4Ce, large arrow indicates intermetallic at bond interface, small arrows indicate Kirkendall pores at base metal/intermetallic interface.

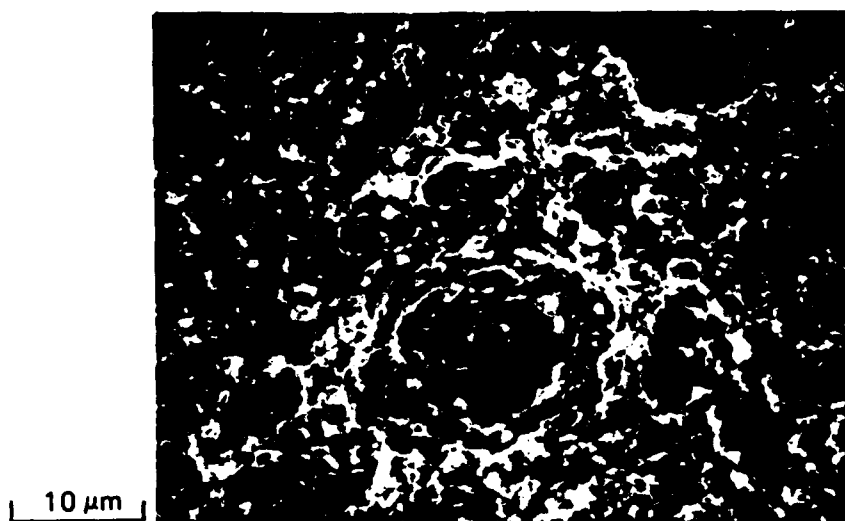
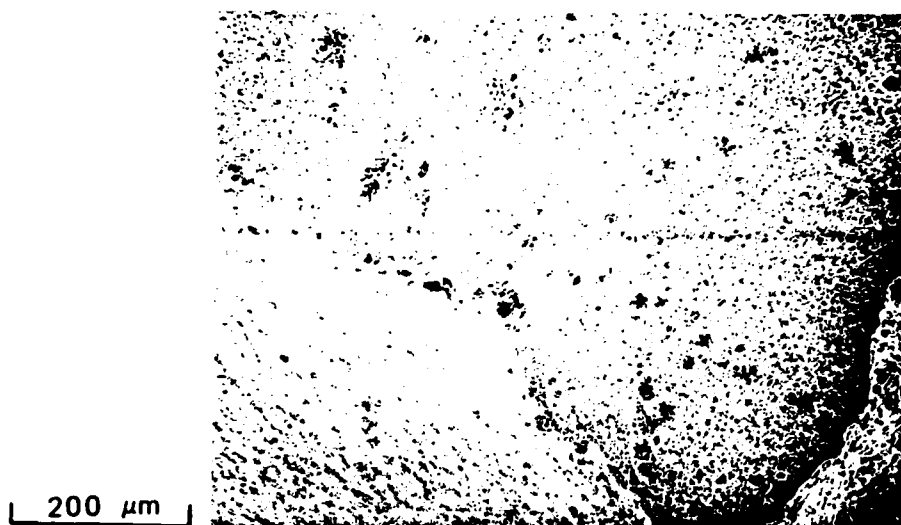


Figure 11. SEM fractographs of diffusion weld fracture surface in Al-8Fe-4Ce. Note Kirkendall pores.

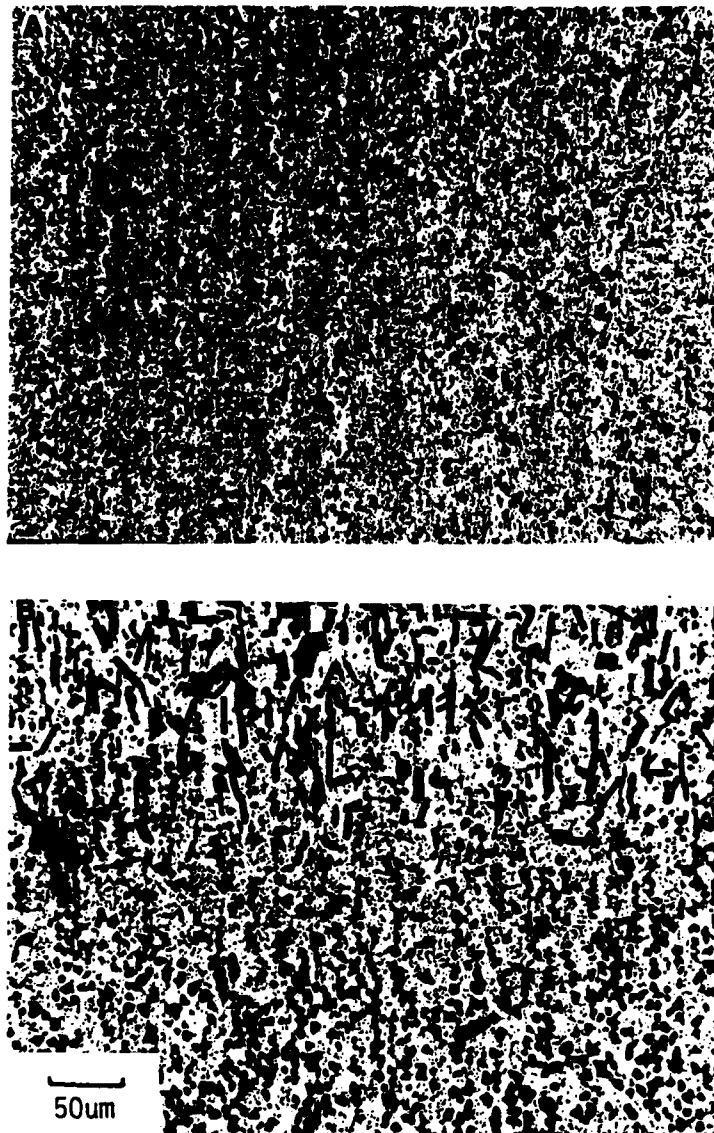


Figure 12.

Light micrographs of Al-4Li-3Cu-1.5Mg-0.18Cr-0.2Zr RS/PM alloy: (A) as-received, (B) vacuum degassed at 538 C/24 hr.

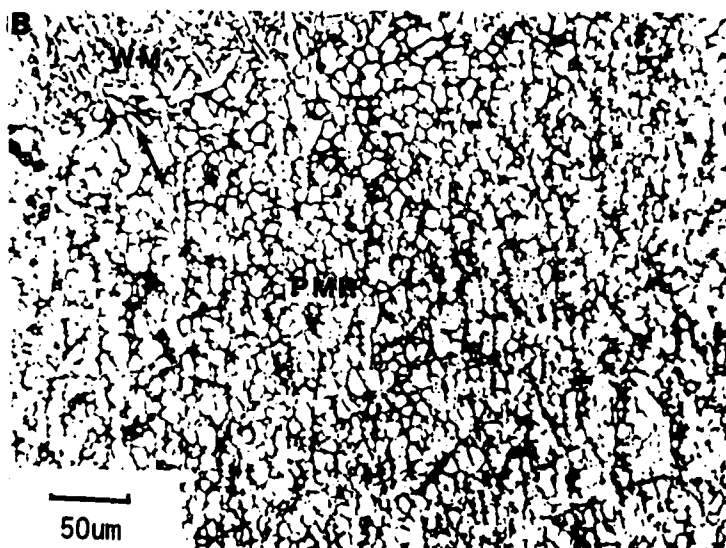
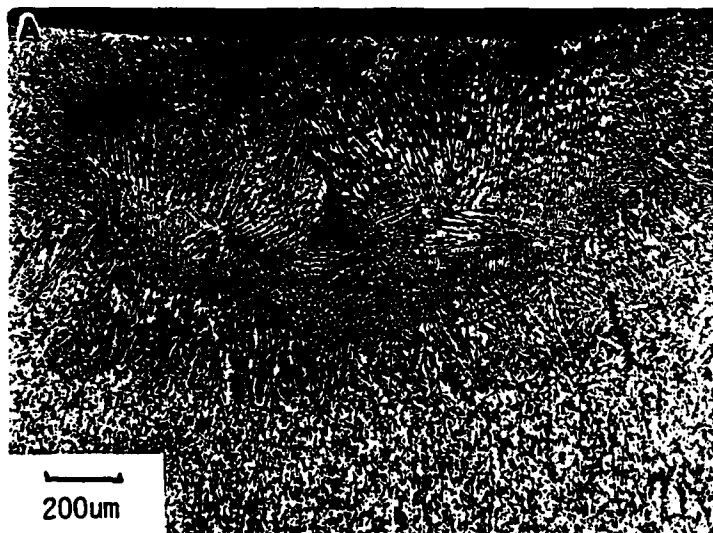


Figure 13.

Light micrograph of gas tungsten-arc weld in RS/PM Al-4Li-3Cu-1.5Mg-0.18Cr-0.2Zr degassed at 510 C/48 hr. Arrows indicate fusion boundary.

APPENDIX IA

W. A. Baeslack III and S. Krishnaswamy, "Electron Beam Weldability of a Rapidly-Solidified Powder Metallurgy Alloy," Advances in Welding Science and Technology, S. A. David, Ed., ASM International (1986) 357-363.

Presented at International Conference on Trends in Welding Research, Gatlinburg, Tennessee, 1986.



ASM INTERNATIONAL
Metals Park, Ohio 44073

**ELECTRON BEAM WELDABILITY OF A RAPIDLY
SOLIDIFIED ALUMINUM ALLOY**

W.A. Baeslack III, S. Krishnaswamy

Department of Welding Engineering
The Ohio State University
190 W. 19th Avenue
Columbus, OH 43210

International Conference on Trends in Welding Research
Gatlinburg, Tennessee, USA
18-22 May 1986

Sponsored by
ASM's Joining Division Council
Co-Sponsored by
American Welding Society and Welding Research Council

"Advances in Welding Science and Technology"
edited by S. A. David

Proceedings published by



8605-006

No part of this paper may be reproduced, stored in a retrieval system, or transmitted, in any form or by any means, electronic, mechanical, photocopying, recording, or otherwise, without the prior written permission of the publisher.

Nothing contained in this paper is to be construed as a grant of any right of manufacture, sale, or use in connection with any method, process, apparatus, product, or composition, whether or not covered by letters patent or registered trademark, nor as a defense against liability for the infringement of letters patent or registered trademark.

SAN: 204-7586
Copyright 1987 ASM International
All rights reserved

This paper is subject to revision. Statements and opinions advanced in papers or discussion are the author's and are his responsibility, no ASM International; however, the paper has been edited by ASM International for uniform styling and format.

Printed and Bound by Publishers Choice Book Mfg. Co.
Mars, Pennsylvania 16046

8605-006

ELECTRON BEAM WELDABILITY OF A RAPIDLY SOLIDIFIED ALUMINUM ALLOY

W.A. Baeslack III, S. Krishnaswamy

Department of Welding Engineering
The Ohio State University
190 W. 19th Avenue
Columbus, OH 43210

ABSTRACT

The electron beam weldability of a rapidly solidified/powder metallurgy Al-8Fe-2Mo alloy has been studied, with the influence of electron beam energy input on the weld zone structure, mechanical properties and fracture behavior specifically investigated. Results indicate that higher weld cooling rates associated with lower energy inputs promote the formation of finer fusion zone primary intermetallic and dendritic alpha structures. These finer structures promote increased weld fusion zone hardness, strength and ductility. The presence of coarse intermetallics near the fusion boundary in low energy input welds and throughout the higher energy input welds promotes lower strength levels and ductility. These reduced properties are attributed to fracture of the intermetallics or delamination of the intermetallic/alpha matrix interfaces.

RECENTLY, THE APPLICATION OF RAPID SOLIDIFICATION/POWDER METALLURGY (RS/PM) technology has led to the development of a new generation of aluminum alloys. These alloys are basically hypereutectic Al-Fe compositions with ternary additions of Mo, Ce or Ni. Through rapid solidification, the formation of equilibrium primary intermetallic phases can be suppressed, with transformation instead occurring to a microeutectic or solute supersaturated dendritic alpha. Subsequent consolidation and thermomechanical processing promote decomposition of these highly metastable structures by the formation of semi-coherent dispersoids which are structurally stable for long times at temperatures up to 230°C. The moderate to high room-temperature strengths provided by these fine microstructures, combined with excellent elevated temperature properties, make these alloys ideal candidates for a variety of structural applications.

If these alloys are to be utilized most effectively, the development of suitable joining

techniques will be required. Considering the strong dependency of Al-Fe alloy properties on the metastable nature of the microstructure, it is apparent that the microstructure must be retained and/or recreated during joining if high joint efficiencies are to be obtained. A previous weldability study of an Al-8Fe-1.7Ni alloy (1) showed that the rapid solidification and cooling rates associated with electron beam welding offer a strong potential for achieving these requirements. This earlier work, however, was limited by a high base alloy gas content and the resulting formation of excessive fusion zone porosity. The objective of the present study was to extend this initial work through characterization of the structure, properties and fracture behavior of electron beam welds in a low hydrogen Al-8Fe-2Mo RS/PM alloy.

EXPERIMENTAL

The Al-8Fe-2Mo alloy studied in this investigation originated as rapidly-solidified powder produced by Pratt and Whitney's "RSR" rotary atomization process (2,3). This process utilizes a rapidly spinning disk to produce powder by centrifugal atomization and helium forced convective cooling to provide droplet cooling rates between 10^4 and 10^6 °C/s. Subsequent inert compaction of the powder and thermomechanical processing provided sheet 1.27 mm in thickness with a chemistry of 8.0 wt%Fe, 2.3 wt%Mo, and less than 1 ppm hydrogen.

Autogenous, full-penetration electron beam welds were produced on the sheet using a range of energy inputs from 15 to 27.6 J/mm. (Specific welding parameters are provided in Table 1.) Following radiographic inspection, the welded coupons were sectioned, mounted, polished and etched (Keller's etch) for metallographic examination using light and scanning-electron microscopy and hardness testing (DPH, 500 g load). Additional coupons were machined into longitudinal and transverse weld tensile specimens

Table 1 - Electron Beam Welding Parameters¹ and Weldment Characteristics

Weld #	Travel speed mm/sec(in/min)	Energy input J/mm(J/in)	DPH at weld center	Threshold bending strain %	UTS MPA (ksi)		EL %	
					Trans.	Long.	Trans.	Long
1	12.7(30)	27.6(701)	110	3.3	--	--		
2	14.8(35)	23.6(600)	116	3.3	--	--		
3	16.9(40)	23.6(600)	116	4	330(46.5)	445(64.2)	1.6	5.8
4	16.9(40)	20.7(526)	119	4	--	--		
5	23.3(55)	19.3(490)	120	4	370(53.5)	470(67.7)	5.6	10.0
6	19.1(45)	18.4(467)	121	4	--	--		
7	21.2(50)	16.5(419)	126	4	--	--		
8	23.3(55)	15(381)	130	5	--	--		

¹Voltage - 100 KV, current 3.5 ma except for #3 (4.0ma) and #5 (4.5ma)

(gage length = 12.7mm) and longitudinal weld bend specimens. Finally, scanning-electron microscopy (SEM) and energy dispersive X-ray analysis (EDX) were employed for fractography of bend and tensile specimens.

RESULTS AND DISCUSSION

WELD INTEGRITY - Previous studies on the fusion welding of RS/PM aluminum alloys have shown hydrogen-induced porosity to be a significant problem (4). The source of hydrogen is the hydration of aluminum oxide on powder surfaces during and subsequent to atomization. The oxide thickness and the degree of hydration are dependent on the atomization process (i.e. air or inert gas) and the manner of powder storage, handling and consolidation. Although hydrogen in the consolidated product can be reduced by hot vacuum degassing prior to final consolidation, such degassing temperatures for the Al-Fe alloys are limited by the coarsening and softening of the metastable dispersoid microstructures. In the present study, total inert atomization,

handling and processing of the powder minimized hydration and provided a base alloy with below 1 ppm hydrogen. Correspondingly, radiographic examination of the weldments and metallographic study found minimal evidence of porosity.

WELD STRUCTURE - Characterization of the electron beam weld macrostructure using light microscopy (Fig. 1A) showed two distinct regions within the fusion zone: a dark-etching central region and a light-etching region adjacent to the fusion boundary. Examination of these structures at increased magnification using SEM (Fig. 1B) showed the central region to consist of extremely fine, nearly equiaxed primary intermetallics (Al₃Fe type) in a matrix of fine dendritic alpha (Figs. 2B and D) and the fusion boundary region to consist of much coarser, high aspect ratio intermetallics in a matrix of coarser dendritic alpha (Figs. 2D and D). Although not observed with light or SEM microscopy, previous scanning-transmission electron microscopy studies(4) suggest the presence of fine intermetallic at dendrite boundaries resulting

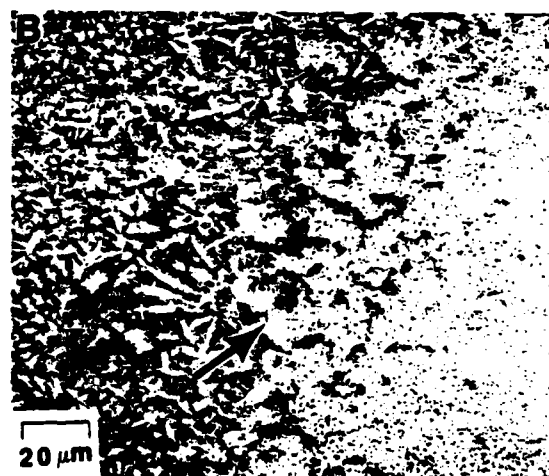
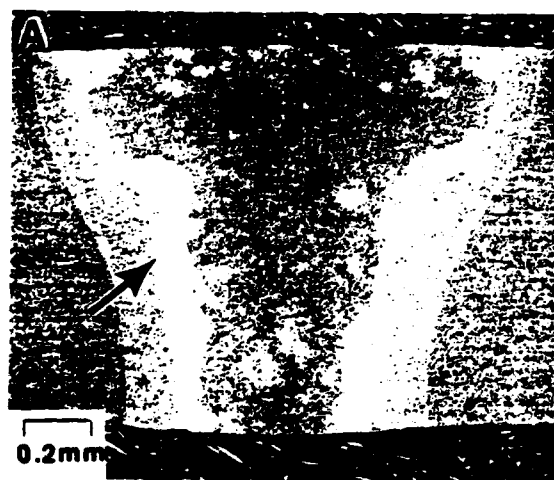


Fig. 1 - Light macrograph (A) and SEM micrograph (B) of electron beam weld produced with energy input of 15 J/mm. Arrows indicate fusion boundary.

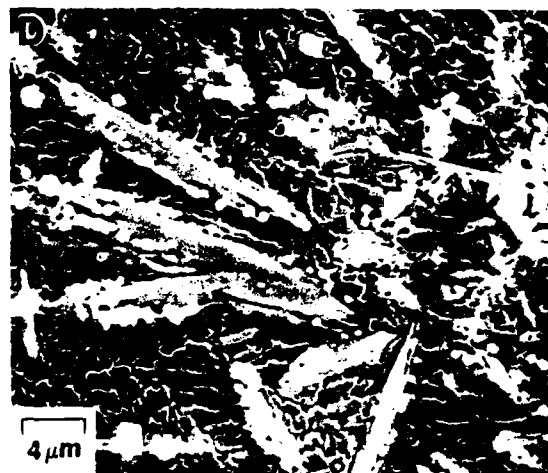
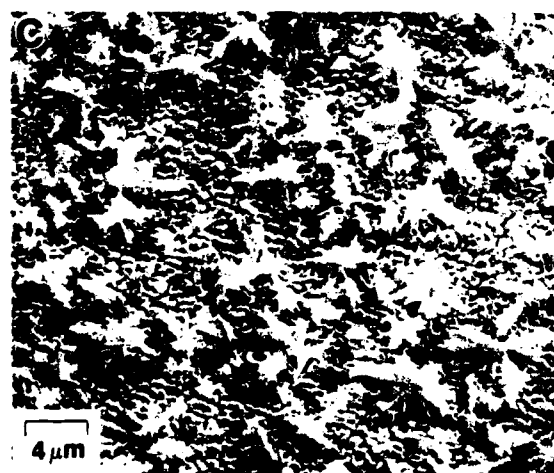
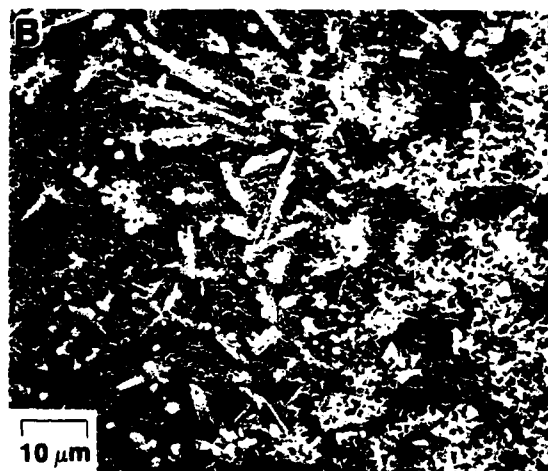
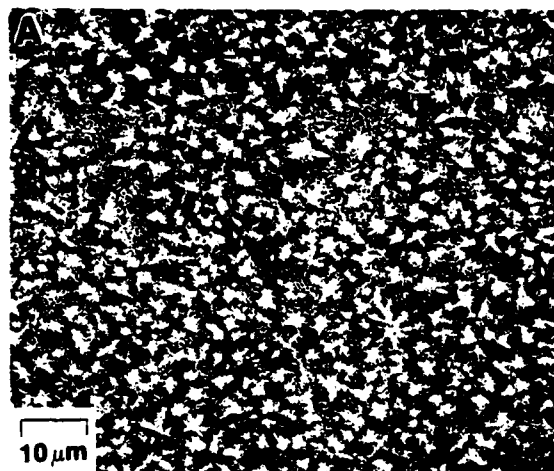


Fig. 2 - SEM micrographs of region in Fig. 1B at increased magnification showing electron beam weld fusion zone center (A,C) and fusion boundary region (B,D)

from eutectic decomposition of the final liquid to solidify. An increase in the weld energy input was shown to promote an increase in the proportion of light to dark-etching regions and also in the microstructure coarseness of both regions. Correlation of dendrite spacings in the central fusion zone regions with previous dendrite spacing/cooling rate relationship data for aluminum alloys (5) indicated cooling rates of between 10^3 and 10^4 °C/s, which were consistent with cooling rates calculated using an analytical 2D heat flow model. Despite these moderately rapid cooling rates, it was not possible to suppress intermetallic nucleation even for the lowest energy inputs in the present study.

Solidification of the electron beam welds occurred primarily by the equiaxed growth of fine alpha aluminum dendrites from intermetallic nuclei. Considering the melting point differences between the Al_3Fe intermetallic ($\approx 1150^\circ C$) and the alpha aluminum matrix ($\approx 650^\circ C$), the possibility that base metal dispersoids remained unmelted and provided these nucleation sites in

the fusion zone becomes apparent. The potential for this phenomena was examined analytically using particle dissolution equations (6,7) and experimentally by producing identical electron beam welds on base metals exhibiting a wide range of initial dispersoid sizes. Although details of these analyses are not presented in this paper, results presently suggest that the base metal dispersoids were completely dissolved in the central fusion zone region during welding.

In contrast, dissolution near the fusion boundary was found to be incomplete (Fig. 1B). In this region, the dispersoids likely served as growth centers for the coarser intermetallic particles observed and possibly promoted the stagnation of fluid flow. Such stagnation may explain the slower cooling rates experienced in this region versus the weld center, as indicated by coarser intermetallic and alpha dendrite sizes.

It is of interest to note that the coarse fusion boundary structure contrasted previous results on Al-8Fe-1.7Ni (1), which found an absence of primary intermetallic formation at the fusion line (epitaxial solidification to microeutectic)

and a gradual increase in the quantity and size of intermetallics toward the weld centerline. This structure was attributed to the steep temperature gradient and rapid cooling rates experienced near the fusion boundary of these high depth-to-width ratio electron beam welds which inhibited nucleation and growth of the intermetallics. A possible explanation for the differences observed in the present study is that the electron beam welds on the thin Al-8Fe-2Mo sheet exhibited much shallower temperature gradients, which was also suggested by the observation of nearly entirely non-epitaxial, equiaxed grain growth in the fusion zone. Indeed, high depth-to-width ratio electron beam welds produced on 12.5 mm thick Al-8Fe-2Mo plate have shown a structure more comparable to that of the Al-8Fe-1.7Ni welds (4).

Also evident in Fig. 1A is the presence of a heat-affected zone adjacent to the fusion boundary. SEM analysis of this region found a noticeable coarsening of the dispersoid structure as compared to the unaffected base metal.

WELD PROPERTIES - Results of mechanical property tests are summarized in Table 1 and Figures 3 and 4.

Figure 3 shows a hardness traverse across an electron beam weld produced at the lowest energy input (15 J/mm). As indicated, the fine intermetallic/alpha dendrite structure in the center of the fusion zone exhibited a hardness comparable to the unaffected base metal (DPH 130 versus 126). However, in the weld HAZ and more significantly in the fusion zone adjacent to the fusion boundary, the hardness dropped appreciably which was consistent with the coarser intermetallic and dendrite structures observed in this region. As Table 1 indicates, the hardness of the fine central fusion zone regions increased with decreasing weld energy input and increasing

cooling rate, which corresponded to the increase in microstructure fineness.

The tensile strengths of the longitudinal weld tensile specimens were found to increase with increased cooling rate (Fig. 4), with the more rapidly cooled specimen exhibiting a tensile strength approximately 90% of the typical base metal strength for this alloy (3). Consistent with the hardness traverses, transverse weld tensile specimens failed at lower strength levels through the coarse fusion boundary region in the weld fusion zone. However, weld efficiency values for the more rapidly cooled welds exceeded 73%, which was relatively high for aluminum alloy weldments.

Table 1 summarizes bend ductility test results, and shows an improvement in ductility with increased cooling rate. It is important to note that crack initiation in these specimens occurred exclusively in the coarse fusion zone microstructure directly adjacent to the fusion line. Tensile ductilities for both longitudinal and transverse specimens were also higher for the more rapidly cooled welds.

FRACTURE CHARACTERISTICS - Figure 5 illustrates the longitudinal (A and B) and transverse (C and D) tensile specimen fracture surfaces for a moderate energy input electron beam weldment ($E_{in} = 23.6$ KJ/mm). Differences in the fracture behavior between the unaffected base metal and the fusion zone were visible even at low magnification (Fig. 5A), and ranged from a flat topography in the base metal to a much more irregular topography in the fusion zone. Figure 5B reveals that at higher magnification three different fracture surfaces could be observed on the longitudinal weld specimens. The unaffected base metal exhibited a ductile-appearing, dimpled fracture which was associated with the fine dispersoid structure in this region

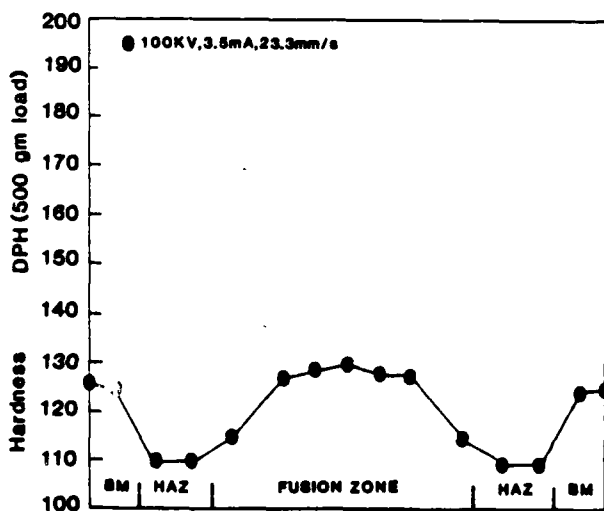


Fig. 3 - Diamond pyramid hardness (DPH) traverse across electron beam weld ($E_{in} = 15$ J/mm).

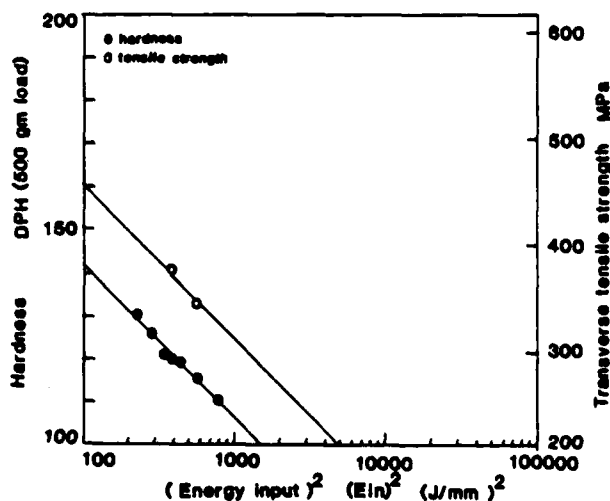


Fig. 4 - Diamond pyramid hardness at center of weld fusion zone and transverse weld tensile strength versus electron beam weld energy input.

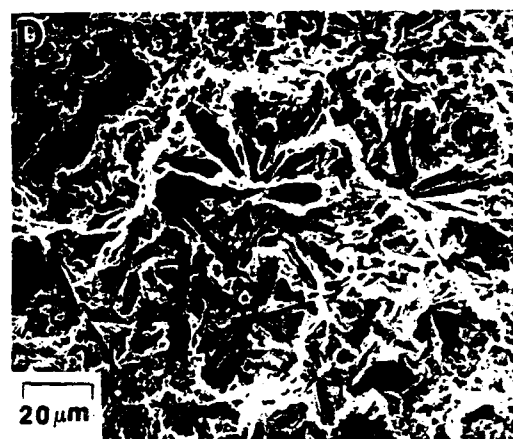
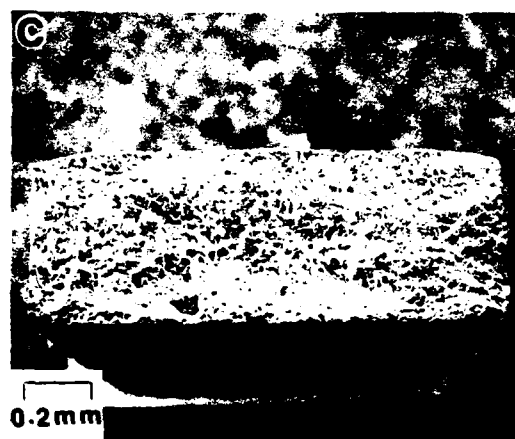
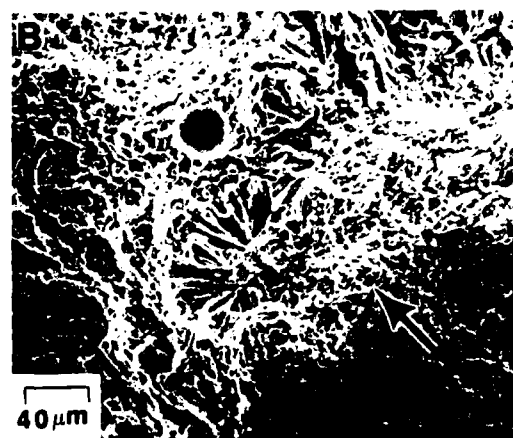
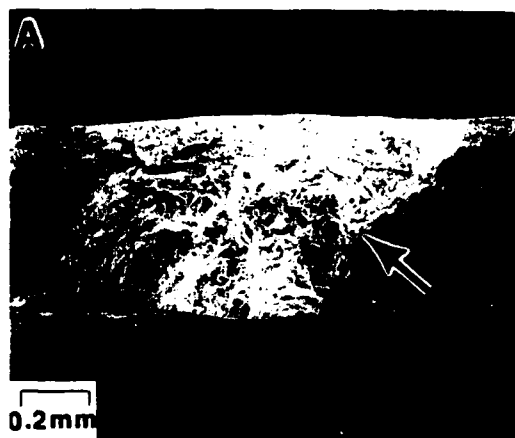


Fig. 5 - Fracture surfaces of longitudinal (A,B) and transverse (C,D) weld tensile specimens ($E_{in} = 19.3 \text{ J/mm}$). Arrows in (A) and (B) indicate approximate fusion boundary.

(Fig. 6A and D). In the central fusion zone, where the intermetallic structure was coarser, considerable ductile-appearing fracture was again observed (Figs. 6B and E). However, SEM/EDX analysis also revealed the presence of intermetallics on the surface, suggesting possible local fracture by delamination of the α /intermetallic interfaces. Evidence of intermetallic fracture and delamination was most apparent in the fusion zone adjacent to the fusion boundary, where the coarse intermetallic structure promoted low ductility fracture (Figs. 6C and F). Relatively little evidence of ductile fracture was observed in this region. In the transverse weld tensile specimens, the entire fracture surface exhibited this third type of fracture, since failure occurred entirely in the fusion zone adjacent the fusion boundary. (Figs. 5C and D).

SUMMARY

The results described above clearly show the importance of maintaining a fine intermetallic/ α aluminum dendrite structure in providing optimum weld strength and ductility. It is also evident that the weld fusion zone adjacent to the fusion boundary represents the "weak link" in the

weldment, and that if properties are to be improved this region must be eliminated. Continuing work on the electron beam welding of the Al-8Fe-2Mo alloy sheet and plate is optimizing parameters such that depth-to-width ratios are increased and optimized. The steeper temperature gradients and more rapid cooling rates associated with these welds will promote finer fusion zone structures and potentially suppress primary intermetallic formation, thereby providing enhanced weld properties.

REFERENCES

- (1) Baeslack, W.A. III, *Metallography*, 18, 73-82 (1985).
- (2) Adam, C.M. and Bourdeau, R.G., "Rapid Solidification Processing, Principles and Technologies II," p. 246, Mehrabian, R., Kear, B.H. and Cohen, M., Eds., Claitors Publishing, Baton Rouge, Louisiana (1980).
- (3) Adam, C.M., "Rapidly Solidified Amorphous and Crystalline Alloys," p. 411, Kear, B.H., Giessen, B.C. and Cohen, M., Eds., Elsevier Science Publishing Co., New York (1982).
- (4) Baeslack, W.A. III, Unpublished Research, The Ohio State University, Columbus, OH 43210, 1982.- 1986.

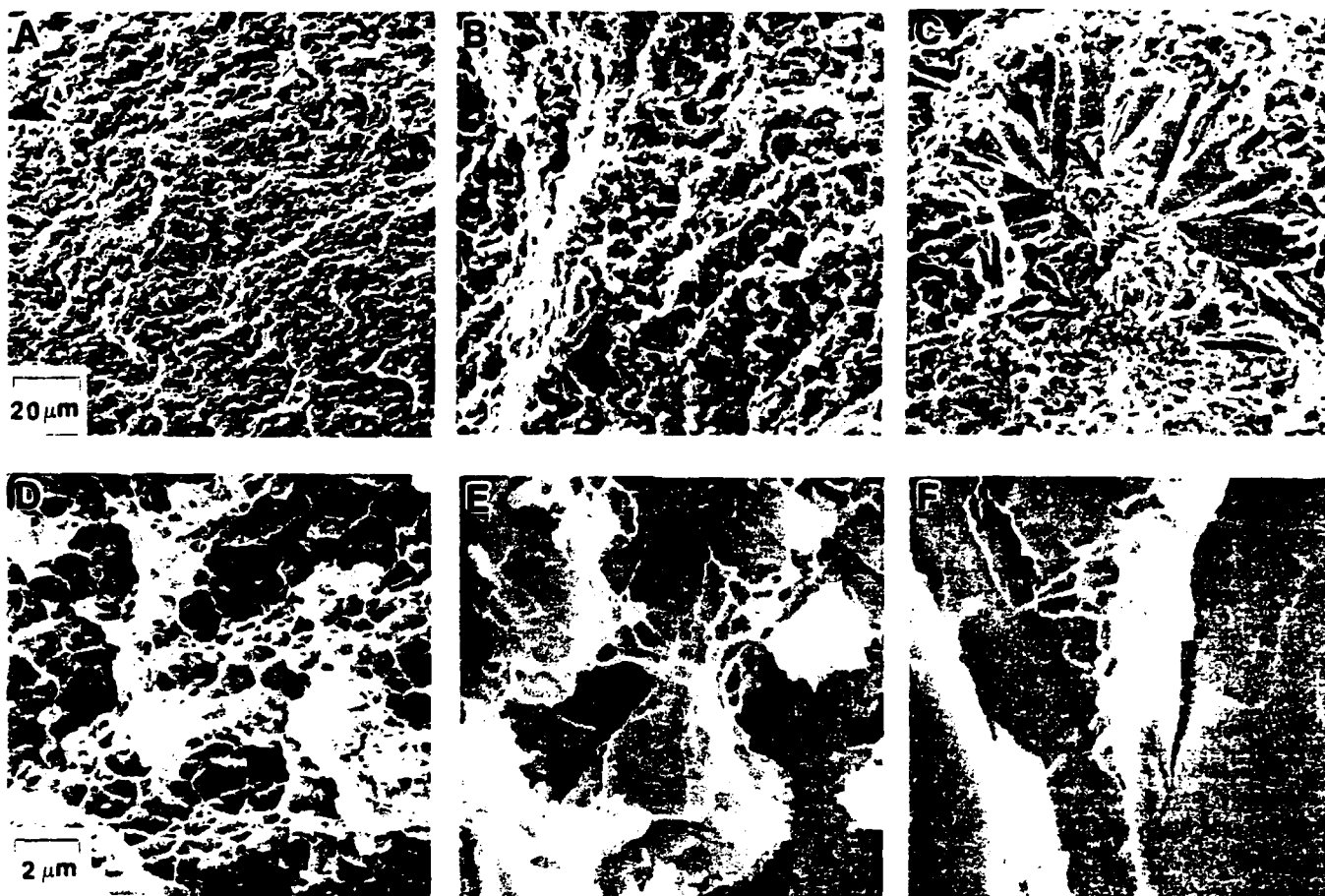


Fig. 6 - Fractographs of longitudinal weld tensile specimen in Fig. 5B at increased magnification showing unaffected base metal (A,D), fusion zone center (B,E) and fusion zone adjacent to the fusion boundary (C,F).

REFERENCES (continued)

- (5) Jones, H., "Rapid Solidification of Metals and Alloys," p. 42, Institution of Metallurgists, London (1982).
- (6) Doremus, R.H., "Rates of Phase Transformations," p. 18, Academic Press Inc., Orlando, Florida (1985).
- (7) Geiger, G.H. and Poirier, D.R., "Transport Phenomena in Metallurgy," p. 541-542, Addison Wesley Publishing Co., New York (1973).

ACKNOWLEDGEMENT

The authors express their gratitude to Dr. Andrew Crowson and the Army Research Office for their financial support. In addition, we are indebted to the Materials Laboratory/Air Force Wright Aeronautical Laboratories for providing the alloy studied in this investigation.

APPENDIX IB

S. Krishnaswamy and W. A. Baeslack III, "Structure and Properties of Rapidly-Solidified Weldments in RS/PM Al-8Fe-2Mo," Materials Science and Engineering (in press).

Presented at RQ-6, Montreal, 1987.

Structure, Properties and Fracture of Electron Beam Welds in RS-PM Al-8Fe-2Mo*

S. KRISHNASWAMY and W. A. BAESLACK III

Department of Welding Engineering, The Ohio State University, Columbus, OH 43210 (U.S.A.)

Abstract

Electron beam welds were produced in rapidly-solidified, powder metallurgy (RS-PM) Al-8wt.%Fe-2wt.%Mo sheet using a range of energy inputs and metallurgically characterized with respect to microstructure, mechanical properties and fracture behavior. A reduction in the electron beam energy input required to produce autogenous, full-penetration welds and the associated increase in weld solidification and cooling rates were found to promote increasingly finer fusion zone microstructures comprising primary intermetallics and dendritic alpha aluminum (zone B type). Welds produced at the lowest energy inputs exhibited fusion zone hardnesses superior to that of the base metal, joint efficiencies exceeding 85% and acceptable ductilities. The use of a minimal energy input also prevented the formation of a structurally-coarsened region near the fusion boundary which served as the weak link in higher energy input weldments. Weld failure in this coarsened region was associated with delamination of the coarse intermetallic-alpha aluminum interfaces.

1. Introduction

Dispersion-strengthened aluminum alloys produced via rapid solidification-powder metallurgy (RS-PM) represent a relatively new and unique family of aluminum alloys. These alloys are basically hypereutectic Al-Fe compositions with ternary additions of molybdenum, cerium or nickel. Through rapid solidification, the formation of coarse, primary intermetallic phase is suppressed and the liquid solidifies instead to a fine, solute supersaturated alpha phase or microeutectic. Proper consolidation and thermomechanical processing of the RS particulates promote the formation of extremely fine, thermally-stable dispersoids which provide moderate to high room-temperature strengths and excellent elevated-temperature properties.

As potential replacements for conventional aluminum and titanium-based alloys in many structural applications, the Al-Fe-X alloys will commonly require joining. Considering the strong dependency of alloy mechanical properties on the metastable nature of the microstructure, it is apparent that the base metal microstructure must either be retained or recreated during joining if high joint efficiencies are to be achieved. Previous work by the authors [1] on RS-PM Al-8wt.%Fe-1.7wt.%Ni has shown that the rapid solidification and cooling rates provided by electron beam welding can offer a strong potential for recreating as RS fusion zone (FZ) microstructure and minimizing structure coarsening in the adjacent heat-affected zone (HAZ). A more recent study [2] on the electron beam weldability of Al-8wt.%Fe-2wt.%Mo (Al-8Fe-2Mo) 1.27 mm thick was successful in producing quality weldments exhibiting zone B FZ microstructures and joint efficiencies exceeding 70%. This study identified a region of structural coarsening in the fusion zone which represented the weak link across the weld zone, and which will require elimination if weld mechanical properties approaching that of the base metal are to be achieved.

The present study involved the generation and metallurgical characterization of electron beam weldments in an Al-8Fe-2Mo sheet 0.65 mm thick. Welding parameters which maximized weld solidification and cooling rates were used in an effort to optimize FZ and HAZ strength and eliminate the coarsened fusion boundary region.

2. Experimental procedure

The Al-8Fe-2Mo alloy investigated in this study originated as rapidly-solidified powder produced by rotary atomization [3]. Forced convective cooling with helium provided droplet cooling rates between 10^4 and 10^6 °C s⁻¹ and minimized surface oxide and hydrate formation commonly associated with air atomization. Subsequent inert compaction and thermomechanical processing resulted in sheet 0.65 mm thick which contained below 1 ppm hydrogen.

*Paper presented at the Sixth International Conference on Rapidly Quenched Metals, Montréal, August 3-7, 1987.

TABLE 1 Electron beam welding parameters^a and weldment characteristics

Weld number	Travel rate (mm s ⁻¹)	Energy input (J mm ⁻¹)	FZ cooling rate ^b (°C s ⁻¹)	DPH at FZ center ^c	Threshold bending strain (%)
1	14.8	8.4	3 700	116	7.5
2	16.9	7.4	4 800	120	7.5
3	19.0	6.6	6 100	124	7.5
4	21.2	5.9	7 500	126	7.5
5	23.3	5.4	9 100	128	7.5
6	25.4	4.9	10 800	129	7.5
7	27.5	4.5	12 700	138	14.0
8	31.7	3.9	17 000	142	14.0
Base metal	—	—	—	137	14.0

^a Voltage, 100 kV; current, 1.25 mA.

^b Determined using two-dimensional analytical heat flow model.

^c Diamond pyramid hardness at 500 gf load.

Autogenous, full-penetration electron beam welds were produced on the sheet using high voltage (100 kV), low current (1.25 mA) and a range of travel rates from 14.8 to 31.7 mm s⁻¹, thereby providing a range of energy inputs from 8.4 to 3.9 J mm⁻¹ (Table 1). After radiographic inspection, the welded coupons were prepared for metallographic evaluation using light and scanning electron microscopy (SEM) and diamond pyramid hardness (DPH) testing (500 gf load). Additional coupons were machined into longitudinal weld bend specimens and transverse weld tensile specimens (gage length 12.7 mm). Finally, SEM analysis was conducted on bend and tensile specimen fracture surfaces for correlation with microstructural features.

3. Results and discussion

Radiographic inspection and metallographic examination of the weldments revealed only minimal evidence of isolated, spherical porosity, which was consistent with the low hydrogen content exhibited by the inertly-atomized and processed alloy. Neither solidification nor solid-state weld cracking was observed.

Examination of the electron beam weld macrostructures using light microscopy revealed distinct differences between welds produced at high and low energy (Figs. 1(a) and 2(a)). High energy welds were characterized by two distinct regions within the weld FZ: a dark-etching central region and a light-etching region adjacent to the fusion boundary. Observation of these regions at increased magnification using SEM showed the central region to consist of nearly equiaxed grains of fine, dendritic alpha aluminum (Fig. 1(b)). Despite significant differences in the melting points of the base metal intermetallics (about 1150 °C) and the alpha aluminum matrix (about 650 °C), both theoret-

ical particle dissolution analysis and metallographic examination suggested complete melting and resolidification in this central FZ region. As shown in Fig. 1(c), the fusion boundary region consisted of appreciably coarser, high aspect ratio intermetallics in a matrix of coarser dendritic alpha. This coarsened region probably originated from sluggish fluid flow near the fusion line which reduced the liquid temperature and thereby prevented complete melting or dissolution of base metal dispersoids. These undissolved dispersoids subsequently served as growth centers for the coarse intermetallics. The width of this coarsened region was found to decrease with a decrease in weld energy input (increase in cooling rate) and was essentially eliminated in the most rapidly-cooled welds.

Welds produced at the lowest energy levels also exhibited both dark- and light-etching regions within the FZ. As above, the dark-etching regions comprised fine, equiaxed primary intermetallics in a matrix of fine dendritic alpha, with both the intermetallics and alpha dendrites becoming progressively finer with lower energy inputs and associated higher cooling rates (Figs. 2(b) and (c)). Light-etching regions consisted of extremely fine, widely spaced primary intermetallics which served as growth centers for large, equiaxed grains of fine alpha aluminum and/or microeutectic. Although cooling rates through the solidification temperature range in the fastest cooled welds were calculated to be between 10⁴ and 10⁵ °C s⁻¹ (Table 1), primary intermetallic nucleation could not be completely suppressed, resulting in a zone B type microstructure.

Figures 1(a) and 2(a) also indicate the presence of a heat-affected zone adjacent to the fusion boundary, which was characterized by noticeable coarsening of base metal dispersoids.

As shown in Figure 3, increased weld cooling rates promoted increases in FZ hardness, which was

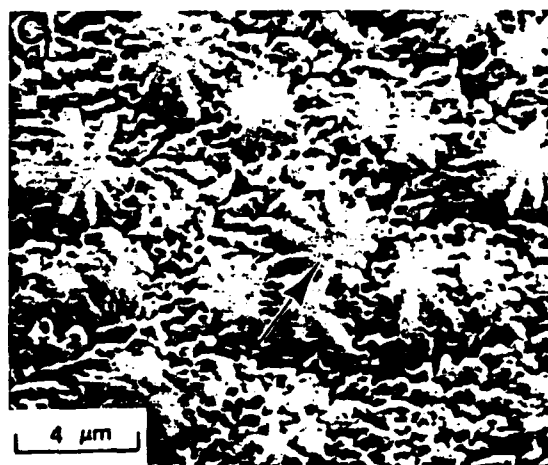
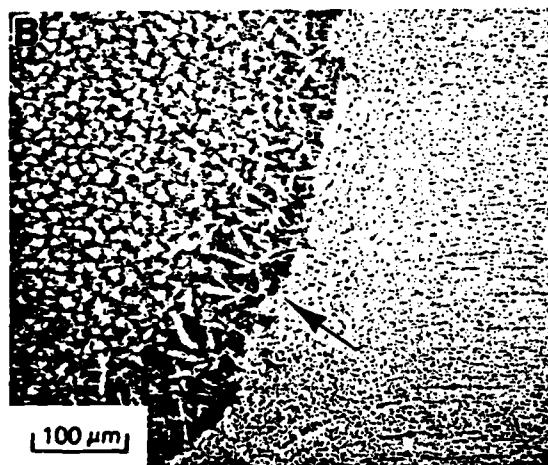
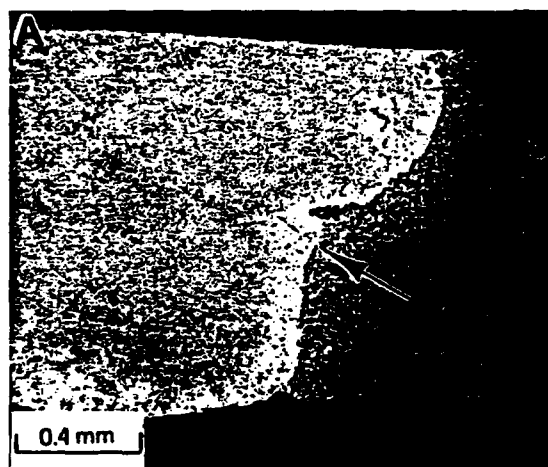


Fig. 1. Light micrograph (a) and scanning electron micrographs (b, c) of electron beam weld produced in Al-8Fe-2Mo with energy input of 6.6 J mm^{-1} . Arrows indicate fusion boundary.

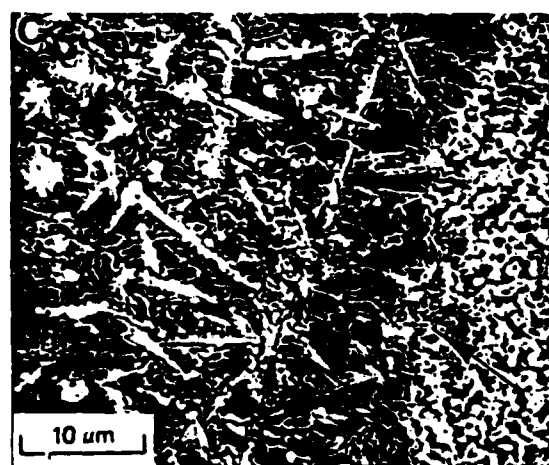
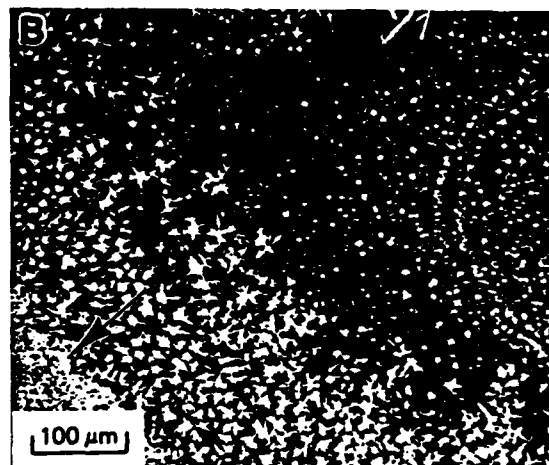
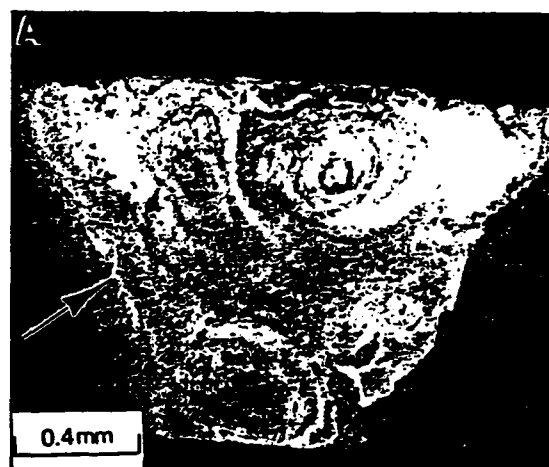


Fig. 2. Light micrograph (a) and scanning electron micrographs (b, c) of electron beam weld produced in Al-8Fe-2Mo with energy input of 4.5 J mm^{-1} . Arrows in (a) and (b) indicate fusion boundary, arrow in (c) indicates primary intermetallic.

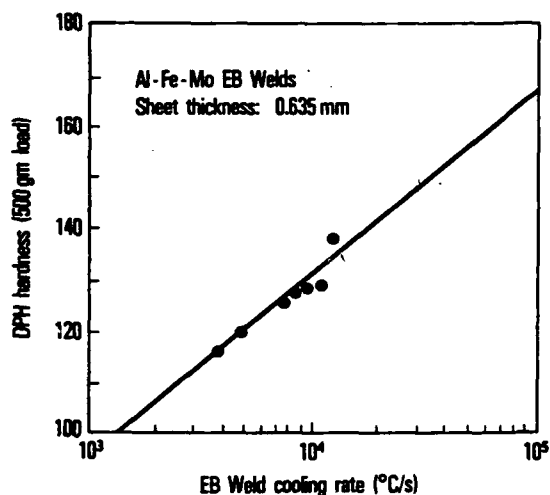


Fig. 3. Diamond pyramid hardness at center of weld fusion zone vs. electron beam weld cooling rate.

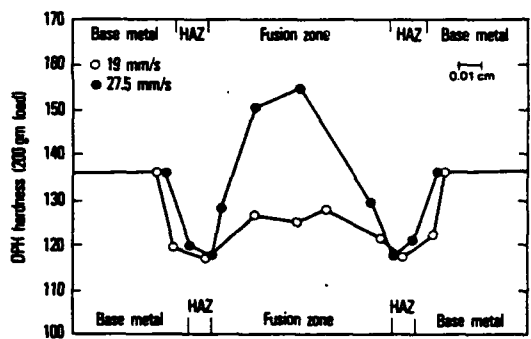


Fig. 4. Diamond pyramid hardness traverses across electron beam welds produced in Al-8Fe-2Mo with energy inputs of 6.6 J mm^{-1} and 4.5 J mm^{-1} .

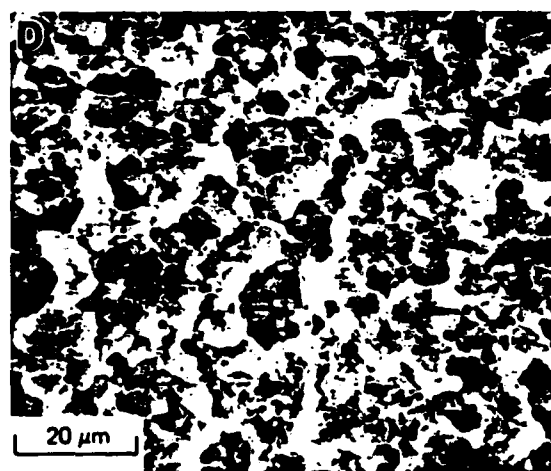
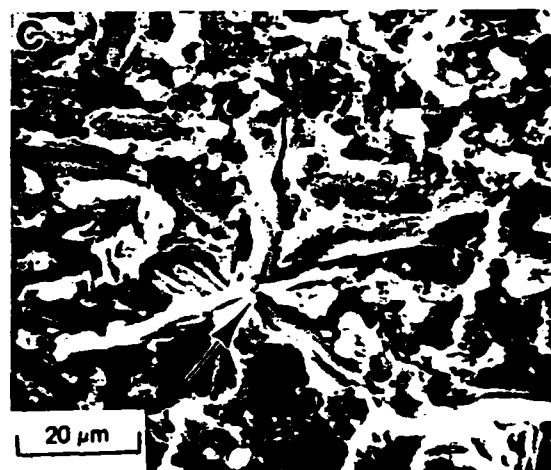
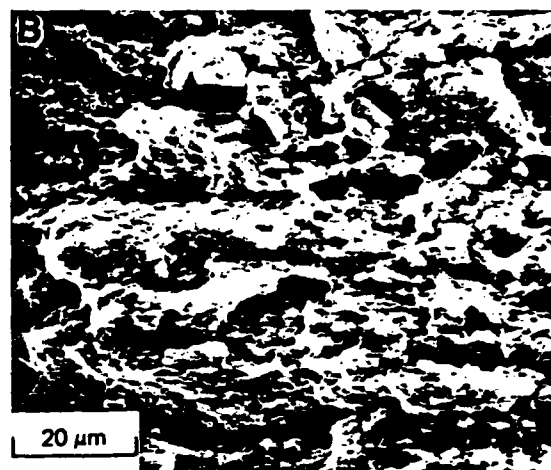
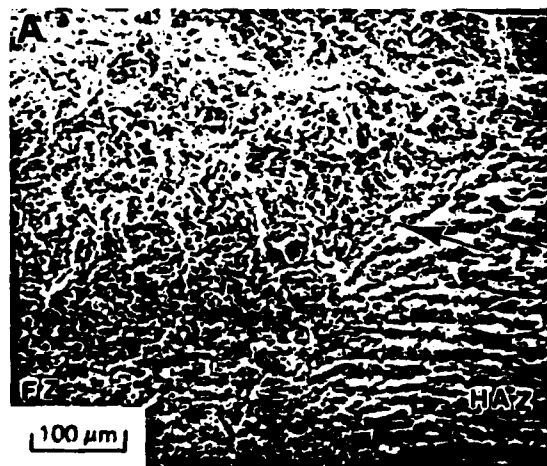


Fig. 5. SEM fractographs of longitudinal-weld oriented bend test specimen (energy input of 6.6 J mm^{-1}): (a) fusion boundary region at low magnification, arrow indicates fusion line; (b) heat-affected zone; (c) fusion zone adjacent to fusion line, arrow indicates coarse intermetallic; (d) center of fusion zone.

consistent with the observed microstructure refinement. Figure 4, however, indicates that despite FZ hardness exceeding that of the base metal and elimination of the coarsened fusion boundary region for the lowest energy welds, reduced hardnesses were still observed in the weld HAZ. As indicated, these near-HAZ hardnesses were comparable with those of the coarsened fusion boundary region and HAZ for welds produced at high energy inputs.

Transverse tensile testing of welds produced at lowest energy inputs determined joint efficiencies to exceed 85% (weld tensile strength of 360 MPa), which represented a marked improvement over 70% values recorded previously for higher energy input welds [2]. Consistent with the hardness transverse, the transverse weld tensile specimens failed in the weld HAZ at ductilities below that of the base metal (1.6% and 9.7% elongation respectively).

Table 1 also summarizes the longitudinal bend ductility test results, and shows an improvement in the threshold bending strain with increased FZ cooling rate. Crack initiation in these welds occurred near the fusion line.

Figure 5 illustrates the fracture surface of a longitudinal-weld oriented bend specimen for a high energy (6.0 J mm^{-1}) weld. Variations in the fracture behavior between the unaffected base metal and the fusion zone were evident even at low magnification (Fig. 5(a)), ranging from a flat, textured topography in the base metal and HAZ to a more irregular fusion zone topography.

Observation at increased magnification (Figs. 5(b)–(d)) revealed a ductile-appearing, dimpled fracture, with microvoids nucleating at the fine dispersoid- α matrix interfaces. Delamination along the coarse intermetallic- α matrix interface was clearly observed in the coarsened fusion boundary

region, and probably promoted the low-ductility fracture initiation observed in bend specimens (Fig. 5(c)). Although this coarse delamination-type fracture was not observed in weld-bend and transverse tensile specimens produced at low energy, a noticeable coarsening of dimples in the HAZ compared with the unaffected base metal correlated well with the structural coarsening and low hardness of this region.

4. Summary

Results of this investigation have demonstrated that defect-free, high integrity welds can be produced in RS-PM Al-8Fe-2Mo thin sheet using the electron beam welding process. Minimization of the weld energy input required to obtain full penetration promoted an extremely fine, predominantly zone B microstructure which exhibited high hardness and strength. Dispersoid coarsening and associated softening in the weld HAZ promoted preferential fracture in this region. However, excellent joint efficiencies of over 85% were obtained at room temperature.

Acknowledgment

The authors express their gratitude to the Army Research Office for their financial support under contract DAAG29-84-K-0176.

References

- 1 W. A. Baeslack III, *Metallography*, (1985) 73–82.
- 2 W. A. Baeslack III and S. Krishnaswamy, in S. A. David (ed.), *Advances in Welding Science and Technology*, ASM International, Metals Park, OH, 1987, pp. 357–362.
- 3 C. M. Adam and R. G. Bourdeau, in R. Mehrabian, B. H. Kear and M. Cohen (eds.), *Rapid Solidification Processing, Principles and Technologies II*, Claitors, Baton Rouge, LA, 1980, p. 246.

APPENDIX IC

W. A. Baeslack III and K. Hagey, "Inertia-Friction Welding of a Rapidly-Solidified, Powder Metallurgy Aluminum Alloy," Welding Journal (Research Supplement) (in press).

Presented at 1987 AWS National Meeting, Chicago, ILL.

INERTIA-FRICTION WELDING OF RAPIDLY SOLIDIFIED POWDER METALLURGY ALUMINUM

W. A. Raeslack III* and K. S. Hagey**

*Department of Welding Engineering
The Ohio State University
Columbus, Ohio 43210

**Westinghouse Electric Company
Jefferson City, Missouri 65102

"Inertia-friction welding can retain the rapidly-solidified, metastable microstructure across the weld interface and inhibit defect formation."

ABSTRACT

The inertia-friction welding of rapidly-solidified, powder metallurgy (RS/PM) Al-Fe-Ce alloys has been investigated from a metallurgical perspective. Similar alloy welds in Al-9 wt% Fe-4 wt% Ce and Al-9 wt% Fe-7 wt% Ce, and dissimilar alloy welds between these RS/PM alloys and ingot metallurgy alloy 2024-T351 were generated and characterized using light and electron microscopy, mechanical testing and fractographic analysis. Results showed the weld axial force to significantly influence weld integrity. Similar alloy welds produced with low axial force were characterized by voids and lack of bonding at the outer periphery and a heat and deformation zone comprised of coarsened intermetallics. The hardness, tensile strength and ductility across this zone were correspondingly degraded with respect to the unaffected base metal. The application of higher axial force during welding promoted the increased expulsion of heat and deformation-affected metal from the weld interface, thereby minimizing or eliminating the presence of a dispersoid-coarsened region and inhibiting defect formation. Welds produced in RS/PM alloys at the highest axial force exhibited minimal hardness losses across the interface and optimum weld strengths.

Deformation during dissimilar alloy welding occurred nearly entirely in

the 2024-T351. Although weld interface defects were not observed, occasional intergranular cracks were apparent in the 2024-T351 at the outer weld periphery. Weld strengths were approximately 60 to 70 percent of the Al-Fe-Ce base alloys.

INERTIA-FRICTION WELDING OF RAPIDLY SOLIDIFIED POWDER METALLURGY ALUMINUM

W. A. Baeslack III* and K. S. Hagey**

*Department of Welding Engineering
The Ohio State University
Columbus, Ohio 43210

**Westinghouse Electric Company
Jefferson City, Missouri 65102

INTRODUCTION

Conventional elevated-temperature aluminum alloys derive their strength principally from precipitation hardening. Although moderate to high strength levels can be maintained in certain 2XXX-series alloys up to approximately 150°C (300°F), service at higher temperatures promotes rapid precipitate coarsening and a corresponding decrease in strength.

Recent advances in rapid-solidification/powder metallurgy (RS/PM) technology have led to the development of a new generation of high-strength aluminum alloys designed specifically for application at temperatures up to 350°C (660°F) (Ref. 1). These unique alloys are hypereutectic aluminum-iron compositions with ternary additions of cerium, molybdenum, nickel or cobalt. Through rapid solidification, the formation of coarse, primary intermetallics is suppressed and solidification instead occurs to a supersaturated alpha phase or microeutectic. Subsequent consolidation and thermomechanical processing produces a microstructure comprised of extremely fine dispersoids in a matrix of submicron alpha grains. Similar to hardening precipitates in conventional heat-treatable aluminum alloys, these fine dispersoids interact with dislocations to provide high strength. In contrast to the precipitates, however, the dispersoids exhibit a high thermodynamic stability which results in a retention of high strength to elevated temperatures. The superior elevated-

temperature strength of a recent generation Al-8.4Fe-7.0Ce alloy is compared with strengths of the ingot metallurgy (IM) alloys 2024-T351 and 2219-T851 in Figure 1 (Refs. 2 and 3).

The utilization of "dispersoid" type RS/PM aluminum alloys in structural applications will require the development of effective and economical joining methods. Fusion welding techniques, which are widely used for the joining of IM aluminum alloys, have been applied with limited success to the RS/PM Al-Fe-Ce alloys (Ref. 4). The primary difficulty has been the formation of gross fusion zone porosity due to an inherently high base metal hydrogen content. This hydrogen originates from non-inert powder atomization which promotes oxide formation on powder surfaces and the subsequent reaction of this oxide with humid air to form deleterious hydroxides. Since vacuum degassing and consolidation temperatures are below those required for complete decomposition of the hydroxides, relatively high total hydrogen levels are retained in the final product (typically 1 to 10 ml/100gms Al). Hydroxide decomposition occurs in the molten weld pool, however, promoting hydrogen evolution and the formation of porosity on solidification. Recent studies of Al-Fe-Mo alloys have shown that completely inert atomization and consolidation significantly reduces the hydrogen content and eliminates hydrogen-induced porosity during fusion welding (Ref. 5). However, such processing is more complex and costly than air or flue-gas atomization and has not been implemented by the producers of Al-Fe-Ce alloys.

Solid-state welding provides an important alternative to fusion welding for materials in which melting and solidification must be avoided. Inertia-friction welding is a solid-state welding process which combines frictional heating generated at faying surfaces and a high axial pressure to produce a metallurgical bond (Ref. 6). The absence of melting at the interface during

inertia-friction welding minimizes or eliminates the formation of solidification-related discontinuities such as porosity or cracking. In addition, the expulsion of surface contaminants and severely heat and deformation-affected metal at faying surfaces during the final forging and upset stage of the process promotes final bonding between fresh subsurface materials. These two inherent process characteristics have established inertia-friction welding as an important technique for joining non-fusion weldable materials, of which RS/PM Al-Fe-Ce alloys are representative.

OBJECTIVES

In order to determine the potential of inertia-friction welding as a viable joining method for RS/PM Al-Fe-Ce aluminum alloys, the following four objectives were set forth:

1. determine the feasibility of producing sound inertia-friction welds between Al-Fe-Ce alloys and between Al-Fe-Ce alloys and IM 2024-T351,
2. determine the effect of axial force on weld characteristics and quality,
3. examine the metallurgical response of the alloys to the thermal-mechanical conditions experienced during welding,
4. develop correlations between the inertia-friction weld microstructure, tensile properties and fracture characteristics.

EXPERIMENTAL METHODS

Materials

Chemical compositions of the RS/PM alloys evaluated in this study were Al-8.6 wt% Fe-6.9 wt% Ce and Al-8.6 wt% Fe-3.8 wt% Ce (designated Al-9Fe-7Ce and Al-9Fe-4Ce, respectively). Hydrogen contents of both alloys were in the range of 2-3 ml/100 gm Al. The nominal chemical composition of the commercial IM 2024-T351 extruded rod used in dissimilar alloy welds was Al-4.5 wt% Cu-1.5

wt% Mg-0.6 wt% Mn.

Powder production was performed using flue-gas atomization in order to reduce cerium losses due to oxidation. Irregular-shaped powder particles, which are characteristic of both flue-gas and air atomization, ranged from approximately 5 to 40 microns in diameter (Figure 2). As shown in Figure 2b, metallographic examination of powder particle cross sections showed a distinct relationship between powder size and solidification structure. The finest, most rapidly-solidified particles exhibited an optically featureless microstructure which is designated in the literature as "Zone A" (Refs. 7-9). In contrast, the coarser, more slowly cooled particles were characterized by a darker, distinctly cellular-dendritic microstructure which is designated as "Zone B".

Powder processing followed the standard ALCOA/Frankfort Arsenal sequence which is schematically illustrated in Figure 3 (Ref. 10). After screening to reduce particle size differences, the powder was cold compacted to a density of approximately 75%. Subsequent hot vacuum degassing of the compact removed physically absorbed gases and promoted partial decomposition of aluminum hydroxides. Final hot pressing and extrusion to a 10.2 mm. (4 in.) by 1.9 mm. (0.75 in.) cross section provided the high degree of powder particle deformation and breakup required to achieve optimum mechanical properties.

Light micrographs of the Al-9Fe-4Ce and Al-9Fe-7Ce base alloy microstructures are shown in Figures 4A and 4B, respectively. Both structures exhibited good homogeneity and a light texture parallel to the extrusion direction. Also evident in Figure 4 are occasional, light-etching spheres. These regions were identified as fine powder particles which retained their shape during compaction and extrusion due to the extremely high hardness of their Zone A microstructure. Although the dispersoid structures were too fine for

resolution using light microscopy, scanning-electron microscopy (SEM) and transmission-electron microscopy (TEM) bright-field analysis revealed a variety of needle-shaped intermetallics in a matrix of submicron alpha aluminum grains (Figure 5). TEM diffraction and X-ray phase identification studies of these alloys have identified several different intermetallics and their metastable precursor phases, including Al_3Fe , Al_6Fe , $\text{Al}_{10}\text{Fe}_2\text{Ce}$, $\text{Al}_8\text{Fe}_4\text{Ce}$ and AlFeCe-2 (Refs. 11-13).

Cylindrical specimens for inertia-friction welding 12.5 mm. (0.5 in.) in diameter and 3.2 mm. (1.25 in.) in length were machined both longitudinal (L) and transverse (T) to the extrusion direction. The faying surfaces of each specimen were mechanically ground and cleaned with acetone prior to welding.

Inertia-Friction Welding

Inertia-friction welds were produced on a 53,280 N (12,000 lb.) MTI Model 90B inertia-friction welding system initially using welding parameters previously established for 2024-T6 aluminum. Through visual examination of the extruded metal flash and measurement of axial displacement, welding parameters including the moment of inertia, rotational speed and axial force were optimized for both similar and dissimilar alloy weldments (Table I). In addition to similar alloy welds produced at the initially optimized parameters (designated "medium" axial force), selected welds were also produced at lower and higher axial forces.

Weld Characterization

Representative welds were sectioned axially, mounted in epoxy and mechanically polished. After defect analysis of the as-polished surface using light microscopy, microstructure characteristics were revealed by etching with Keller's reagent and examined using light and scanning-electron microscopy.

In addition, thin foils were produced from the unaffected base metals and weld interface regions and examined using TEM.

Diamond pyramid microhardness traverses were performed across the weld interface at different distances from the axial centerline using a load of 500 grams. Progressive bend and tensile tests were conducted to determine the strength and ductility of the inertia-friction welds. Bend test specimens were produced by removing the weld flash and longitudinally sectioning the weldment into two pieces. Multiple progressive bend tests were conducted for each alloy/weld parameter combination such that both the weld center and outer periphery were placed in tension. Tensile specimens were machined from the center region of welded specimens (4 mm. [0.16 in.] gage dia., 16.5 mm [0.65 in.] gage length) and tested at an extension rate of 0.0042 mm/sec. (0.01 in/min.).

Fracture analysis of tensile specimens was accomplished using SEM and energy-dispersive X-ray analysis (EDS).

RESULTS

Visual Examination

Visual analysis of the Al-Fe-Ce similar alloy welds found good symmetry and continuity of flash around the weld circumference, with the volume of flash increasing significantly with increased axial force (Figure 6). The Al-Fe-Ce/2024-T351 dissimilar alloy welds exhibited negligible flash in the Al-Fe-Ce and a discontinuous, "torn" flash in the 2024-T351 (Figure 7).

Average axial displacements for different alloy/weld parameter combinations are shown in Table 2. As expected, an increase in axial force while maintaining other parameters constant promoted increased axial displacement. Also evident from Table 2 are the consistently greater axial displacements of the Al-9Fe-4Ce versus the Al-9Fe-7Ce similar alloy welds. This difference can

be attributed to the greater compressive yield strength of the higher Ce alloy at elevated temperatures. Welds produced in specimens oriented transverse to the extrusion direction exhibited slightly greater displacements than those produced in specimens oriented parallel to this direction. This effect may also result from differences in the compressive yield strengths for different orientations.

Macroscopic Characterization

Macroscopic characterization of axially-sectioned similar alloy weldments in the as-polished condition revealed two types of defects. In low and medium axial force welds, the nonuniform deformation and extrusion of softened metal out of the original interface region promoted the formation of voids near the outer weld periphery (Figures 6). In addition to these gross defects, similar alloy welds produced at all axial forces exhibited fine, lack-of-bonding discontinuities oriented parallel to the weld interface* (Figure 8). The number and size of these linear discontinuities, which in several instances appeared to be associated with dispersed oxides, decreased with increased axial force and were only occasionally observed at the outer periphery of welds produced at the highest axial force. Despite the high base metal hydrogen content, no evidence of hydrogen-induced blistering was observed in the welds.

As shown in Figure 7, deformation of the 2024-T351 was quite extensive in the dissimilar alloy welds due to a comparatively low strength at the high temperatures experienced in the vicinity of the weld interface. Although examination of the as-polished weldments showed complete bonding at the Al-Fe-

*Similar alloy welds did not exhibit a distinct weld "interface", but rather a continuous "heat and deformation" zone (HDZ). For discussion purposes, the term weld "interface" refers to the symmetric center of the HDZ.

Ce alloy/2024-T351 interface, occasional intergranular cracks were observed in the 2024-T351 HDZ at the weld outer periphery (Figure 8C).

Heavy etching of the similar alloy welds clearly revealed macroscopic heat and deformation zones (HDZ's). Welds produced at low axial force exhibited wide HDZ's of nearly uniform width. Increased axial force enhanced the extrusion of heat and deformation-affected metal out of the weld interface as flash, resulting in a thinner, more hourglass shaped HDZ. This general effect of axial force on inertia-friction weld HDZ geometry is schematically illustrated in Figure 9. Dissimilar alloy welds were characterized by an extensive macroscopic HDZ of nearly uniform width in the 2024-T351 and a negligible HDZ in the Al-Fe-Ce.

Microstructure Characteristics

Microstructure traverses from the unaffected base metal to the weld interface are shown in Figure 10 near the center of welds produced in Al-9Fe-4Ce at low and high axial forces. The radially outward flow of metal which is characteristic of inertia-friction welding is clearly evident in the far HDZ region, with the microstructure texture continuously changing from parallel to perpendicular to the original base alloy extrusion direction. Nearer the weld interface, higher temperatures and deformation levels disrupted the textured base metal microstructure. As shown, the width of this dark-etching region decreased with increased axial force. At the weld interface, temperature and deformation effects were most significant, as evidenced by the formation of a distinct, light-etching band. The examination of this structure using TEM (Figure 11) indicated appreciable coarsening of the dispersoid and alpha grain structures as compared to the unaffected base metal (Figure 5). The width of this region paralleled that of the dark-etching transition structure, decreasing with increased axial force. As shown in Figures 6C and 10B, the

light-etching region was essentially absent near the center of Al-Fe-Ce similar alloy welds produced at the highest axial force. Although not illustrated, microstructural characteristics of the Al-9Fe-7Ce welds paralleled those of the Al-9Fe-4Ce.

A microstructure traverse across an Al-9Fe-4Ce/2024-T351 dissimilar alloy weld is illustrated in Figure 12. Deformation of the Al-Fe-Ce alloy was apparent only as a slight change in the texture orientation directly adjacent to the weld interface. In contrast, the coarse, elongated alpha grains exhibited by the 2024-T351 base metal experienced severe deformation radially outward parallel to the weld interface, becoming elongated near the interface. Examination at increased magnification indicated the presence of a fine subgrain structure within the elongated alpha grains and precipitation or coarsening of $MgCuAl_2$ at grain and subgrain boundaries (Figure 13). Directly adjacent to the weld interface, high temperatures and deformation promoted the formation of an extremely fine microstructure comprised of dynamically recrystallized alpha grains.

As mentioned earlier, inertia-friction welding is a solid-state process in which melting at the interface generally does not occur. In the present study, however, evidence of melting was observed near the outer periphery of low axial force similar alloy welds where surface velocities and temperatures were greatest. In these welds, distinct "streaks" or "swirls" of light-etching Zone A solidification product were observed at the interface (Figure 8).

Microhardness Testing

Microhardness traverses across the Al-Fe-Ce similar alloy welds corresponded well with the observed microstructure characteristics (Figure 10C). Although hardness decreases were not apparent in the far HDZ and minimal in

the dark-etching HDZ structure, a significant decrease in hardness was observed in the wide, light-etching structure exhibited along the weld interface of low axial force welds. Similar microstructures near the outer periphery of medium axial force welds showed comparable hardness traverses. As shown in Figure 10C, the elimination of this coarsened structure along most of the weld interface in high axial force welds minimized hardness losses across the weld.

Consistent with microstructure analysis, the hardness of the Al-Fe-Ce in dissimilar alloy welds appeared essentially unaffected by the weld thermal/mechanical cycle (Figure 11C). Hardness in the 2024-T351 was observed to increase slightly in the severely deformed alpha grains but decrease in the fine microstructure directly adjacent to the weld interface.

Bend and Tensile Properties

Guided bend testing of the similar and dissimilar alloy welds generally found bend ductilities to be below 6%*, with macroscopically flat fractures occurring nearly exclusively along the interface region. Welds produced in Al-9Fe-4Ce with a high axial force were the exception, exhibiting ductilities of 10 to 12 percent and a more shear-appearing fracture.

The greatest differences in weld interface microstructure characteristics were exhibited between the centers of the low and high axial force welds. Evaluating the influence of interface region microstructure, without an influence of outer periphery defects, required sectioning of tensile specimens from this center region. Tensile properties obtained from these specimens for the similar alloy inertia-friction welds are shown in Table 2. Increased axial force was found to promote significant increases in tensile strength,

* The minimum strain allowed by test apparatus for 6.4 mm (0.25 in) thick specimen was 6%.

exceeding 90% of the base metal strength for high axial force welds. Higher weld strengths in the Al-9Fe-7Ce relative to the Al-9Fe-4Ce alloy reflected differences in base metal hardness and strength. Tensile strength of the dissimilar alloy weld tensile specimens averaged between 60 and 80% of the Al-Fe-Ce base alloy, with welds produced between transverse-oriented Al-Fe-Ce alloys exhibiting lower strength levels.

Tensile ductilities of similar alloy weld tensile specimens also increased with greater axial force. This improvement resulted from the increased interface region strength and more uniform elongation along the specimen gage section (i.e., less strain localization in the lower strength weld interface region). Elongation values were still well below the 10-12% observed in the Al-Fe-Ce base metals.

It is important to recognize that these tensile properties are optimum for the respective alloy/welding parameter combinations in that they do not reflect the influence of lack of bonding defects at the outer periphery of similar alloy welds.

Fracture Characteristics

Fracture locations were identified by axially sectioning and metallographically preparing one-half of the failed tensile or bend specimen. Both bend and tensile specimen failures were associated primarily with the weld interface region, with the only exceptions being similar alloy welds produced at high axial force. In these welds, the absence of defects and minimal loss of strength due to microstructural coarsening promoted a shear-like fracture across the weld interface, HNZ and unaffected base metal.

Fractographic analysis of the bend and tensile specimen fracture surfaces revealed important information pertaining to both fracture behavior and the formation of weld defects. Figures 14 and 15 illustrate the bend and

tensile specimen fracture surfaces, respectively, for Al-9Fe-4Ce welds produced at low axial force. Both fracture surfaces exhibited a distinct spiral appearance emanating from the center of the bar. As schematically illustrated in Figure 16, this fracture pattern reflects the effects of combined torsional and axial forging forces on metal flow experienced at the interface during inertia-friction welding. The bend specimen fracture surface shown in Figure 14A shows a varying fracture topography comprised of macroscopically flat and highly-irregular regions, with the flat regions located primarily at the outer periphery. Through the analysis of matching fracture surface pairs, the "cliffs" shown in Figure 14B were determined to bound the large, outer periphery voids observed in transverse-mounted sections. The voids appear to be associated with the "peeling back" of layers of metal at the weld interface (arrow in Fig. 14B), which suggests very nonuniform plastic deformation in this region during the welding process. Analysis of the void surfaces at high magnification (Fig. 14C) showed a dimpled appearance indicating that these regions were not original unbonded interfaces, but rather interface regions which had fractured and separated during welding. Deformation and fracture appeared to be more ductile toward the center of the bend specimen fracture surface and across the entire tensile specimen fracture surface (Figure 15). At high magnification, fracture in these regions appeared associated with microvoid formation around the fine dispersoids and ductile fracture of the soft alpha aluminum matrix.

The bend and tensile fracture surfaces of similar alloy welds produced at high axial force exhibited a shear mode of failure (Figure 7). Although fracture likely initiated at the weld interface, crack propagation continued into the HDZ and unaffected base metal regions. Analysis of the interface surface region (arrow in Fig. 17A) showed a spiral macroscopic fracture

pattern and a dimpled fracture at high magnification. Although the microstructure in this weld region exhibited an appreciably finer dispersoid and alpha grain size than the low axial force welds, differences in microvoid size and distribution on the fracture surfaces were not apparent.

Fracture of the tensile and bend specimens in dissimilar alloy welds occurred along the weld interface (Figure 8). Examination at high magnification found a fracture surface similar to that observed at the center of the Al-Fe-Ce similar alloy welds, suggesting fracture principally through the Al-Fe-Ce directly adjacent to the weld interface. EDAX compositional analysis of the Al-Fe-Ce and 2024-T351 fracture surfaces, however, revealed the presence of elements from both alloys. This indicated fracture through a discreet region of alloy mechanical mixing at the weld interface.

DISCUSSION

The inertia-friction welding process exhibits several inherent characteristics which make it extremely suitable for the welding of RS/PM Al-Fe-Ce alloys and the dissimilar alloy welding of these alloys to conventional aluminum alloys. These characteristics include: (1) an absence of melting at the weld interface, (2) rapid heating and cooling rates and (3) the expulsion of severely heat and deformation-affected metal during the final forging and upset stage of the process. In order to take full advantage of these process characteristics, principal welding parameters (i.e., rotational velocity, inertia mass and axial force) must be carefully controlled. In the present work, this requirement for welding parameter optimization was found to be critical in preventing weld defect formation and optimizing weld microstructure characteristics and mechanical properties.

Defect Formation and Prevention

Macroscopic void formation at the weld outer periphery represented a significant defect in similar alloy welds produced at low and medium axial force. During the inertia-friction welding process of similar alloys, mechanical mixing occurs between thin layers of metal on each side of the weld interface. Under ideal welding conditions, this local mixing and deformation is associated with a stable plastic condition across the entire interface region. In the Al-Fe-Ce alloy welds, local plastic instabilities existed which promoted nonuniform deformation of metal in the interface region, fracture of the interface region during welding and the separation of these interfaces. This "fracture and separation" mechanism for void formation, versus a lack of bonding between original metal interfaces, was supported by SEM analysis of matching, opposite cavity surfaces which showed distinct evidence of prior plastic deformation and fracture. The tendency for such plastic instabilities in the Al-Fe-Ce alloys was likely promoted by a base metal microstructure comprised of a large proportion of high strength intermetallics in a matrix of soft alpha aluminum. This microstructure exhibited higher strength versus conventional single-phase aluminum alloys at the high weld interface temperatures but poorer hot ductility, which contributed to plastic instability and void formation. The influence of increased axial force in promoting more stable plastic deformation at the interface and thereby reducing or eliminating void formation was not apparent in this investigation. It is suggested, rather, that the greater axial displacement and extrusion of heat and deformation-affected metal out of the interface region promoted the filling and/or closure of voids or cavities which existed prior to the final forging and upsetting.

The fine, linear lack-of-bonding defects present along the weld

interface represented a more common but less serious defect in similar alloy welds. The occasional association of these defects with oxide particles indicated that their origin may be associated with original powder processing and/or surface preparation prior to welding. The reduction and elimination of these defects at high axial force resulted in part from the expulsion of these surface oxides from the interface.

As discussed earlier, a principal difficulty with the fusion welding of Al-Fe-Ce alloys is the evolution of hydrogen in the molten weld pool and the subsequent formation of porosity on solidification. Although somewhat controversial, the literature generally agrees that melting does not occur at the interface during inertia-friction welding (Ref. 6). These conclusions have been based on metallographic analysis, interface temperature measurements and calculations, and the analysis of the weld cycle torque curve which would indicate a discontinuity if appreciable liquid were present (Refs. 13 and 14). In addition, it would be anticipated that any solid present at near-solidus interface temperatures would be so low in strength that it would be extruded out as flash prior to the onset of melting. Although extensive melting was not observed in the Al-Fe-Ce welds, occasional streaks of Zone A at the weld interface outer periphery (where temperatures are highest) did indicate localized liquation. An absence of porosity in these regions resulted from the effect of high axial force on either inhibiting pore formation or promoting the closure of pores during final forging stage of the process.

As shown above, dissimilar alloy weldments were characterized by extensive macroscopic deformation in the 2024-T351 and minimal deformation in the Al-Fe-Ce. On a microscopic level, however, the mechanical mixing of the two alloys was evident at the weld interface. In contrast to the similar alloy welds, void formation and evidence of fine lack-of-bonding defects were not

apparent at the weld interface of dissimilar alloy welds. Complete bonding at this interface was apparently promoted by the low strength of the 2024-T351 at welding temperatures and the associated extensive deformation. Outer periphery defects were observed in the 2024-T351 HDZ in the form of fine grain boundary cracks. The origin of these cracks appeared to be eutectic liquation of second phase particles due to the high temperatures experienced in this region of the weld. The influence of these defects on bend and tensile fracture behavior appeared to be minimal.

Structure/Property/Fracture Relationships

In addition to the prevention of weld defects, the production of high joint efficiency welds in Al-Fe-Ce requires retention of the fine base metal dispersoid and alpha grain structure across the weld interface. Such microstructure retention is promoted in inertia-friction welding by the high rate of energy input and short weld cycle duration which provide extremely high weld heating and cooling rates. Although actual thermal cycle data is not available for welds in aluminum alloys, experimental and calculated thermal cycles for inertia-friction welds in steel have indicated heating rates on the order of 10^4 °C/s, with the rates being greatest at the midradius (Ref. 6). The higher thermal conductivity of aluminum would reduce these rates somewhat, however, heating rates of at least 10^3 °C/s would be expected. These high heating rates and short time period at peak temperatures would tend to reduce dispersoid and alpha grain coarsening at the weld interface region and adjacent HDZ, and minimize hardness and strength losses in these regions. Although not as great as the heating rates, cooling rates from peak temperature would also be rapid due to the heat sinking effects, thereby reducing dispersoid and grain coarsening in the completed inertia-friction weld. Despite these rapid inertia-friction weld thermal cycles, the high temperatures

experienced at the weld interface promoted appreciable dispersoid coarsening. In the low and medium axial force welds, this coarsened HDZ was largely retained at the weld interface. However, increased axial force promoted the expulsion of thermally softened material out of the interface region as flash, resulting in a weld between microstructures minimally affected by heat and deformation.

Mechanical property tests, including hardness and transverse bend and tensile tests, were effective in demonstrating the importance of minimizing microstructure coarsening at the weld interface in maximizing properties. Structural coarsening at the weld interface promoted reduced hardness and strength versus the surrounding HDZ and base metal which led to its preferential fracture. The near elimination of a structurally coarsened region with high axial force served to maximize weld efficiency.

Inertia-friction welding has been widely used for the joining of dissimilar alloys (Refs. 15-18). Although the dissimilar alloys joined in the present study were both aluminum base, their microstructures and more importantly their elevated-temperature properties differed appreciably. These significant property differences were reflected in the extensive deformation of the 2024-T351 versus the minimal deformation in the Al-Fe-Ce. Despite the formation of an extensive heat and deformation affected region in the 2024-T351, and no subsequent heat treatment, it is significant to note that room temperature hardness and strength of this region exceeded that of the Al-Fe-Ce. Fracture at stresses below the ultimate tensile strength of the Al-Fe-Ce may reflect slight, unobserved coarsening directly adjacent to the interface, or a weakness in the discreet region of mechanical mixing between the alloys.

CONCLUSIONS

1. Inertia-friction welding has been demonstrated to be an effective process for joining RS/PM Al-Fe-Ce alloys generally considered unweldable by fusion welding techniques.
2. Weld axial force significantly influenced joint integrity, with increased force reducing or eliminating the dispersoid and grain-coarsened structure at the weld interface region. In addition, increased force inhibited the formation of voids at the weld outer periphery and fine, linear discontinuities across the weld interface region.
3. Retention of the RS/PM microstructure and the elimination of defects in the weld interface region resulted in minimal losses of hardness and strength across the weld region.
4. Dissimilar alloy inertia-friction welds between IM 2024-T351 and the Al-Fe-Ce alloys exhibited room-temperature strength levels 60 to 70% of the Al-Fe-Ce base metal. Fracture was associated with a discrete region of alloy mechanical mixing at the weld interface.

ACKNOWLEDGMENTS

The authors are indebted to Dr. G. J. Hildeman of Alcoa Co. for providing the Al-Fe-Ce alloys, Mr. D. E. Kuruzar of MTI, Inc., for technical assistance in the inertia-friction welding and Mr. S. Krishnaswamy of OSU for his metallographic efforts. We would also like to thank Professor C. A. Albright of The Ohio State University and Dr. J. C. Lippold of Edison Welding Institute for their helpful comments. Finally, appreciation is expressed to the Army Research Office for its support of this work under Contract No. DAAG29-84-K-0176.

REFERENCES

1. Quist, W. E. and Lewis, R. E., 1986. "The need for rapidly-solidified powder metallurgy aluminum alloys for aerospace applications", Rapidly Solidified Powder Aluminum Alloys, ASTM STP 890, American Society for Testing Materials, Philadelphia, PA, pp. 7-38.
2. Langenbeck, S. L., Griffith, W. M., Hildeman, G. J. and Simon, J. W., 1986. "Development of dispersion strengthened aluminum alloys", Rapidly Solidified Powder Aluminum Alloys, ASTM STP 890, American Society for Testing Materials, Philadelphia, PA, pp. 410-422.
3. Properties and Selection: Nonferrous Alloys and Pure Metals, 1979. ASM Handbook, Volume 2, Ninth Edition, American Society for Metals, Metals Park, OH, pp. 72-88.
4. Unpublished research performed at The Ohio State University, Columbus, OH, 1983.
5. Baeslack, W. A. III, and Krishnaswamy, S., 1987. "Electron beam weldability of a rapidly-solidified powder metallurgy aluminum alloy", International Trends in Welding Research, American Society for Metals, Metals Park, OH.
6. Wang, K. K., 1975. "Friction welding", Welding Research Council Bulletin #204, Welding Research Council, New York, NY.
7. Jones, H., 1969. "Observations of a structural transition in Al alloys hardened by rapid solidification", Materials Science and Engineering, 5:1-18.
8. Garrett, R. K., Jr., and Sanders, T. H., Jr., 1983. "The formation of coarse intermetallics in rapidly solidified Al-Co alloys", Materials Science and Engineering, 60: 269-274.
9. Jacobs, M. H., Dogget, A. G. and Stowell, M. J., 1974. "The microstructure of Al-8wt% Fe-based alloys prepared by rapid quenching from the liquid state", Journal of Materials Science, 9: 1631-1643.
10. Cebulak, W. A., 1977. "Program to develop high strength aluminum powder metallurgy mill products - phase IVB scale-up to 1545 Kg Billet", Final Report FA-TR-76067, Frankfort Arsenal, Philadelphia, PA.
11. Angers, L. M., 1985. "Particle coarsening in rapidly solidified Al-Fe-Ce alloys", Ph.D. thesis, Northwestern University.
12. Chy, M. G., Rioja, R. J., Hildeman, G. J., and Denzer, D. K., 1985. "Microstructural evolution during solidification of Al-Fe-Ce powders", Proceedings of the 43rd Annual Meeting of the Electron Microscopy Society of America, p. 32.
13. Cheng, C. J., 1963. "Transient Temperature During Friction Welding of Two Similar Materials in Tubular Form", Welding Journal, 42(5): 233s to 240s.

14. Wang, K. K. and Nagappan, P., 1970. "Transient Temperature Distribution in Inertia Welding of Steels", Welding Journal, 49(9): 419s-426s.
15. Hazlett, T. H. 1962. Properties of friction welds between dissimilar metals. Welding Journal 41(10):448-s to 450-s.
16. Nicholas, E. D., Jessop, T., and Dinsdale, W. O. 1978. Friction welding dissimilar metals, Advances in welding processes proceedings, 4th international conference, Harrogate, York, May 1978, The Welding Institute, paper 49, pp. 23-26.
17. Jessop, T. J., and Dinsdale, W. O. 1976. Mechanical testing of dissimilar metal friction welds. Welding Research International 6(2): 1-22.
18. Bell, R. A., Lippold, J. C. and Adolphson, D. R., 1984. "An Evaluation of Copper-Stainless Steel Inertia-Friction Welds", Welding Journal, 63(11): 325s - 331s.

LIST OF TABLES

Table 1. Inertia-Friction Welding Parameters

Table 2. Inertia-Friction Weld Axial Displacement and Tensile Properties

Table 1. Inertia-Friction Welding Parameters

<u>Similar Alloy</u> <u>Weldments</u>	<u>Dissimilar Alloy</u> <u>Weldments</u>
Moment of Inertia: $4.6 \times 10^{-3} \text{ kg-m}^2$ (0.108 $\text{lb}_m\text{-ft}^2$)	$8.3 \times 10^{-3} \text{ kg-m}^2$ (0.198 $\text{lb}_m\text{-ft}^2$)
Rotational Speed: 1,206 radians/s (11,660 rpm)	1144 radians/s (11,000 rpm)
Angular Velocity: 7.6m/s (1,527 fpm)	7.2m/s (1,441 fpm)
Axial Thrust Load: 4.4, 6.5, 8.7 kN (980; 1,470; 1,960 lb_f)	12.0kN (2,695 lb_f)

Table 2. Inertia-Friction Weld Axial Displacements and Tensile Properties

Material Combination	Axial Force*	Axial Displacement mm (in)	Tensile Strength MPa (ksi)	Joint Efficiency** %	% Elong.	Fracture Location***
Al-9-4 L/Al-9-4 L	Low	2.5 (0.10)	234 (34)	56	1.9	IR
Al-9-4 L/Al-9-4 L	Med	5.8 (0.23)	262 (38)	62	2.9	IR
Al-9-4 L/Al-9-4 L	High	9.6 (0.38)	386 (56)	92	3.0	IR/HDZ
Al-9-4 T/Al-9-4 T	Med	5.8 (0.23)	289 (42)	69	2.4	IR
Al-9-7 L/Al-9-7 L	Low	1.8 (0.07)	262 (38)	56	1.9	IR
Al-9-7 L/Al-9-7 L	Med	4.6 (0.18)	386 (56)	82	2.7	IR
Al-9-7 L/Al-9-7 L	High	8.9 (0.35)	427 (62)	91	3.0	IR/HDZ
Al-9-7 T/Al-9-7 T	Med	5.3 (0.21)	289 (42)	62	2.3	IR
Al-9-4 L/2024	-	5.1 (0.20)	331 (48)	79	1.8	IR
Al-9-4 T/2024	-	5.1 (0.20)	310 (45)	65	1.7	IR
Al-9-7 L/2024	-	4.8 (0.19)	338 (49)	72	2.0	IR
Al-9-7 T/2024	-	5.3 (0.21)	290 (42)	61	2.0	IR

*Low, Medium and High Pressures were 4.4, 6.5 and 8.7 kN (980, 1470, 1960 lbf), respectively

**The weld center for Al-9Fe-4Ce, Al-9Fe-7Ce and 2024-T351 base metal tensile strengths of 420, 469 and 469MPa (61, 68 and 68 ksi), respectively).

***IR - Interface Region, HDZ - Heat and Deformation Zone

LIST OF FIGURES

- Figure 1 - Tensile strength versus test temperature for RS/PM Al-8.4Fe-7.0Ce and IM 2024-T351 and 2219-T851. Note that the Al-8.4Fe-7.0Ce alloy was tested after 1000 hours at 150 and 232°C (300 and 450°F) and 100 hours at 315°C (600°F) (Refs. 2 and 3).
- Figure 2 - SEM (A) and light (B) micrographs of Al-9Fe-4Ce flue-gas atomized powder. Arrows indicate featureless Zone A regions.
- Figure 3 - Processing sequence for Al-Fe-Ce powder.
- Figure 4 - Light micrographs of (A) Al-9Fe-4Ce and (B) Al-9Fe-7Ce base metal microstructures. Large arrows indicate extrusion direction, small arrows indicate undeformed powder particles.
- Figure 5 - TEM bright-field micrographs of Al-9Fe-4Ce base metal microstructure. Arrows indicate fine intermetallics.
- Figure 6 - Inertia-friction welds in Al-9Fe-4Ce: (A) as welded specimens produced at low, medium and high axial force (top-to-bottom), (B, C) axial sections of welds produced at low and high axial forces, respectively. Arrows in B and C indicate bond lines.
- Figure 7 - Inertia-friction weld between Al-9Fe-4Ce (left side) and 2024-T351 (right side): (A) as-welded specimen, (B) axial section, arrow indicates weld bond line.
- Figure 8 - Defects in (A,B) Al-9Fe-7Ce low axial force weld and (C) Al-9Fe-4Ce/2024-T351 dissimilar alloy weld: (A) coarse, linear defect near outer periphery (etched); (B) fine, linear defect near weld centerline (unetched); (C) intergranular cracks adjacent to weld interface in 2024-T351. Small arrows indicate defects, large arrow in (A) indicates apparent Zone A solidification product.
- Figure 9 - Schematic illustrating the general effect of axial force on heat and deformation zone geometry for similar alloy inertia-friction weld.
- Figure 10 - Microstructures (A, B) and diamond pyramid hardness traverse (C) near center of inertia-friction welds in Al-9Fe-4Ce produced at (A) low and (B) high axial forces. Arrows indicate weld interface.
- Figure 11 - TEM bright-field micrographs showing coarsened dispersoid structures at interface of low axial force Al-9Fe-4Ce inertia-friction weld.
- Figure 12 - Microstructure and diamond pyramid hardness traverse near center of inertia-friction weld produced between Al-9Fe-4Ce and 2024-T351. Arrow indicates weld interface.

Figure 13 - Light micrograph of weld interface in Al-9Fe-4Ce dissimilar alloy inertia-friction weld. Large arrow indicates weld interface, small arrows indicate intermetallics at alpha boundaries in 2024-T351.

Figure 14 - SEM fractographs of bend tested Al-9Fe-4Ce inertia-friction weld produced at low axial force: (A) macroscopic fracture surface, (B) flat fracture near outer periphery and "cliff" (arrow) bounding void, (C) surface of void at increased magnification.

Figure 15 - SEM fractographs of tensile tested Al-9Fe-4Ce inertia-friction weld produced at low axial force: (A) macroscopic fracture surface, (B) spiral pattern indicating metal flow during welding, (C) dimpled fracture surface at increased magnification.

Figure 16 - Schematic illustration of metal flow during inertia-friction welding (Ref. 6).

Figure 17 - SEM fractographs of tensile tested Al-9Fe-4Ce inertia-friction weld produced at high axial force: (A) macroscopic fracture surface, (B, C) interface fracture surface at increased magnification.

Figure 18 - SEM fractographs of tensile tested Al-9Fe-4Ce/2024-T351 dissimilar alloy inertia-friction weld (2024-T351 side): (A) macroscopic fracture surface, (B) spiral pattern indicating metal flow during welding, (C) dimpled fracture surface revealed at increased magnification.

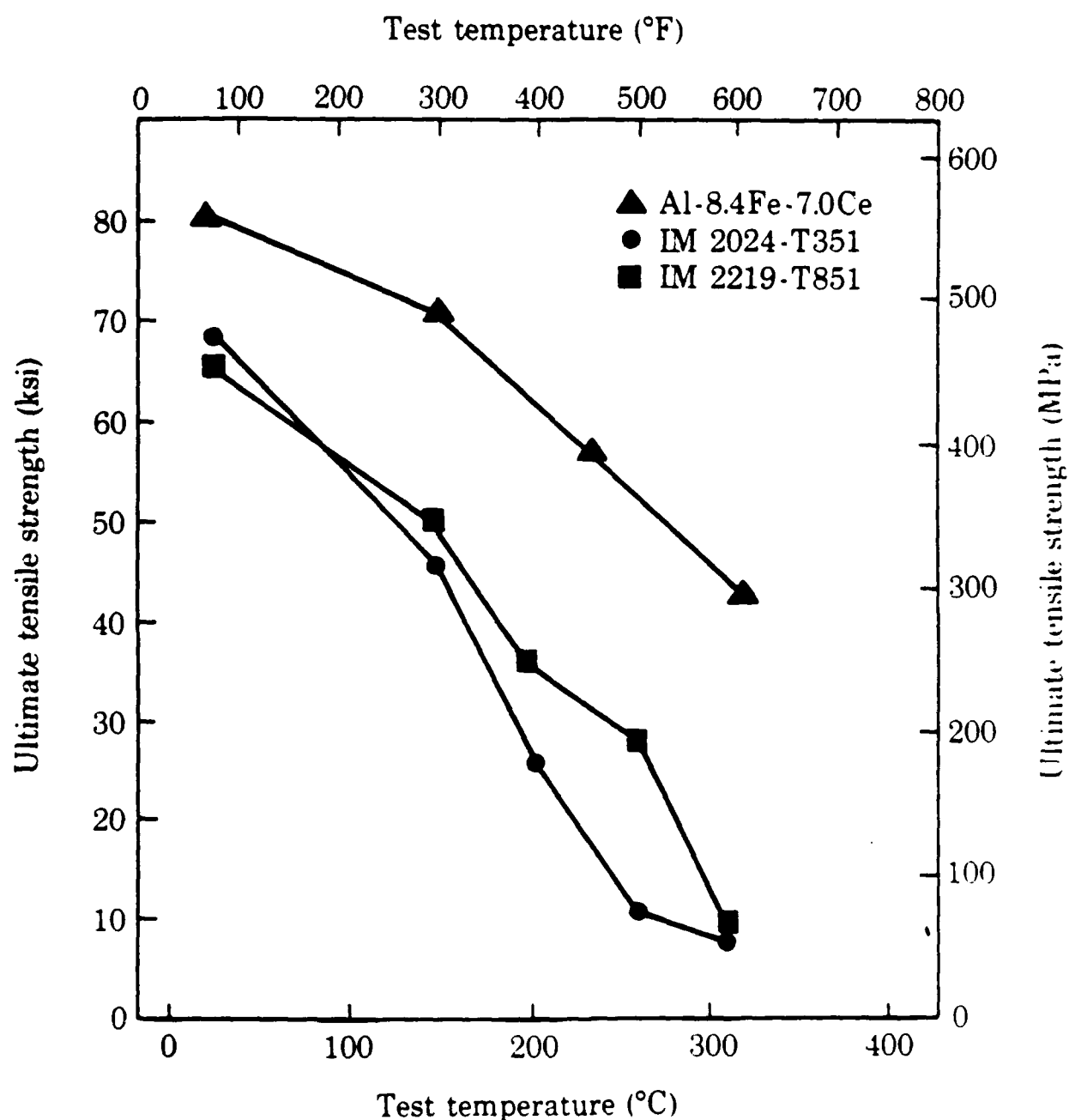


Figure 1 - Tensile strength versus test temperature for RS/PM Al-8.4Fe-7.0Ce and IM 2024-T351 and 2219-T851. Note that the Al-8.4Fe-7.0Ce alloy was tested after 1000 hours at 150 and 232°C (300 and 450°F) and 100 hours at 315°C (600°F) (Refs. 2 and 3).

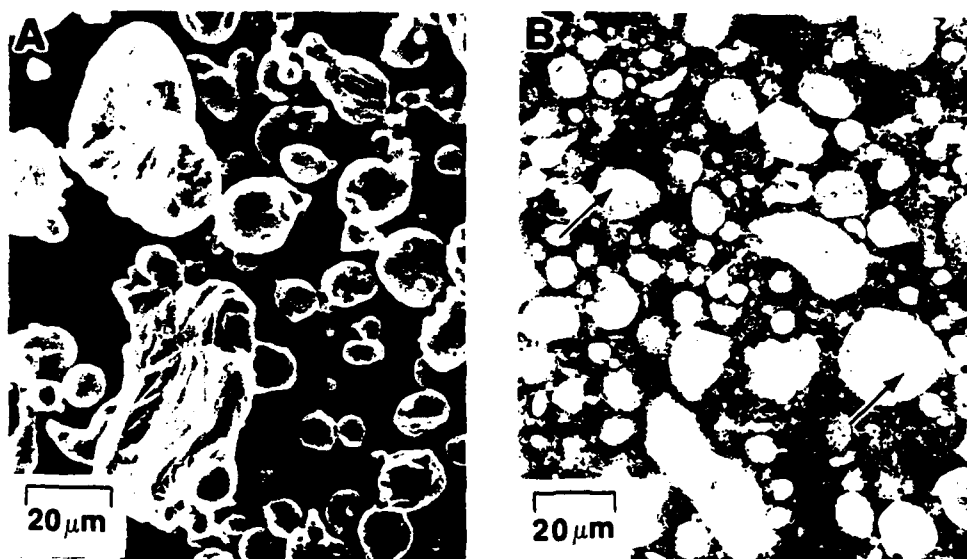


Figure 2 - SEM (A) and light (B) micrographs of Al-9Fe-4Ce flue-gas atomized powder. Arrows indicate featureless, Zone A regions.

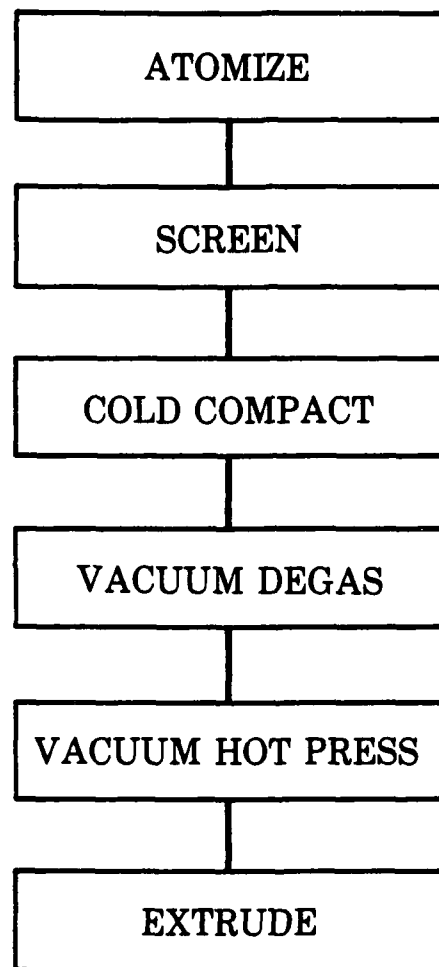


Figure 3 - Processing sequence for Al-Fe-Ce powder.

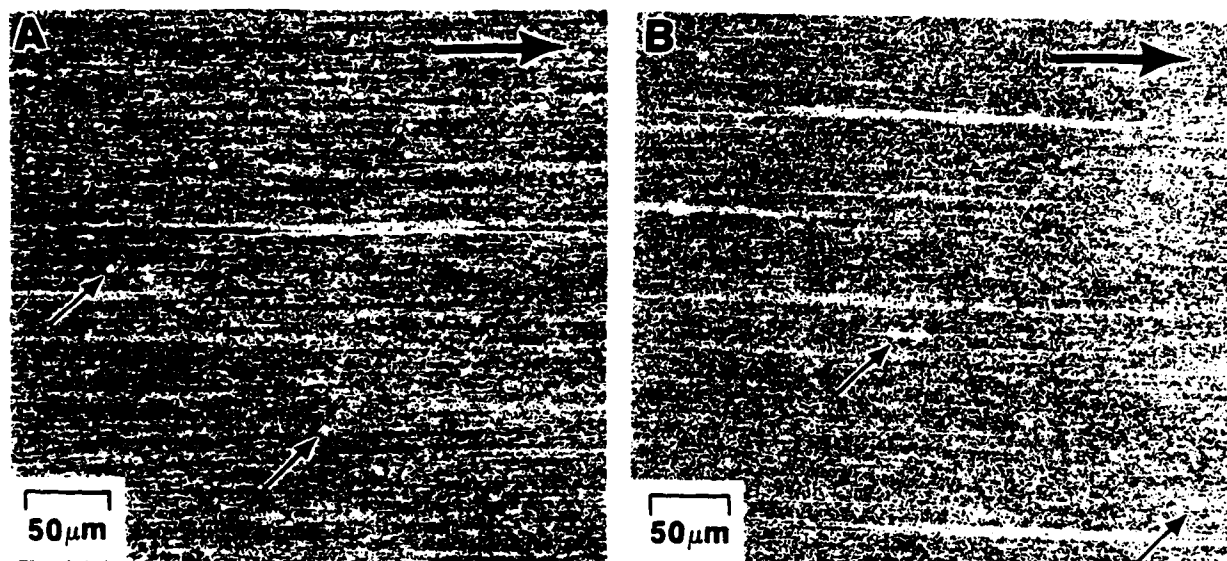


Figure 4 - Light micrographs of (A) Al-9Fe-4Ce and (B) Al-9Fe-7Ce base metal microstructures. Large arrows indicate extrusion direction. Small arrows indicate undeformed powder particles.

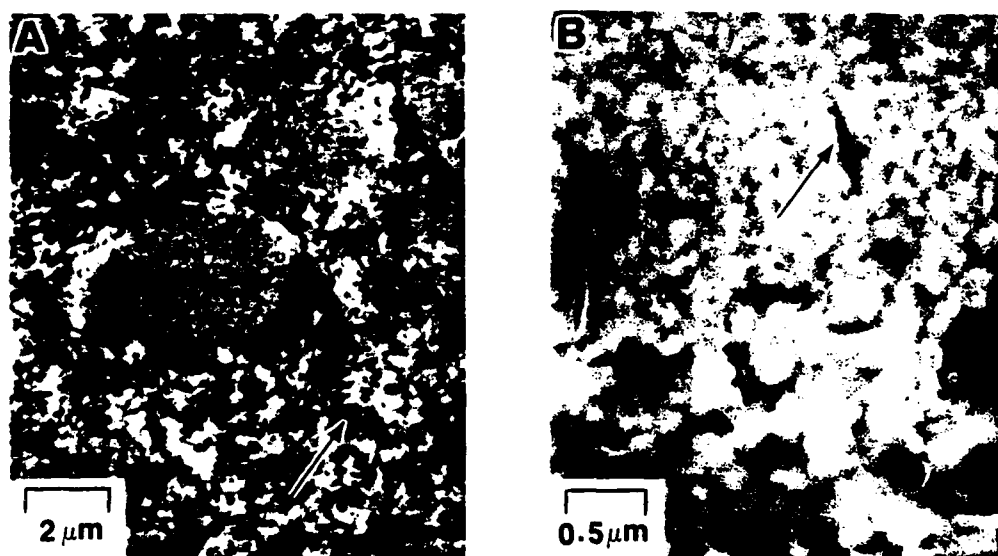


Figure 5 - SEM micrographs of Al-9Fe-4Ce base metal microstructure. Arrows indicate fine intermetallics.

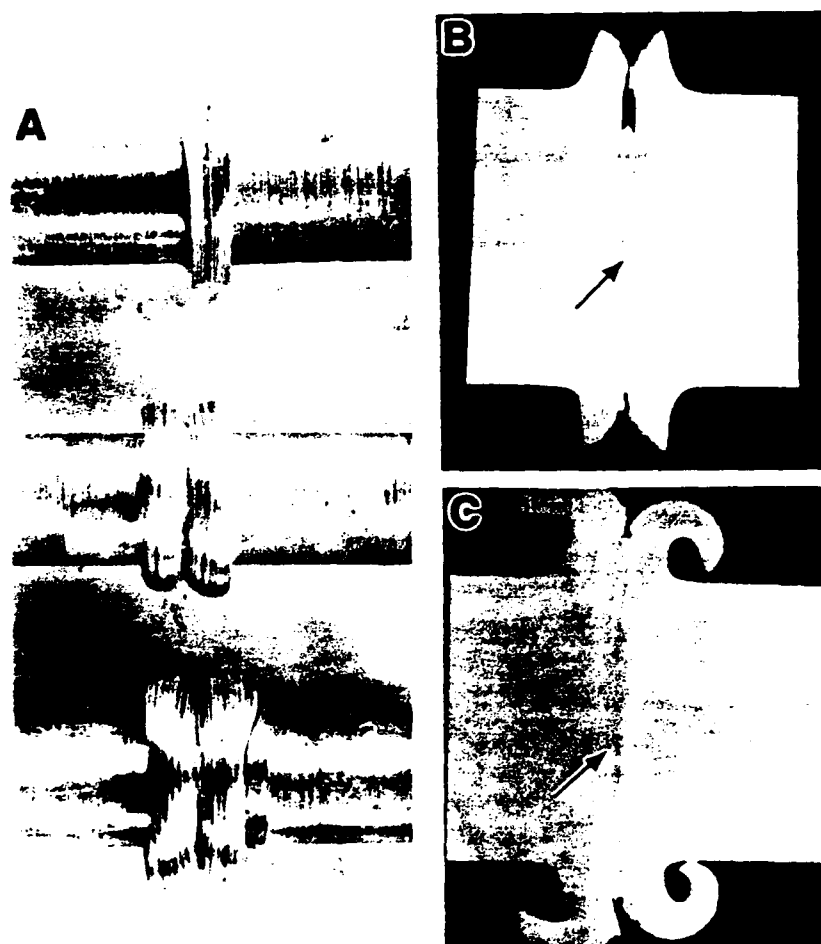


Figure 6 - Inertia-friction welds in Al-9Fe-4Ce: (A) as-welded specimens produced at low, medium and high axial force (top-to-bottom); (B,C) axial sections of welds produced at low and high axial forces; respectively. Arrows in B and C indicate weld interface.

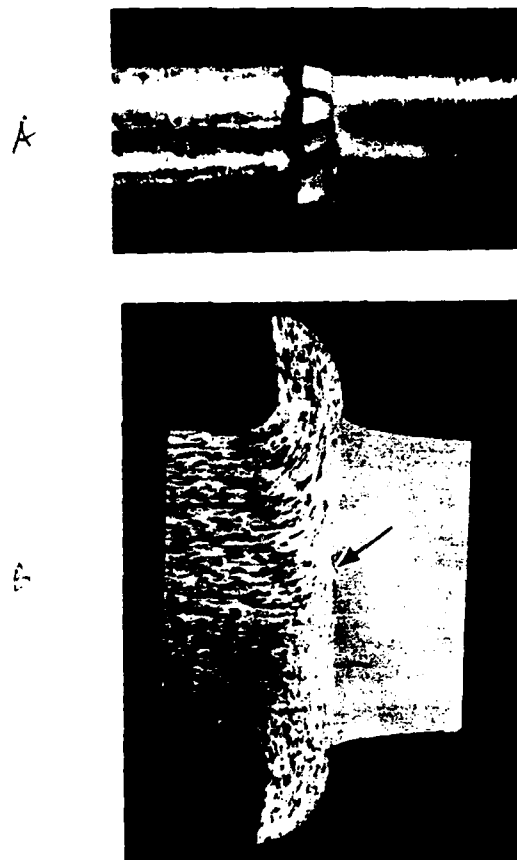


Figure 7 - Inertia-friction weld between Al-9Fe-4Ce (left side) and 2024-T351(right side) (A) as-welded specimen, (B) axial section, arrow indicates weld interface.

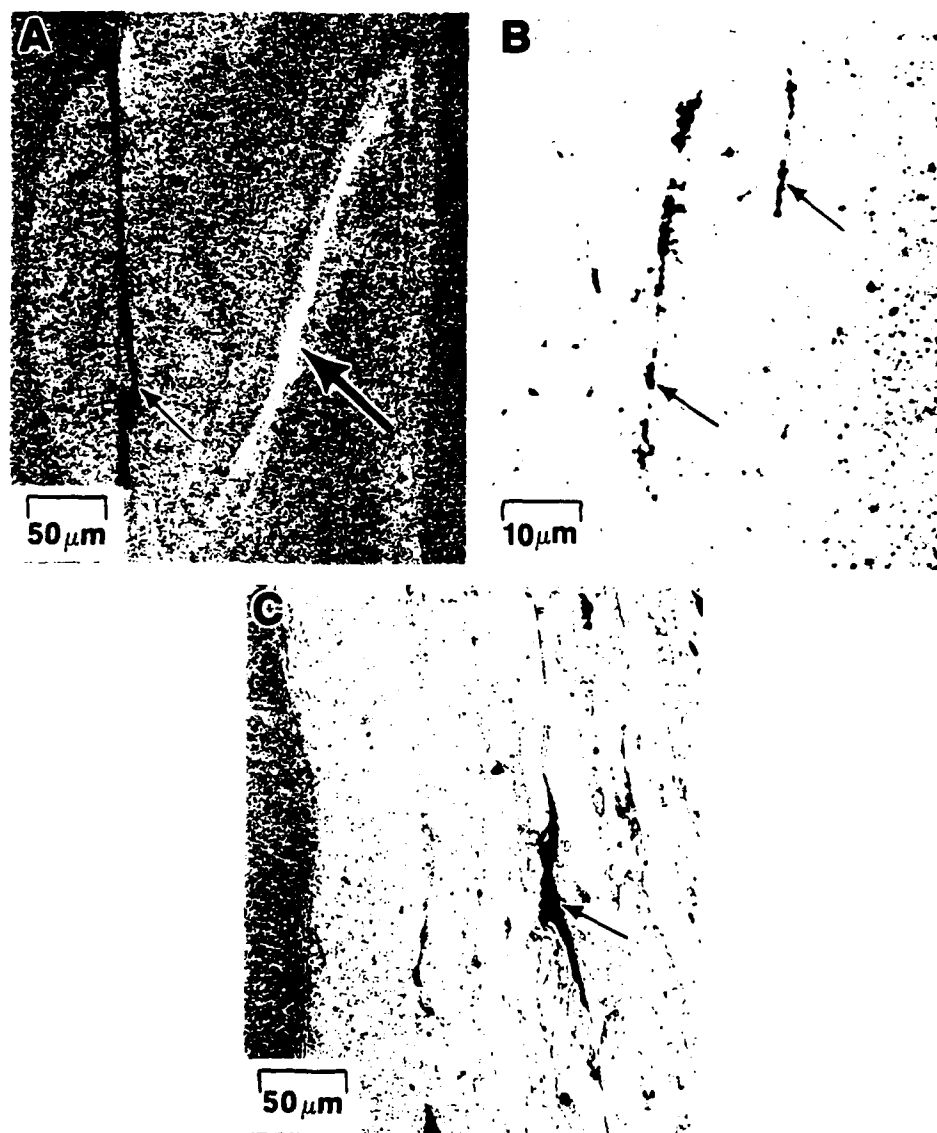


Figure 8 - Defects in (A,B) Al-9Fe-7Ce low axial force weld and (C) Al-9Fe-4Ce /2024-T351 dissimilar alloy weld: (A) coarse, linear defect near outer periphery (etched); (B) fine, linear defect near weld centerline (unetched); (C) intergranular cracks adjacent to weld interface in 2024-T351. Small arrows indicate defects, large arrow in (A) indicates apparent Zone A solidification product.

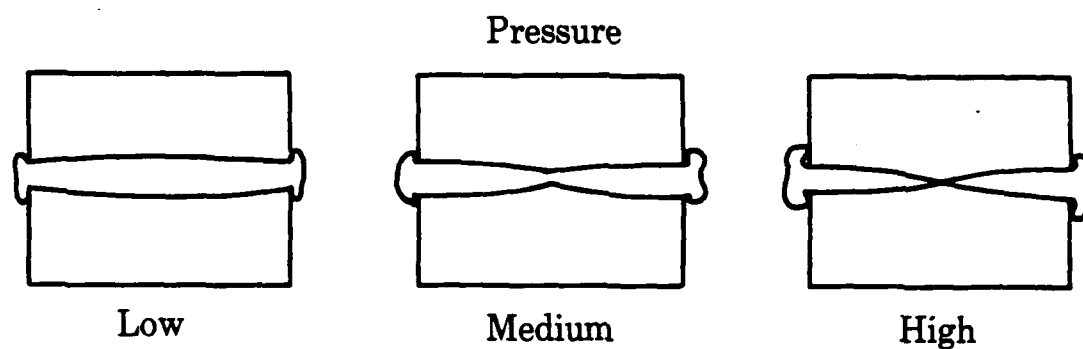


Figure 9 - Schematic illustrating the general effect of axial force on heat and deformation zone geometry for similar alloy inertia-friction welds.

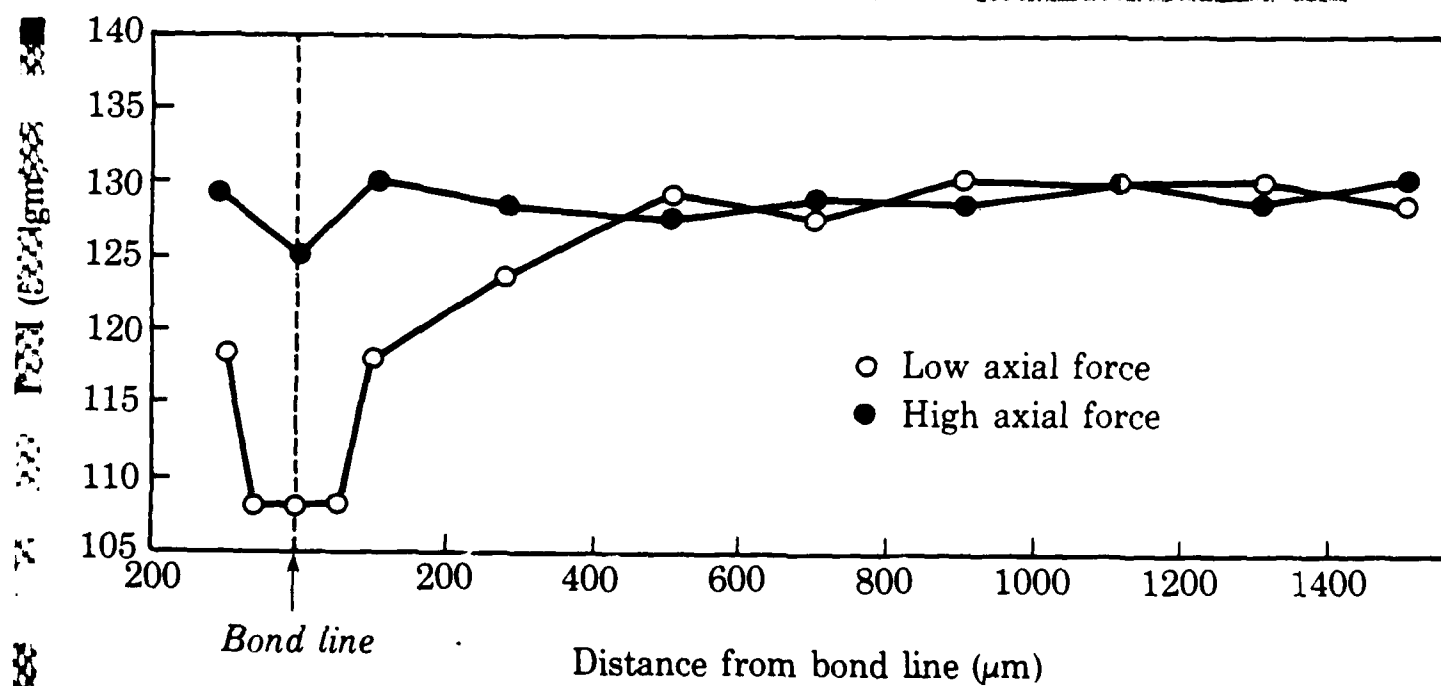
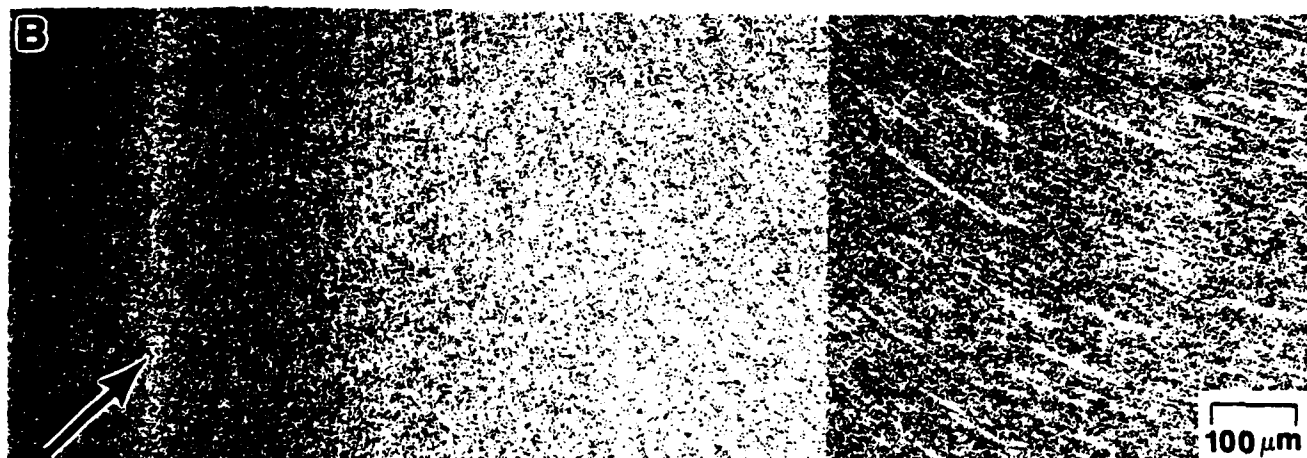
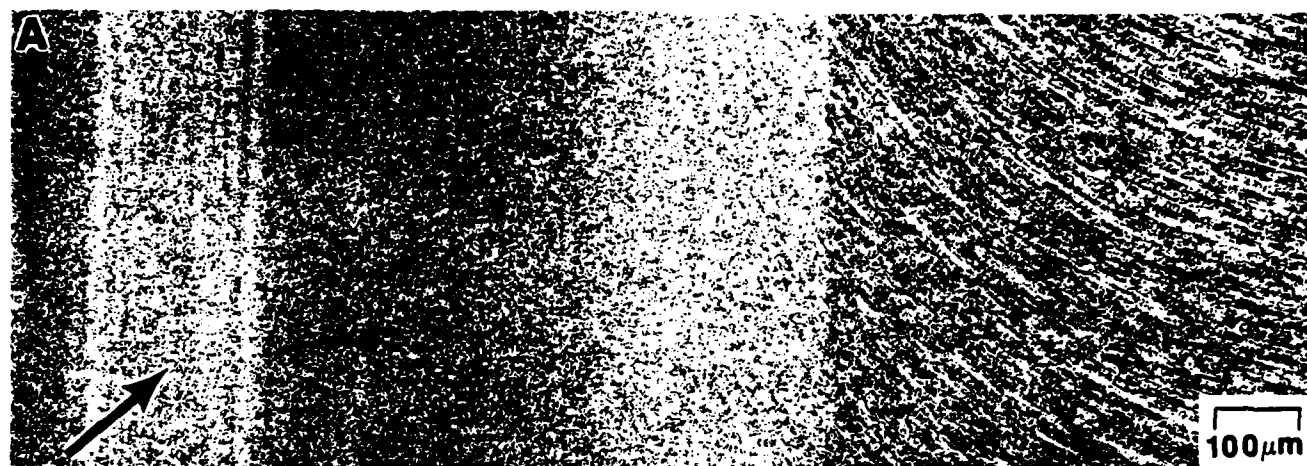


Figure 10 - Microstructures (A, B) and diamond pyramid hardness traverse (C) near center of inertia-friction welds in Al-9Fe-4Ce produced at (A) low and (B) high axial force. Arrows indicate weld interface.

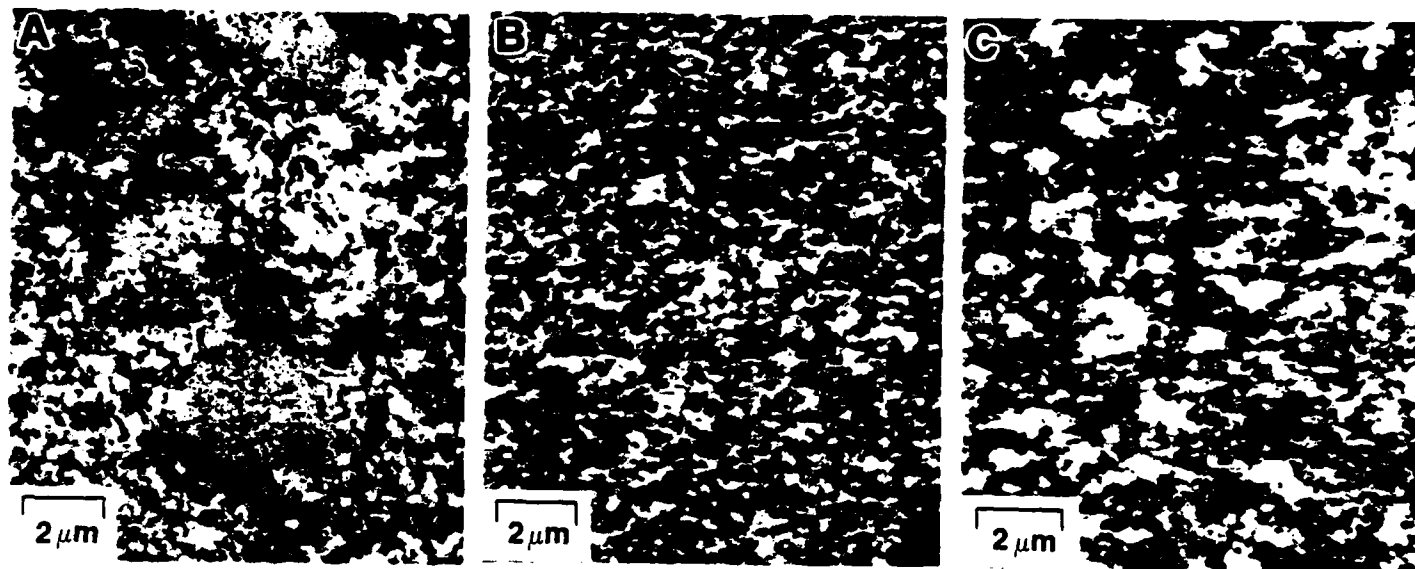


Figure 11 - SEM micrographs showing dispersoid coarsening across weld unaffected base metal (A) into the HNZ (B) and finally at the interface (C).

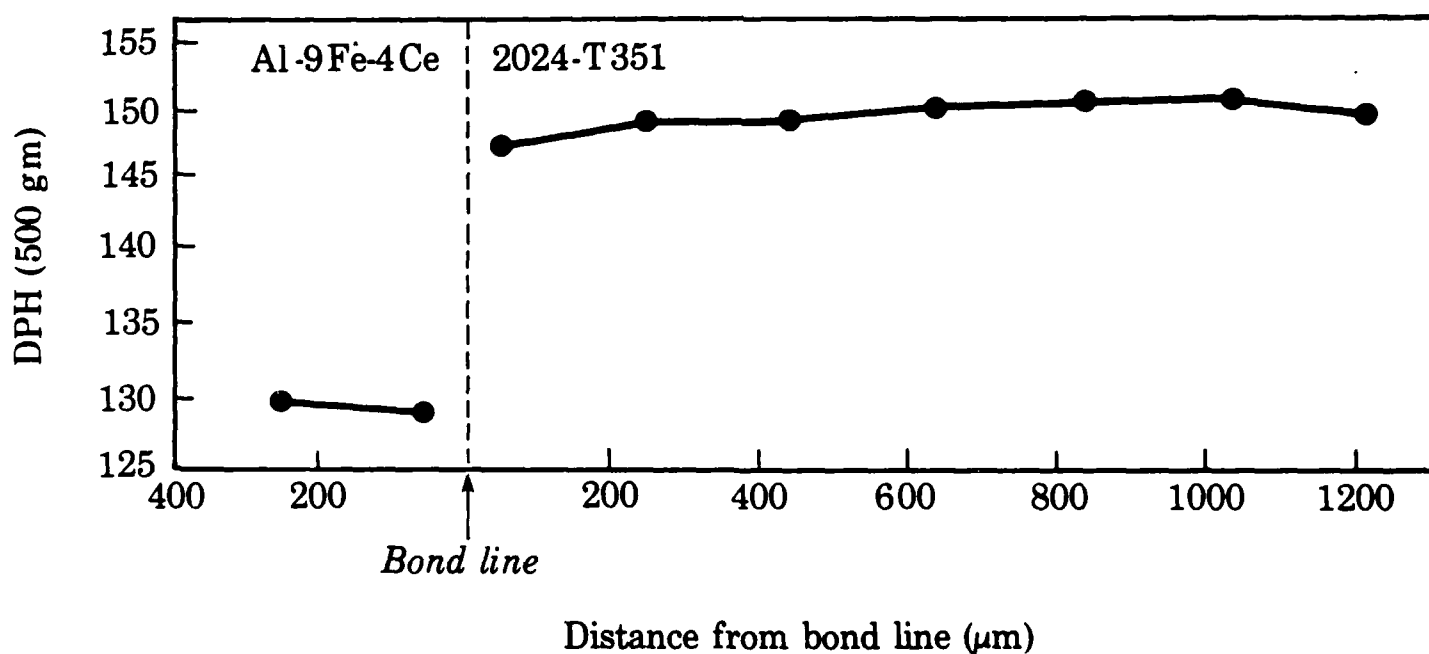


Figure 12 - Microstructure and diamond pyramid hardness traverse near center of inertia-friction weld produced between Al-9Fe-4Ce and 2024-T351. Arrow indicates weld interface.



Figure 13 - Light micrograph showing bond region in Al-9Fe-4Ce dissimilar alloy inertia-friction weld. Large arrow indicates weld interface, small arrows indicate intermetallics at alpha grain boundaries in 2024-T351.

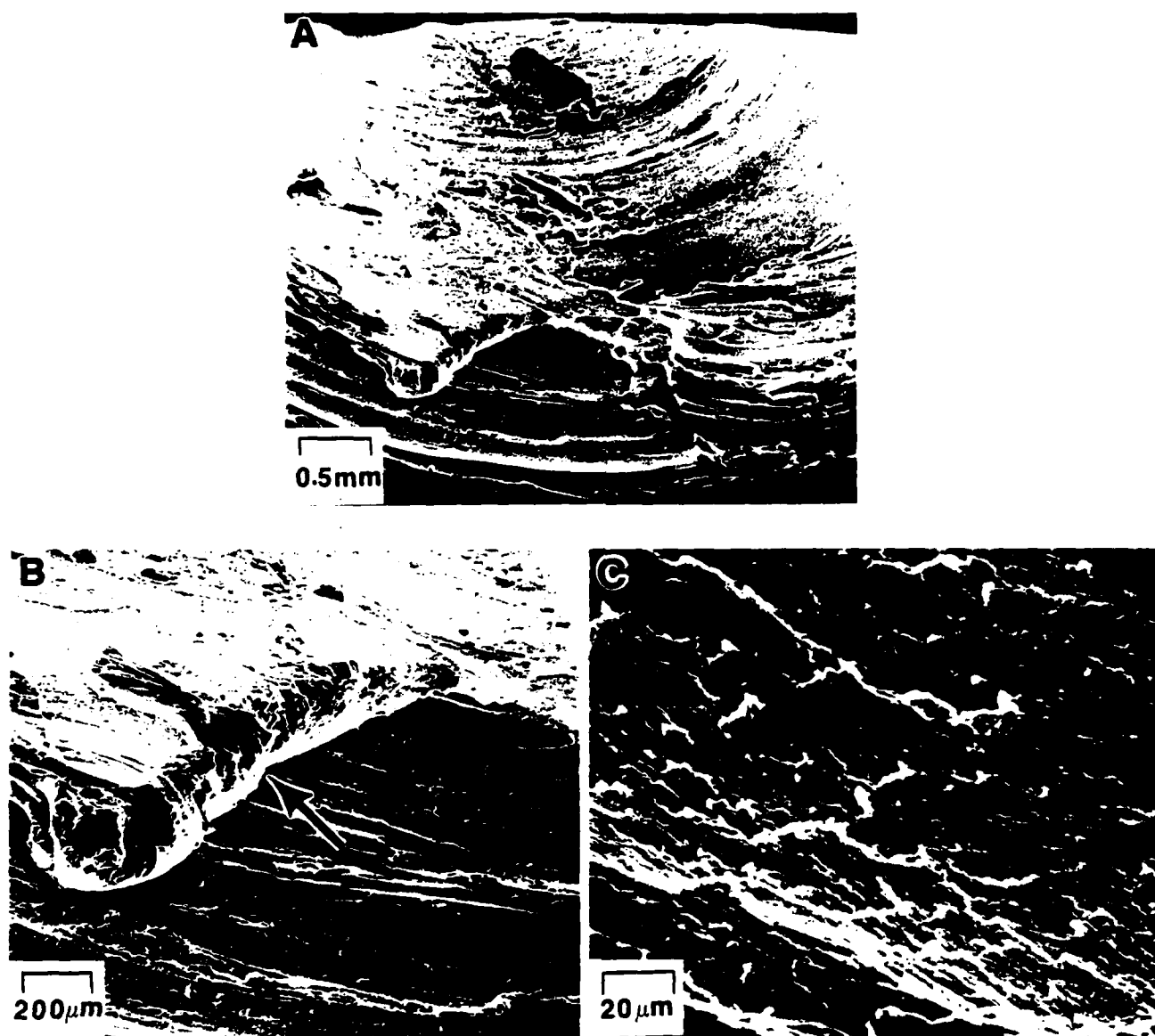


Figure 14 - SEM fractographs of bend tested Al-9Fe-4Ce inertia-friction weld produced at low axial force: (A) macroscopic fracture surface, (B) flat fracture near outer periphery and "cliff" (arrow) bounding void, (C) surface of void at increased magnification.

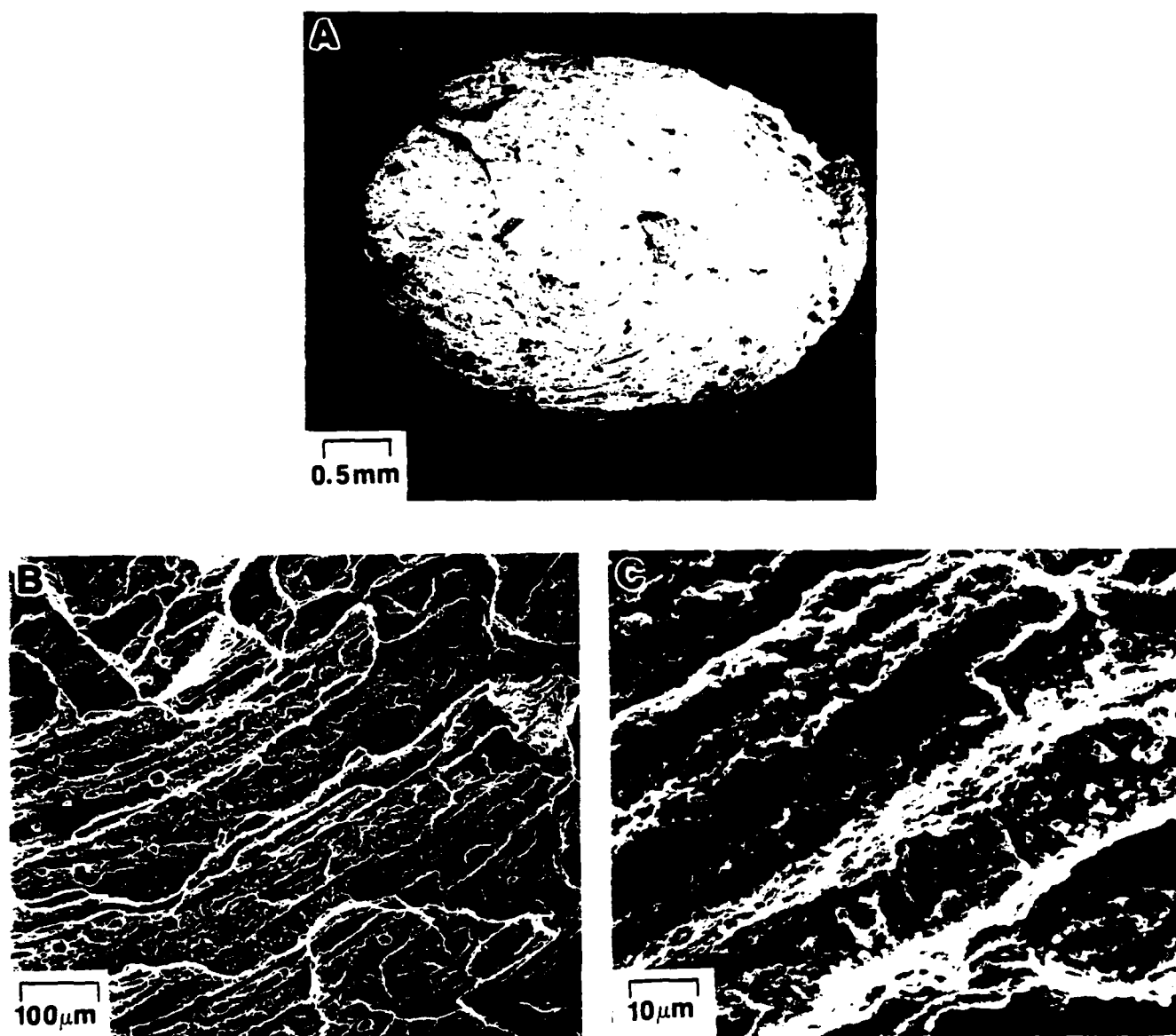


Figure 15 - SEM fractographs of tensile tested Al-9Fe-4Ce inertia-friction weld produced at low axial force: (A) macroscopic fracture surface, (B) spiral pattern indicating metal flow during welding, (C) dimpled fracture surface at increased magnification.

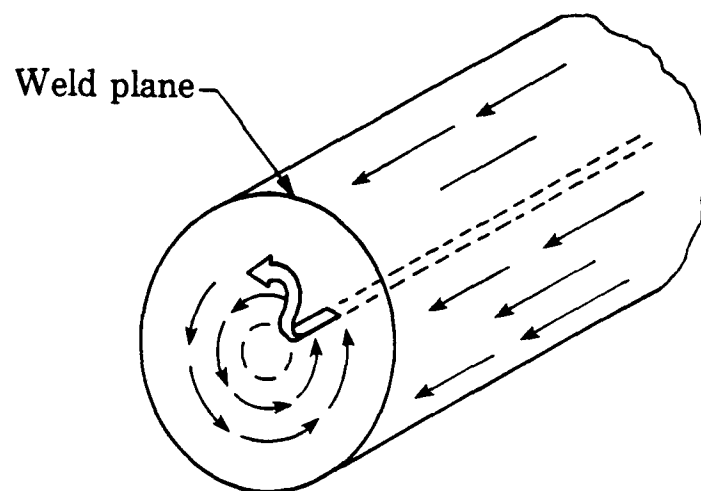


Figure 16 - Schematic illustration of metal flow during inertia-friction welding (Ref. 6).

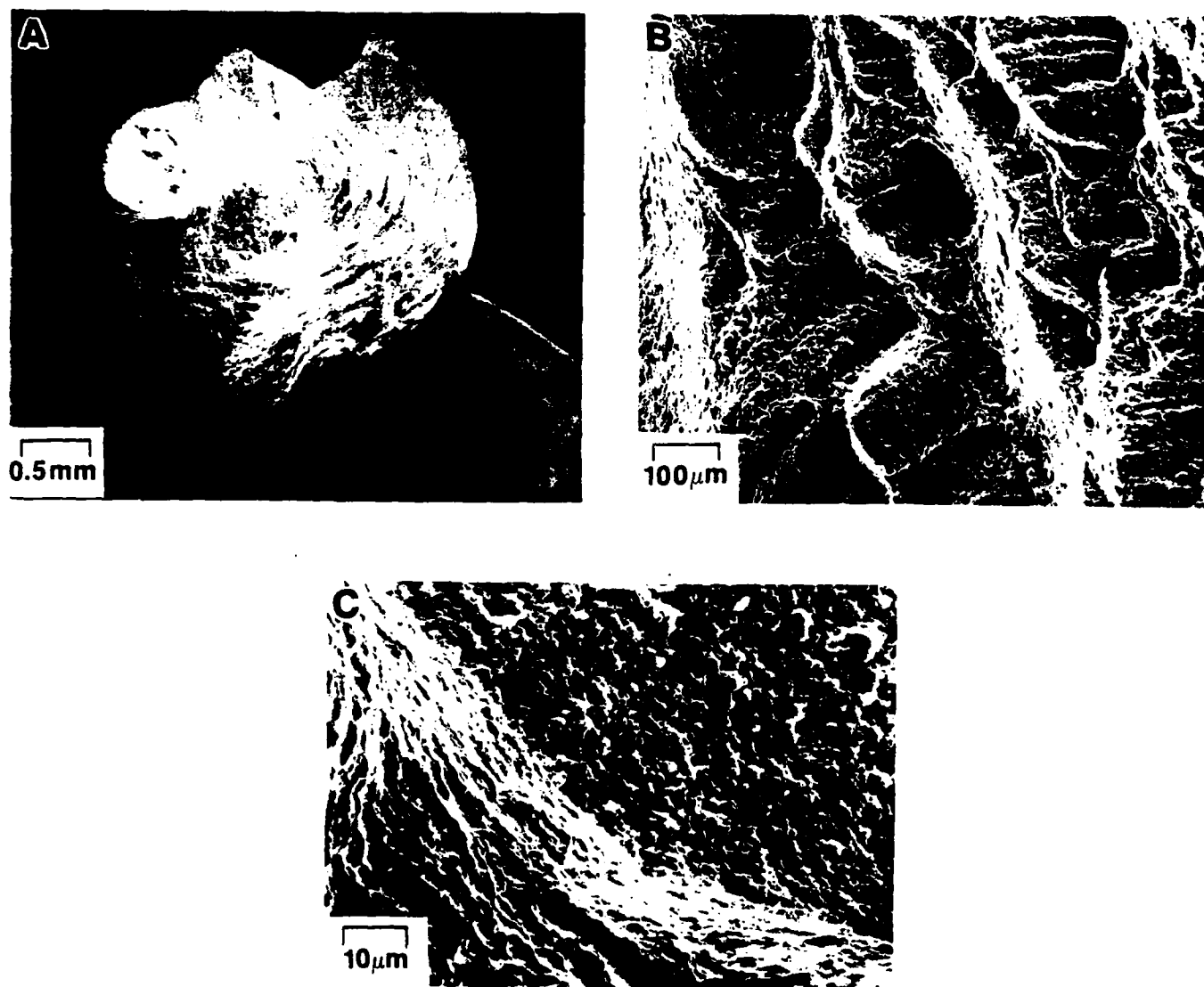


Figure 17 - SEM fractographs of tensile tested Al-9Fe-4Ce inertia-friction weld produced at high axial force: (A) macroscopic fracture surface, (B, C) interface fracture surface at increased magnification.

APPENDIX ID

W. A. Baeslack III, K. H. Hou and J. H. Devletian, "Rapid Solidification Joining of a Powder Metallurgy Al-Fe-Ce Alloy, Journal of Materials Science Letters, (in press).

Rapid Solidification Joining of a Powder Metallurgy

Al-Fe-Ce Alloy

W.A. Baeslack III,* K.H. Hou* and J.H. Devletian**

*Department of Welding Engineering
The Ohio State University
Columbus, OH 43210 USA

**Department of Materials Science and Engineering
Oregon Graduate Center
Beaverton, OR 97006 USA

Aluminum-iron-cerium alloys represent an important new family of rapidly-solidified, powder metallurgy aluminum alloys designed for elevated-temperature applications up to 300°C [1,2]. These alloys are hypereutectic aluminum-iron compositions with ternary additions of cerium for improved dispersoid thermal stability. Through rapid solidification, the formation of coarse, primary intermetallics is suppressed and solidification instead occurs to supersaturated alpha phase. Subsequent powder consolidation and thermomechanical processing promote the formation of extremely fine, thermally-stable dispersoids in a matrix of submicron alpha grains. This unique microstructure provides moderate to high room-temperature strength and excellent elevated-temperature properties.

The utilization of Al-Fe-Ce alloys as potential replacements for conventional aluminum and titanium alloys will require the development of joining methods which can effectively "recreate" and/or "retain" in the weld zone the metastable microstructures upon which these alloys depend for their unique mechanical properties. To date, conventional fusion

welding techniques have been applied with limited success to Al-Fe-Ce alloys. Poor weld quality has resulted primarily from the inherently high hydrogen content of the alloys (> 1 ml/100gm) and the associated evolution of fusion zone porosity. Also, the relatively slow cooling rates experienced during most fusion welding processes allow fusion zone solidification to undesirable, near-equilibrium microstructures and appreciable microstructural coarsening and softening in the weld heat-affected zone (HAZ). Recent joining studies on SiC/Al metal-matrix composites exhibiting similarly high hydrogen contents have demonstrated that the capacitor-discharge (CD) welding process can successfully generate weldments free of gaseous porosity [3]. In addition, the extremely rapid heating and cooling rates associated with the CD process ($\sim 10^6$ C/s) provided rapid solidification rates in the melt zone and minimized HAZ formation. Considering these advantages, it is apparent that the CD process may also represent an effective method for producing defect-free, rapidly-solidified weldments in Al-Fe-Ce alloys. The present study examined this potential by characterizing the metallurgical structure, properties and fracture behavior of CD weldments produced in a semi-commercial Al-Fe-Ce alloy.

The Al-8.4Fe-3.6Ce (Al-8Fe-4Ce) alloy studied in the present investigation was produced by flue-gas atomization. As shown in Figure 1a, the as-solidified powder particles were irregularly shaped and ranged in size from approximately 5 to 40 microns in diameter. Powder processing involved cold compaction, hot vacuum degassing, hot pressing and extrusion to 5.1 cm diameter rod. Cylindrical rods 6.4 mm in diameter and approximately 25 mm in length were machined with the

longitudinal rod axis parallel to the extrusion direction. Conical ignition tips were machined onto one of the two faying workpiece surfaces prior to welding. In the initial gap CD welding process, the weld specimens impact under gravity, causing arcing and subsequent melting by the discharge of a capacitor bank. When the components impact the arc is extinguished, excess molten metal is expelled, and solidification occurs. Both "high" and "moderate" cooling rate welds ($\sim 10^5$ and 10^7 °C/s, respectively [4]) were produced using welding parameters shown in Table 1. Representative welds were sectioned axially, mounted in epoxy and mechanically polished. After defect analysis of the as-polished surface, microstructure characteristics were revealed by etching with Keller's reagent and examined using light and scanning-electron microscopy (SEM). Diamond pyramid hardness traverses were performed across the weld interface at several distances from the axial centerline. Additional weldments were sectioned axially and three-point bend tested in both the as-welded condition and after removal of the flash and/or ledge at the weld outer periphery. SEM was utilized for fractographic analysis.

Metallographic examination of powder particles showed the finest, most rapidly-cooled particles to exhibit a featureless microstructure designated in the literature as "Zone A" (Fig. 1b) [5]. In contrast, the coarser, more slowly cooled particles were characterized by a dark-etching microstructure designated as "Zone B." In the Al-8Fe-4Ce powder, both the Zone A and Zone B microstructures solidified as primary alpha in a cellular mode, with the Zone B contrast resulting from a coarser cell structure.

The extruded base metal microstructure illustrated in Fig. 2a

AD-A194 677

AN INVESTIGATION INTO THE METALLURGICAL ASPECTS OF
JOINING RAPIDLY-SOLIDIFIED (U) OHIO STATE UNIV RESEARCH
FOUNDATION COLUMBUS W A BAESLACK 01 APR 88

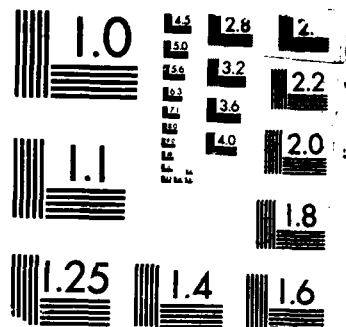
2/2

UNCLASSIFIED

ARO-20987.4-MS DAAG29-84-K-0176

F/G 11/6.2 NL





MICROCOPY RESOLUTION TEST CHART
BUREAU OF STANDARDS-1963-A

exhibited good homogeneity and a light texture parallel to the extrusion direction. Also evident were occasional fine powder particles which retained a spherical shape during processing due to the high hardness of their Zone A microstructures (> 200 DPH). SEM analysis revealed a variety of fine, needle-shaped intermetallics in a matrix of alpha aluminum (Fig. 2b). Previous TEM electron diffraction and X-ray diffractometry studies of this microstructure identified several different intermetallics and their metastable precursor phases, including Al_3Fe , Al_6Fe and $Al-Fe-Ce-2$ (orthorhombic) [6].

Visual examination of the CD welds revealed minimal flash at the outer periphery. However, due to a slight axial misalignment of the specimens during welding, both weld types exhibited a narrow "ledge" at the weld outer periphery.

As illustrated in Figure 3, the rapid solidification rates experienced by the high cooling rate CD welds promoted fusion zone solidification to a featureless, Zone A microstructure. Fusion zone width was found to be relatively uniform across the specimen cross section, gradually narrowing at the outer periphery (Fig 3b). At the fusion zone/base metal interface, the presence of a narrow partially-melted region (PMR) was evidenced dispersed intermetallics in a predominantly Zone A matrix (Fig. 3c). Despite large differences between the melting temperatures of the matrix and the intermetallics, the extremely high temperature gradients across the weld interface minimized the width of this region. The presence of a HAZ outside of the PMR was not apparent with light microscopy and SEM. Microhardness traverses across the weld interface indicated extremely high fusion zone hardnesses

minimal heat-affect in this region. As in the high cooling rate welds, occasional spherical and elongated pores were observed at the weld centerline (Fig. 4c).

Progressive three-point bend tests performed on the as-welded and axially-sectioned specimens (flat side in tension) showed a significant reduction in bend ductility versus the base metal (Table II). Analysis of the fractured specimens showed fracture initiation at the outer periphery notch (Figs. 5a-c). However, specimen fracture occurred principally in the unaffected base metal remote from the weld interface. Removal of the flash/ledge region by grinding significantly improved bend ductilities to near base metal values in the high cooling rate welds. As shown in Fig. 6a, fracture initiated at a solidification shrinkage cavity or pore at the center of the weld fusion zone. The smooth, liquated-appearing surface typical of these solidification-related defects (Fig. 6b) differed distinctly from the ductile-appearing, base metal fracture surface (Fig 6c). Secondary cracking perpendicular to the fracture surface was also in evidence. Despite the presence of similar fusion zone defects in the moderate-cooling rate welds, fracture occurred exclusively in the unaffected base metal at base metal ductility levels.

Results of the present investigation have demonstrated that the CD welding process can successfully generate rapidly-solidified weld microstructures in PM Al-Fe-Ce alloys. Despite high hydrogen levels, porosity formation was minimal and did not significantly influence weld ductility. In addition, the high weld zone hardnesses and absence of HAZ softening were indicative of high joint efficiencies. The presence of an outer periphery notch due to specimen misalignment and excessive flash,

however, was observed to significantly reduce bend ductility. It is anticipated that these weld defects could be eliminated through improved process parameter control, thereby optimizing weld properties.

References

1. W.E. QUIST AND R.E. LEWIS, "Rapidly-Solidified Powder Aluminum Alloys, ASTM STP 890" (American Society for Testing Materials, Philadelphia, PA, 1986) p. 7-38.
2. S.L. LANGENBECK, W.M. GRIFFITH, G.J. HILDEMAN AND J.W. SIMON, "Rapidly Solidified Powder Aluminum Alloys, ASTM STP 890" (American Society for Testing Materials, Philadelphia, PA, 1986) p. 410-422.
3. J.H. DEVLETIAN, Weld. J. 67 (1987) 33.
4. S. Venkataraman and J.H. Devletian, Weld. J. (in press).
5. L.M. ANGERS, Ph.D. Dissertation, Northwestern University, (1985).
6. H. JONES, Materials Sci. and Eng. 5 (1969) 1.

Acknowledgements

The authors are indebted to Dr. G.J. Hildeman of ALCOA for providing the PM Al-Fe-Ce alloy. Appreciation is also expressed to the Army Research Office for support of this work under Contract No. DAAG29-84-0176. Finally, the metallographic assistance of Mr. S. Krishnaswamy is acknowledged.

List of Figures

- Figure 1. SEM (a) and light (b) micrographs of Al-8Fe-4Ce flue-gas atomized powder. Arrows indicate featureless, Zone A regions.
- Figure 2. Light (a) and SEM (b) micrographs of Al-8Fe-4Ce base metal microstructure. Arrows indicate undeformed Zone A powder particles.
- Figure 3. Light micrographs of high cooling rate CD weld in Al-8Fe-4Ce: (a) fusion zone (white etching) at weld centerline; (b) fusion zone at weld outer periphery; (c) fusion zone at weld center line at increased magnification, large arrow indicates pore or cavity, small arrows indicate undeformed Zone A powder particles in unaffected base metal.
- Figure 4. Light micrographs of moderate cooling rate CD weld in Al-8Fe-4Ce: (a) fusion zone at weld centerline (outlined by arrows); (b) fusion zone at weld outer periphery; (c) fusion zone at weld centerline at increased magnification (outlined by arrows), note porosity.
- Figure 5. Light micrograph (a) and SEM fractographs (b,c) of high cooling rate CD weld bend specimen in Al-8Fe-4Ce tested in "as-welded" condition: (a,b) fracture initiation site at specimen outer periphery, note

crack propagation through unaffected base metal; (c) liquated "ledge" surface at increased magnification.

Figure 6. SEM fractographs of high cooling rate CD weld bend specimen in Al-8Fe-4Ce tested after removal of outer periphery notch: (a) fracture initiation site at solidification-related weld defect near specimen center (arrow); (b) surface of defect at increased magnification, note secondary cracking perpendicular to fracture surface; (c) dimpled fracture surface of unaffected base metal.

TABLE I. Capacitor-discharge welding parameters

Parameter	Weld Specimen Type	
	High Cooling Rate	Moderate Cooling Rate
Stud Diameter:	6.4 mm	6.4 mm
Tip Base Diameter:	0.4 mm	0.8 mm
Tip Length:	0.5 mm	1.0 mm
Tip Shape:	60° conical	60° conical
Capacitance:	80,000 uF	80,000 uF
Voltage:	100V	100V
Drop Weight:	Head + 5.68 Kg	Head + 1.93 Kg
Drop Height:	50 mm	25 mm

TABLE II. Hardness and bend ductility of Al-8.4Fe-3.6Ce base metal and CD weld specimens

Specimen	DPH (50 gm load)	Bend Ductility*	Fracture Initiation Site
Base Metal	132-137	>20 %	-
HC Weld/AW	286-341**	3.3 %	outer periphery notch
HC Weld/AW	"	>16 %	FZ weld defect
MC Weld/notch	148-161**	3.7 %	outer periphery notch
MC Weld/smooth	"	>17 %	base metal

*Flat surface in tension

**Hardness at center of fusion zone

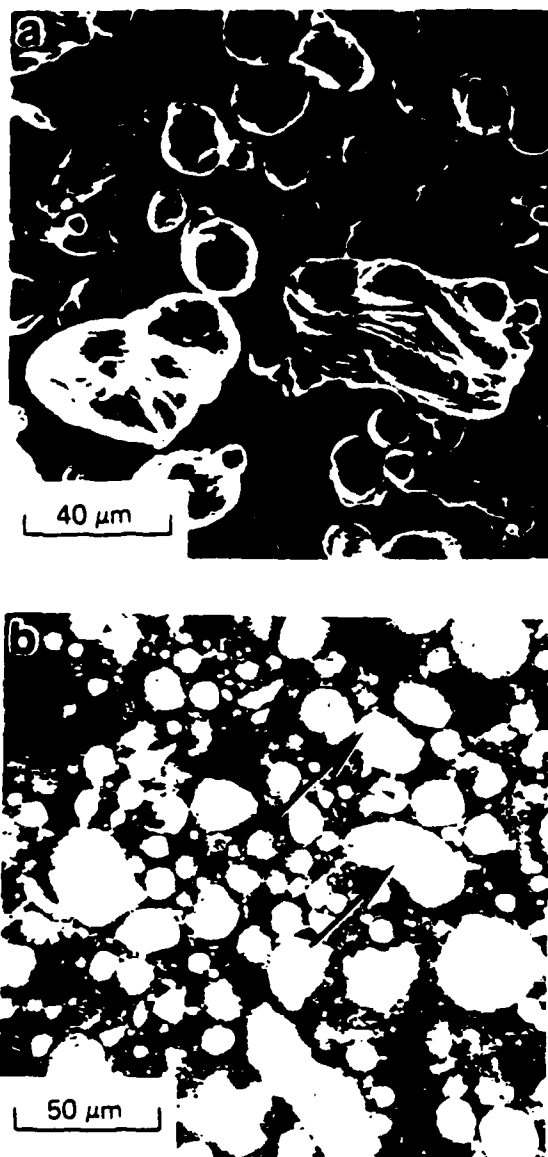


Figure 1. SEM (a) and light (b) micrographs of Al-8Fe-4Ce flue-gas atomized powder. Arrows indicate featureless, Zone A regions.

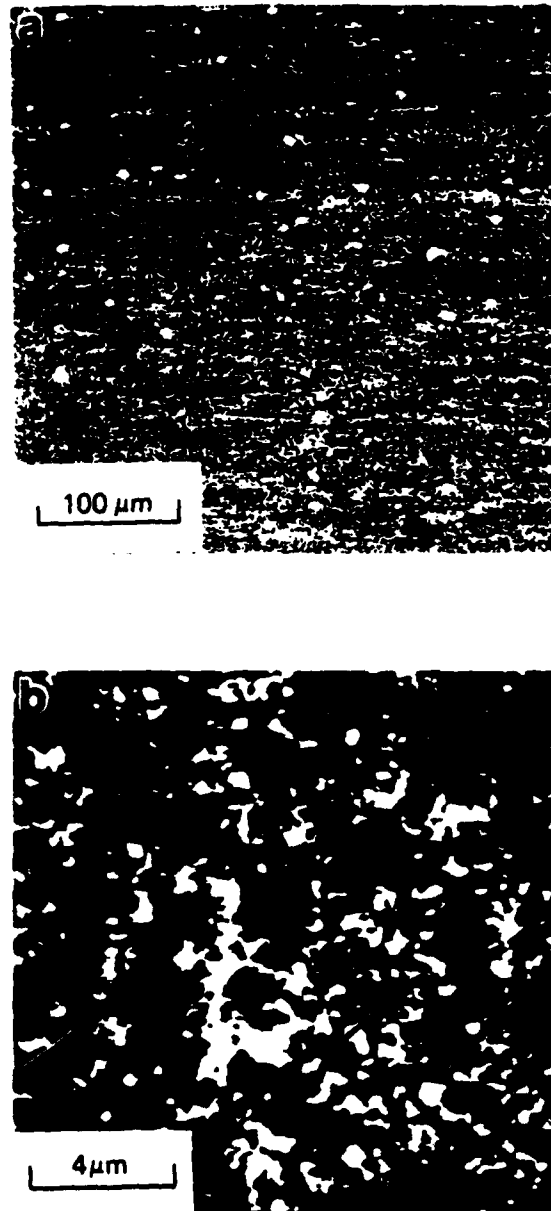


Figure 2. Light (a) and SEM (b) micrographs of Al-8Fe-4Ce base metal microstructure. Arrows indicate undeformed Zone A powder particles.

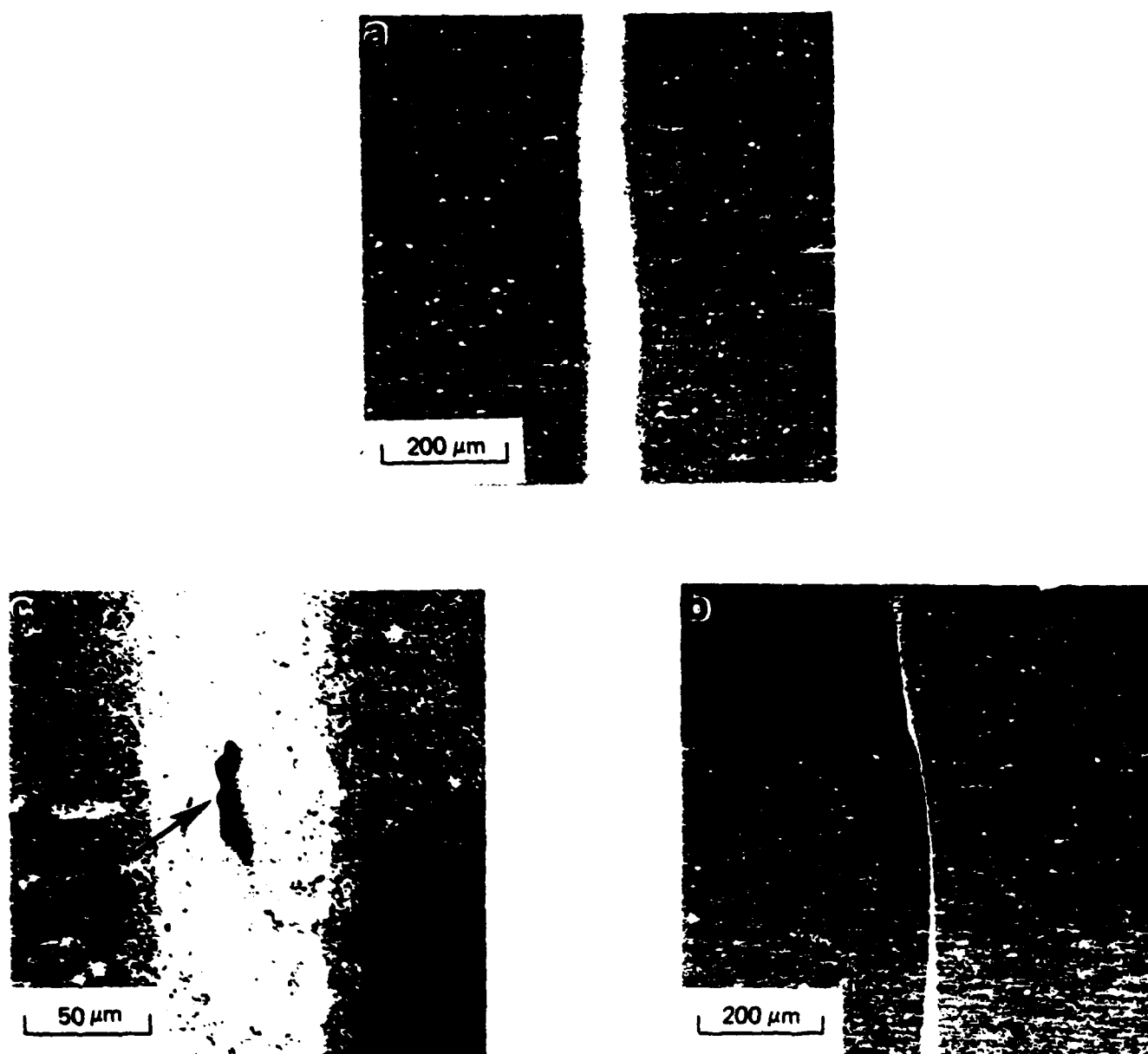


Figure 3. Light micrographs of "high cooling rate" CD weld in Al-8Fe-4Ce: (a) fusion zone (white etching) at weld centerline; (b) fusion zone at weld outer periphery; (c) fusion zone at weld center at increased magnification, large arrow indicates pore or cavity, small arrows indicate undeformed Zone A powder particles in unaffected base metal.

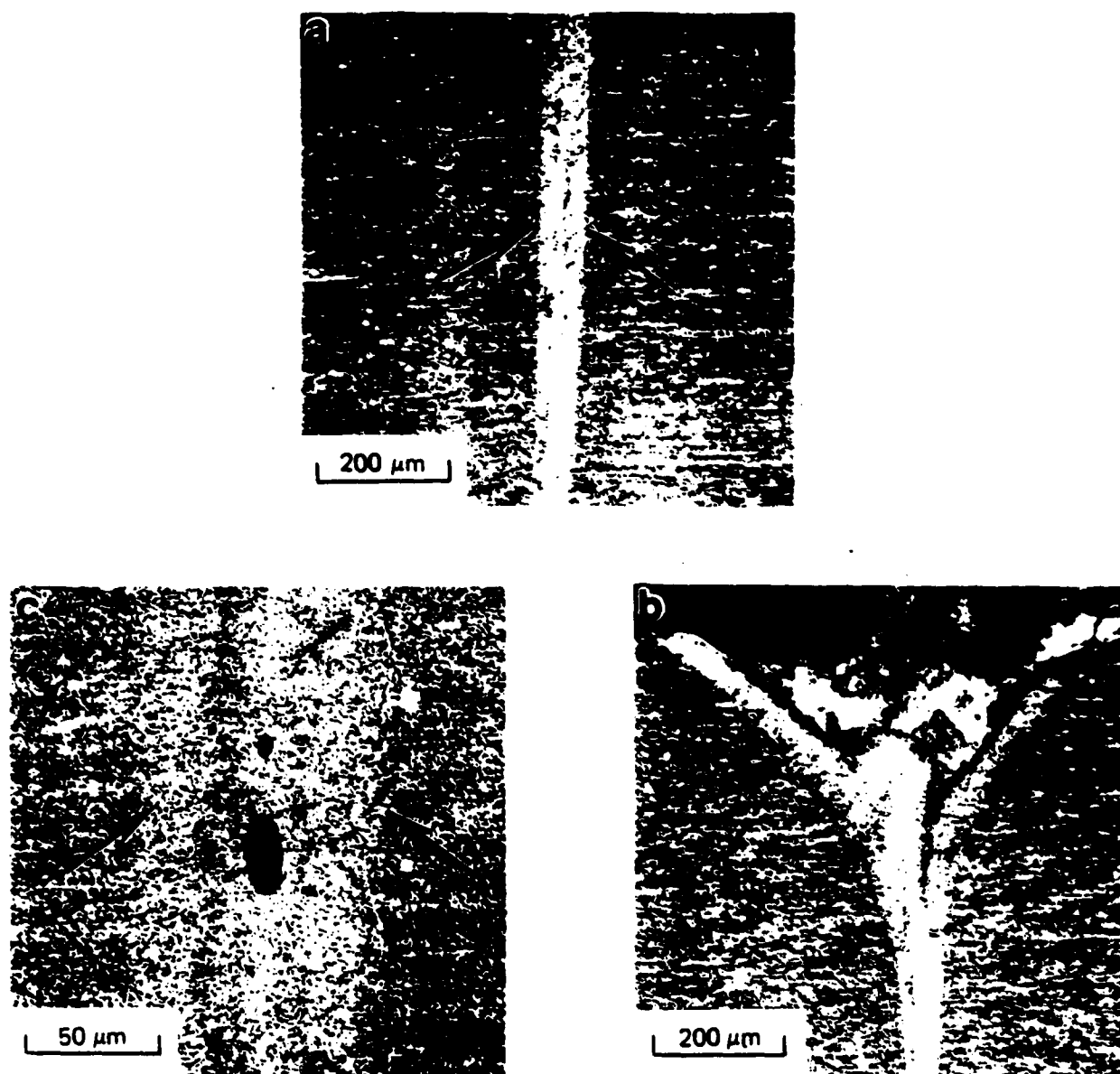


Figure 4. Light micrographs of "moderate cooling rate" CD weld in Al-8Fe-4Ce: (a) fusion zone at weld centerline (outlined by arrows); (b) fusion zone at weld outer periphery; (c) fusion zone at weld centerline at increased magnification (outlined by arrows, note porosity).

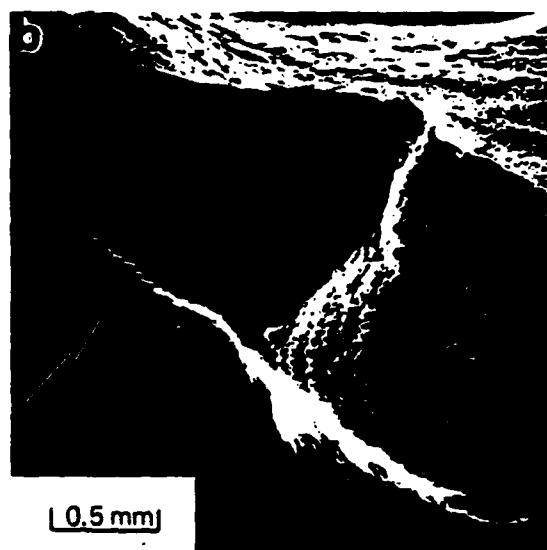
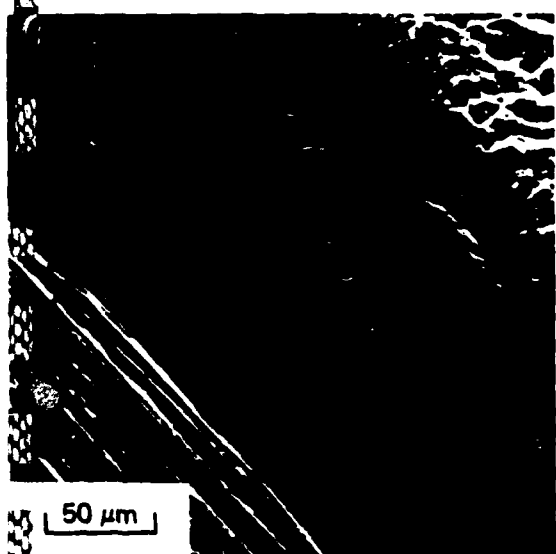
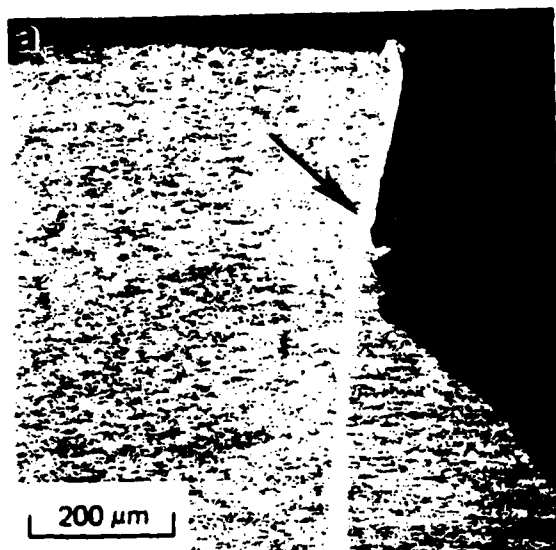


Figure 5. Light micrograph (a) and SEM fractographs (b,c) of high cooling rate CD weld bend specimen in Al-8Fe-4Ce tested in as-welded condition: (a,b) fracture initiation site at specimen outer periphery, note crack propagation through unaffected base metal; (c) liquated "ledge" surface at increased magnification.

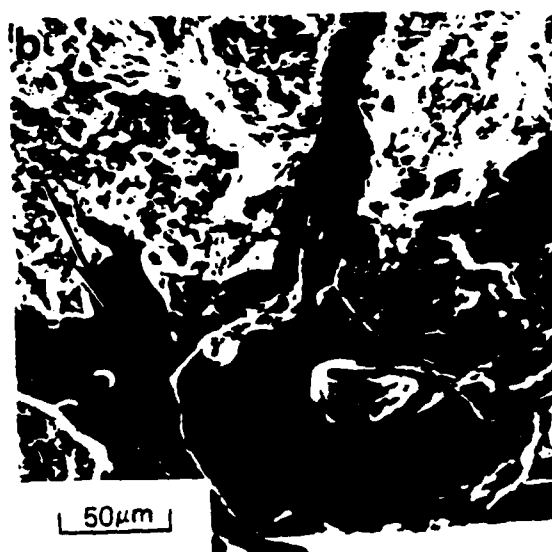
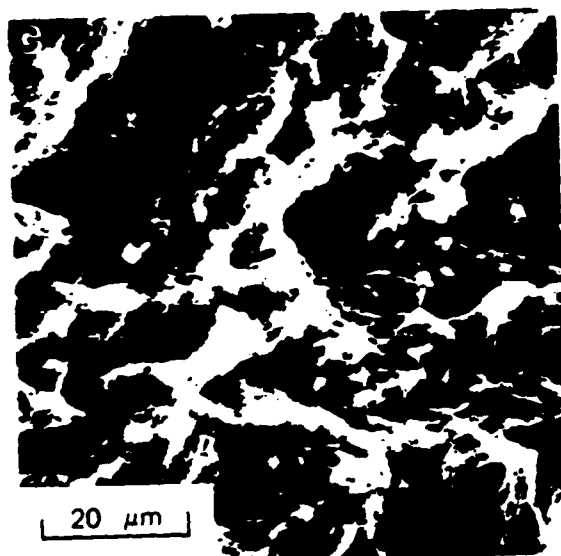
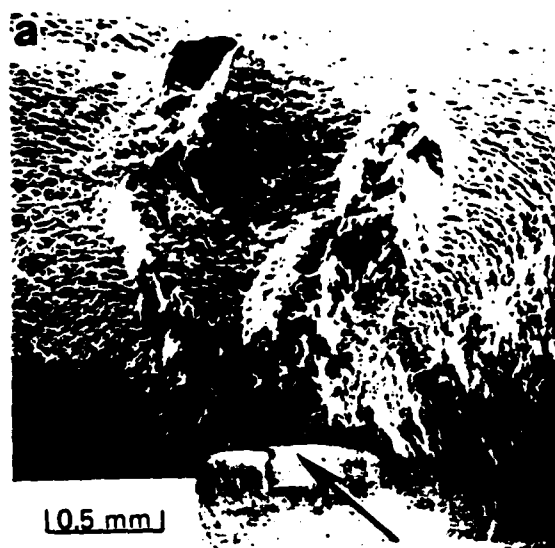


Figure 6. SEM fractographs of high cooling rate CD weld bend specimen in Al-8Fe-4Ce tested after removal of outer periphery notch: (a) fracture initiation site at solidification-related weld defect near specimen center (arrow); (b) surface of defect at increased magnification, note secondary cracking perpendicular to fracture surface; (c) dimpled fracture surface of unaffected base metal.

END

DATE

FILMED

8-88

DTIC